UNIVERSIDADE FEDERAL DO ESPÍRITO SANTO
CENTRO TECNOLÓGICO
PROGRAMA DE PÓS-GRADUAÇÃO EM ENGENHARIA MECÂNICA

JOÃO VITOR FERREIRA DUQUE

A NOVEL PATHWAY TO RECOVER HYDROCARBONS FROM POLYETHYLENE RESIDUES THROUGH THE COMBUSTION-DRIVEN PYROLYSIS PROCESS

Vitória
2021

JOÃO VITOR FERREIRA DUQUE

A NOVEL PATHWAY TO RECOVER HYDROCARBONS FROM POLYETHYLENE RESIDUES THROUGH THE COMBUSTION-DRIVEN PYROLYSIS PROCESS

Tese apresentada ao Programa de Pós Graduação em Engenharia Mecânica do Centro Tecnológico da Universidade Federal do Espírito Santo, como requisito parcial para a obtenção do título de Doutor em Engenharia Mecânica.

Orientador: Prof. Dr. Márcio Ferreira Martins.
Coorientador: Prof. Dr. Gérald Debenest

Vitória
2021

Ficha catalográfica disponibilizada pelo Sistema Integrado de
Bibliotecas - SIBI/UFES e elaborada pelo autor

D946n

Duque, João Vitor Ferreira, 1989-
A novel pathway to recover hydrocarbons from polyethylene residues through the combustion-driven pyrolysis process / João Vitor Ferreira Duque. - 2021.
161 f. : il.

Orientador: Márcio Ferreira Martins.
Coorientador: Gérald Debenest.
Tese (Doutorado em Engenharia Mecânica) - Universidade Federal do Espírito Santo, Centro Tecnológico.

1. Combustão. 2. Análise térmica. 3. Cinética química. 4. Polietileno. 5. Reatores químicos. I. Martins, Márcio Ferreira. II. Debenest, Gérald. III. Universidade Federal do Espírito Santo. Centro Tecnológico. IV. Título.

CDU: 621

PROGRAMA DE PÓS-GRADUAÇÃO EM ENGENHARIA MECÂNICA
CENTRO TECNOLÓGICO
UNIVERSIDADE FEDERAL DO ESPÍRITO SANTO

“A NOVEL PATHWAY TO RECOVER HYDROCARBONS FROM POLYETHYLENE RESIDUES THROUGH THE COMBUSTION-DRIVEN PYROLYSIS PROCESS”

João Vitor Ferreira Duque

Marcio F Martins

Márcio Ferreira Martins, Ph.D.
(Orientador – PPGEM/UFES)

Gérald Debenest, Ph.D.
(Orientador - Université de Toulouse)

Marcos Tadeu D'Azeredo Orlando

Marcos Tadeu D’Azeredo Orlando, Ph.D.
(Examinador interno – PPGEM/UFES)

Ana Maura Araujo Rocha, Ph.D.
(Examinadora externa – UFOP)

Fernando Luiz Pellegrini Pessoa

Fernando Luiz Pellegrini Pessoa, Ph.D.
(Examinador externo – SENAI CIMATEC)

CentraleSupélec
Prof. Patrick Perré
Directeur de la Chaire de Biotechnologie
Laboratoire de Génie des Procédés et Matériaux
CEBB-51110 Pomacle

Patrick Perré, Ph.D.
(Examinador Externo - Universite Paris Saclay)

Tese apresentada ao Programa de Pós-Graduação em Engenharia Mecânica da Universidade Federal do Espírito Santo como parte dos requisitos necessários à obtenção do título de Doutor em Engenharia Mecânica. Tese de Doutorado com supervisão conjunta internacional UFES/Universidade de Toulouse/França

Vitória (ES), 24 de fevereiro de 2021.

A novel pathway to recover hydrocarbons from polyethylene residues through the combustion-driven pyrolysis process

Abstract — Global production of plastic materials has grown drastically, but the technologies adopted by industry and the policies of combining waste streams, collection, treatment, and disposal have not followed this rapid growth rate. Several methods of thermochemical conversion of plastic waste into useful products have been investigated in the last decades; however, in terms of energy efficiency, the search for a technique that results in the recovery of noble products from plastic wastes is still a challenge, as is the understanding of its thermal degradation behavior. Therefore, the thesis's general objective was to develop a self-sustainable energy device that uses low-grade fuels as heat-drive to pyrolysis, perform the polyethylene waste thermal cracking, and recover an energy-dense material. The steps toward achieving these objectives were to characterize a recycled polyethylene waste to determine its molecular composition and kinetics pathway from a single-step to a multi-step perspective; to launch a novel device in which the input energy for pyrolysis is driven by a combustion front propagating in a porous matrix, at this step, a new methodology was established to obtain a longitudinal temperature profile (LTP) for reactors with temperature increasing with time; to describe quantitatively and qualitatively for the first time, the propagation of a smoldering front in annular space - through temperature in time, gas analysis, and LTP - that wraps a concentric cylinder chamber in which the heat released by the combustion front is transferred for waste conversion; and finally, to conduct experiments toward the production and recovering of an energy-dense pyrolysis product in the form of wax and to characterize the wax employing FTIR to identify the functional groups, and a detailed kinetic analysis. The research results show that the polyethylene undergoing thermal and mechanical stress in its cycle life has functional groups with long carbon chains while weakening the compounds' bonds. The main consequence was that recycled polyethylene need less activation energy to degrade thermally, modifying the pyrolysis pathway's chemical groups. The designed combustion-driven reactor (C-DPyR) could perform polyethylene plastic waste pyrolysis. The proposed LTP served to explore the heat inputted to the pyrolysis chamber, ratifying that a self-sustaining combustion process carried enough energy to supply pyrolysis. The index Energy Availability showed that in the worst case, it remains 11% of energy underused, and at higher thermal energies conditions, just about 5% of the energy is consumed to convert the plastics. The primary outcome was that the volume ratio energy from combustion/energy to pyrolysis could be reduced by increasing the pyrolysis chamber's volume to convert more kg of plastic per batch. The conclusion can also be drawn that different heat inputs were used to pyrolyze the polyethylene waste, resulting in different pyrolysis products' yields. A maximum of about 87 wt.% of wax was recovered from an experiment at low thermal energy, confirming that low-grade fuel combustion is an alternative heat source capable of pyrolyzing plastic waste. The enthalpies of the recovered products hovered around 2115 J/g, and according to FTIR results, the wax's functional groups identified were like the ones in low-density polyethylene's waste. Therefore, the operational conditions attained by C-DPyR were able to recover a polyethylene wax. That means the C-DPyR process has the potential benefits of feedstock recycling in plastic waste management.

Keywords: Plastic waste, polyethylene, pyrolysis, heat of combustion, thermal analysis, C-DPyR process, polyethylene wax.

By
João Vitor FERREIRA DUQUE
joao.duque@ifes.edu.br
Institut de Mécanique des Fluides de Toulouse
2 Allée du Professeur Camille Soula
31400 TOULOUSE

Une nouvelle voie pour transfomer déchets de polyéthylène en hydrocarbures : utilisation de la pyrolyse alimentée par la combustion de résidus solides

Résumé — La production mondiale de matières plastiques a considérablement augmenté, mais les technologies adoptées par l'industrie et les politiques combinant les flux de déchets, la collecte, le traitement et l'élimination n'ont pas suivi ce taux de croissance rapide. Plusieurs méthodes de conversion thermochimique des déchets plastiques en produits utiles ont été étudiées au cours des dernières décennies; cependant, en terme d'efficacité énergétique, la recherche d'une technique aboutissant à la récupération de produits nobles à partir de déchets plastiques reste un défi, tout comme le reste la compréhension du comportement du déchet lors de sa dégradation thermique. Par conséquent, l'objectif général de la thèse était de développer un dispositif énergétique autosuffisant qui utilise des combustibles de faible qualité comme moteur thermique pour la pyrolyse, afin d'effectuer le craquage thermique des déchets de polyéthylène et enfin, de récupérer un matériau dense en énergie. Les étapes pour atteindre ces objectifs consistaient : - à caractériser un déchet de polyéthylène recyclé afin de déterminer sa composition moléculaire et sa schéma cinétique de dégradation selon une seule étape ou plusieurs étapes; - Puis, à développer un nouveau dispositif annulaire, dans lequel, l'énergie d'entrée pour la pyrolyse est générée par un front de combustion se propageant dans une matrice réactive composée de déchets et de carbone. Grâce à celui-ci, nous pouvons obtenir un profil de température longitudinal (LTP) dont la température augmente avec le temps; - Ensuite, nous avons décrit quantitativement et qualitativement la propagation d'un front de chaleur dans l'espace annulaire ainsi que la température au cours du temps. L'analyse des gazs produits ainsi que le LTP a été réalisé. Nous avons vérifié que dans cette chambre cylindrique concentrique, la chaleur dégagée par le front de combustion est bien transférée pour la conversion des déchets; - Et enfin, mener des expériences en vue de la production et la récupération d'un produit de pyrolyse dense en énergie sous forme de cire qui a été caractérisée en utilisant FTIR pour identifier les groupes fonctionnels, et son schéma cinétique de dégradation; Les résultats montrent que le polyéthylène soumis à des contraintes thermiques et mécaniques au cours de son cycle de vie possède des groupes fonctionnels avec de longues chaînes carbonées mais le recyclage affaiblit les liaisons des entre les groupes. La conséquence principale est que le polyéthylène recyclé nécessite moins d'énergie d'activation pour se dégrader thermiquement. Le réacteur de combustion qui a été conçu (C-DPyR) pourrait effectuer la pyrolyse des déchets de plastique de type polyéthylène. Le LTP que nous avons obtenu, permet d'apporter la chaleur à la chambre de pyrolyse par la combustion d'un résidu charbonneux, ce qui génère suffisamment d'énergie pour pyrolyser les déchets plastiques L'indice de disponibilité énergétique a montré que dans le pire des cas, 11% de l'énergie sous-utilisée reste disponible, et dans des conditions thermiques à plus haute températures, à peine 5% de l'énergie est consommée pour convertir les plastiques. Le résultat principal est donc que le rapport volumique (énergie de la combustion / énergie à la pyrolyse) pouvait être réduit en augmentant le volume de la chambre de pyrolyse pour convertir plus de résidus plastiques. Une autre observation peut être faite, à savoir que faire varier les apports de chaleur pour pyrolyser les déchets de polyéthylène, entraine des rendements différents de la pyrolyse. Un maximum d'environ 87% en poids de cire a été récupéré à partir d'une expérience à faible énergie thermique, confirmant que la combustion de carburant de faible qualité est une source de chaleur alternative capable de pyrolyser les déchets plastiques. Les enthalpies des produits récupérés oscillaient autour de 2115 J/g. Selon les résultats FTIR, les groupes fonctionnels de la cire identifiées étaient identiques à ceux du polyéthylène recyclé de basse densité. Par conséquent, les conditions opérationnelles atteintes par le C-DPyR permettent de récupérer une cire de polyéthylène. Cela signifie donc que le processus C-DPyR présente les avantages potentiels en ce qui concerne le recyclage des matières premières dans la gestion des déchets plastiques.

Mots clés : Déchets plastiques, polyéthylène, pyrolyse, chaleur de combustion, analyse thermique, procédé C-DPyR, cire de polyéthylène.

Pour
João Vitor FERREIRA DUQUE
joao.duque@ifes.edu.br
Institut de Mécanique des Fluides de Toulouse
2 Allée du Professeur Camille Soula
31400 TOULOUSE

Publications

Published:

Duque, J. V. F., Martins, M. F., Debenest, G., Orlando, M. T. D. (2020). The influence of the recycling stress history on LDPE waste pyrolysis. Polymer Testing, 86. `https://doi.org/10.1016/j.polymertesting.2020.106460`

Duque, J. V. F., Martins, M. F., Orlando, M. T. D. (2020). Biodegradable masterbatch blends: The implications on thermal conversion and recycling stream of polyethylene. Open Journal of Chemistry, 6(1), 008–010. `https://doi.org/10.17352/ojc.000016`

Pan, R., Duque, J. V. F., Debenest, G. (2020). Investigating Waste Plastic Pyrolysis Kinetic Parameters by Genetic Algorithm Coupled with Thermogravimetric Analysis. Waste and Biomass Valorization. `https://doi.org/10.1007/s12649-020-01181-4`

Pan, R., Duque, J. V. F., Martins, M. F., Debenest, G. Application of a neural fuzzy model combined with simulated annealing algorithm to predict optimal conditions for polyethylene waste non-isothermal pyrolysis. Heliyon. `https://doi.org/10.1016/j.heliyon.2020.e05598`

Under review:

Article: Duque, J. V. F., Bittencourt, F. L. F., Martins, M. F., Debenest, G. Developing a combustion-driven reactor for waste conversion.

Article: Duque, J. V. F., Martins, M. F., Bittencourt, F. L. F., Debenest, G. Self-sustaining combustion in annular space: an alternative heat source for waste conversion.

Article: Pan, R., Duque, J. V. F., Debenest, G. Waste Plastic Thermal Pyrolysis Analysis by a Neural Fuzzy Model Coupled with a Genetic Algorithm.

Book chapter: Martins, M. F., Duque, J. V. F., Soares, K., Orlando, M. T. D. Thermal analysis of recycled plastics. Springer Nature.

Patent: Martins, M. F., Duque, J. V. F.,Debenest, G. Combustion driven pyrolysis reactor: C-DPyR.

Acknowledgements

An amazing journey! With the certainty of the existence of a loyal financier, who never left me alone, who never asked me for anything in return, I was able to get here!

Aspiring sailor, with the unknown waiting for me, it would not be possible to control the ship alone. I am grateful to Dr. Martins for always having been by my side, giving me hope, guiding me, and showing me the necessary instruments to navigate. Thank you for teaching me to understand the maps and to respect the craft. Knowledge, commitment, and professionalism. I am grateful to Dr. Debenest for welcoming me in his laboratory, share his knowledge with me, and co-authored an important chapter in my professional life. With the help of you two, I controlled the insecurity and anxiety!

During this crossing, in my private cabin, a very pleasant and happy journey. By my side, my family was always ready to welcome me. Day after day, tireless warriors fighting shoulder to shoulder with me. The clearest source of wisdom and love. I thank my parents for teaching me to have hope, patience, and faith. I also thank my brother who has always been by my side.

The journey was long and I needed a few stops to refuel the energy. I thank the Lessa Moura family for welcoming me in Toulouse, helping me to overcome the absence of my family, my friends, and my country. It would have been much more difficult without you. My toulousaine family! I thank the Costa Martins family for the affection they have always opened the doors of their home to receive me. Many laughs, many conversations, many happy moments. It is very good to know that you are my friends!

Previous knowledge was also essential to navigate. I thank my friend Carlucio, who helped me discover the greatest lesson of sport, resilience! Also, I am very grateful to all teachers who encouraged me to seek knowledge. I thank Prof David Lo Jacono for the opportunity!

What was not lacking on this journey was fear! Fear of storms, fear of illness, fear of not responding and not being returned, fear of not being worthy. Some fears I overcame and others I just learn to live with. I thank the friends from IFES, LCC, and IMFT for their support. I thank Flávio for the many hours of teamwork. I thank Marcela for encouraging me. You were essential!

So, insisting, day after day, 1813 days, the horizon took shape, allowed me to believe, and this wonderful journey was concluded!

"O que sobra é a obra, o resto soçobra!" Lêdo Ivo

Contents

List of Figures

List of Tables

Chapter 1

Introduction

The production of plastic artifacts grows year after year worldwide and, in the same proportion, grows the amount of plastic waste. This phenomenon is because much of the plastic production is for single-use products, roughly speaking, turn into waste just after the first use, overloading the municipal solid waste streams around the world. That can be appointed as one cause of the universal environmental and human health crisis fomented by unplanned plastic disposal [1], Fig. 1.1.

Figure 1.1: The unplanned disposal of plastic waste worldwide (from [2]).

In 2019, global plastic production almost reached the historical mark of 368 million tonnes [3], Fig. 1.2, contributing to an accumulation of 6300 million tons since 1950s, and a projection of 1393 million tons for the year 2050 [4]. The main types of processed plastics are polyethylene (PE), polypropylene (PP), polystyrene (PS), polyethylene terephthalate (PET), and Polyvinyl-chloride (PVC), and about 65% of plastics production was mainly concentrated in developing countries [3]. Historically, the manufacturer has always been primarily focused on the diverse types of packaging. More recently, the new generation of waste has been driven by the unexpected demand for plastic artifacts due to the COVID-19 pandemic [5], Fig. 1.3. Again, single-use plastics in vogue, but now, for personal protective equipment (like face masks, gloves, and gowns) that suddenly skyrocketed around the world, putting the plastic reduction policies in check. Without having time to think about sustainable proposals for waste management and reinforcing the green plastics solutions chain (Appendix B), waste spread across the globe, often in inappropriate places, such as the marine environment, a fact of great discussion nowadays [7].

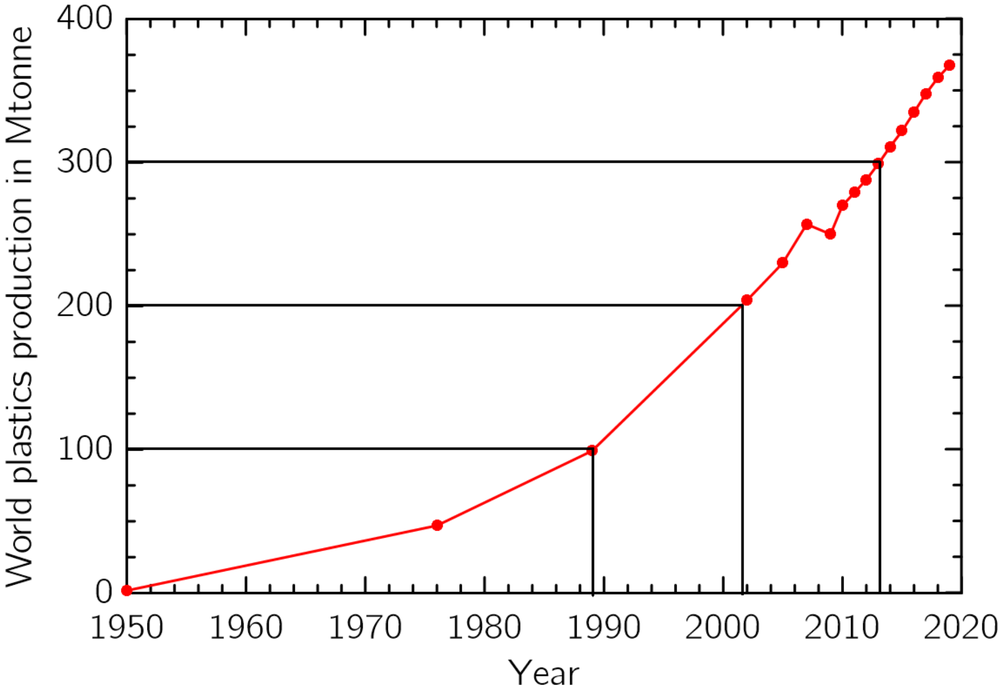

Figure 1.2: World plastics production from 1950 to 2019 (data from [3]).

How Can Plastic be Recycled?

The routes of plastic waste treatment have been widely discussed in the literature through schemes and technologies [4, 8]. The primary (re-extrusion), secondary (mechanical), tertiary (chemical), and quaternary (energy recovery) recycling, Fig. 1.4, require special attention related to waste characterization before its employment. Each route provides a unique set of advantages that makes it particularly beneficial for specific locations and applications [10]. Geyer et al. [11] estimated that, of all the plastic produced between 1950 and 2015, about 12% was incinerated, 9% recycled, and most of it, around 60%, has been discarded in landfills or in unplanned disposal environments, Fig. 1.5.

Figure 1.3: Accumulation of plastic waste generated by COVID-19 pandemic (from [6] - see Appendix A).

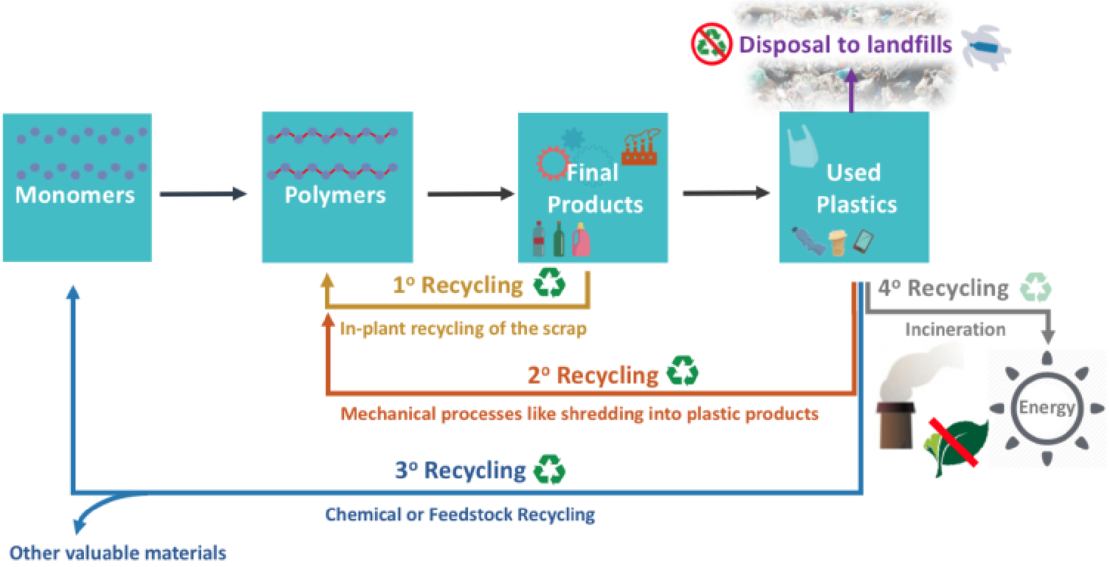

Figure 1.4: Types of plastic waste recycling (from Okan et al. [9] - see Appendix A).

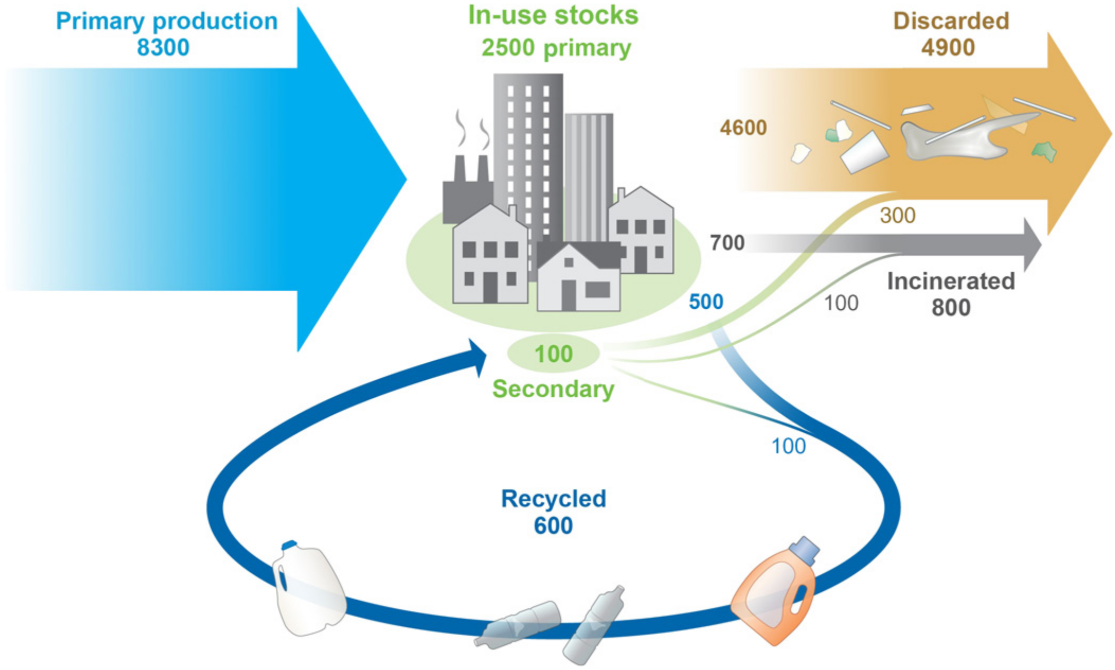

Figure 1.5: Cumulative plastic global production disposal from 1950 to 2015; in million metric tons (from Geyer et al. [11]).

In 2011, Butler [8] projected pyrolysis as a thermochemical conversion technology that could be considered a 'feedstock recycling' process. Indeed, some thermochemical technologies emerged [12], and others became commercial [13]. Nevertheless, due to each country's specificities, the space to develop new apparatus for pyrolyzing plastic waste is still relevant, since some problem related to reactor design limitation persists [4, 8].

Recent Laboratory and Commercial Reactors State-of-the-Art

When we focused on thermochemical conversion technologies to valorize waste plastics, specifically for pyrolysis, several setups have been implemented and tested to convert plastic waste using thermal or catalytic processes. Pyrolysis has been investigated on many scales, ranging from micro experimental setups to pilot and semi-industrial scales [8].

From 2010 to the present, few new features have been reported from the industrial scale viewpoint, such as microwave pyrolysis of polymeric materials [12] and miniature micro-factories concept under recycling e-waste [13]. The latter not necessarily encompass thermochemical conversion. A complete list of old technologies, not necessarily well established or operating, can be found in [8].

On the hand of laboratory-scale setups, they typically aim to study the degradation kinetics and the materials' properties in the thermogravimetry analyzer, i.e., heat transfer does not play a hole in the pyrolysis process that is, in this case, kinetically governed [14]. The heat transfer is then for the thermochemical conversion reactors, a technical challenge as the reactor is scaled-up. That increases the rigor to heat the reactor's material more efficiently [4]. For instance, in rotary kiln reactors, the heat is usually supplied to the kiln by externally heated walls. To improve heat transfer, metal spheres are put inside the reactor to promote heat transfer [4, 15]. Vacuum pyrolysis reactors have been mainly developed commercially [16], but, in general, they do not have good heat transfer. As also is the case of the stirred-tank reactors [4]. Basically, a pyrolysis reactor not optimally designed suffers from low heat transfer and temperature control results in a fussed polymer material in the reactor's interiors [4].

Although heat transfer is a key process for pyrolysis because it leads to temperature control, other operational factors that typically affect pyrolysis are the type of reactor, residence time, and operating pressure. In the context of the present thesis, where a new reactor concept is being launched, these factors will be implicitly approached along with the text.

Why is Polymer Characterization Important?

Identifying the mass, morphology, and molecular structure of polymeric materials (synthetic and natural) is termed polymer characterization. These polymers are made up of chains of macromolecules, bound together by covalent bonds. Their chemical/biological components define the properties of such structures. Usually, however, they are very versatile and useful in a variety of applications. Synthetic polymers include plastics (polyethylene and polystyrene), whereas natural polymers include wool and rubber. Therefore, plastic waste is challenging even though the industries, mainly the mechanical recycling industry, sort the waste by plastic-type; the contaminants are common constituents [17].

Most polymers are complex mixtures of molecules with different carbon lengths, structures, and functionality. Attempts to measure the exact chemical composition are complicated by the presence of contaminants in plastic waste. For these reasons, increasingly, instrumental methods such as gas chromatography [18], gel permeation (also known as size exclusion) chromatography [19], refractive index [20], differential scanning calorimetry [21], infrared spectroscopy [22], and nuclear magnetic resonance [23] are being used for characterization. Properties such as molecular weight distribution, degree of branching, degree of crystallinity, and functionality can be readily measured with these techniques.

Given the great sensitivity of plastics to temperature, thermal characterization is as crucial as chemical characterization. The contaminants can serve as catalysts to chemical reactions [24]. Consequently, knowledge about plastic thermal behavior becomes essential to choose the recycling route. To assess the behavior when plastics are submitted to a temperature change, the thermal analysis show to be the best option [21, 25, 26].

Plastic-to-Wax concept

The concept of converting plastics to products is not new. The conversion of plastic waste into petroleum feedstock is technically viable but also costly [27]. Contributing to high costs is the need of adapting a unique conversion technology to each one of the many types of plastic waste existent: Polyethylene, Polypropylene, Polystyrene, Polyamide, Polymethyl methacrylate, Polyethylene terephthalate, Polyurethane, Polyvinyl Chloride, Hydrochloride, Waste Electrical and Electronic Equipment, Poly Aromatic Hydrocarbons.

Therefore, it is somehow relevant to design a rector self-sustainable in energy that operates intermediate to low temperatures but with enough thermal energy to overcome the different enthalpy of pyrolysis brought by the different types of plastics and operating under close atmospheric pressure. Nevertheless, under such a configuration, and knowing that plastic pyrolysis leads to gas, liquid, and wax material, the wax production show be energetically less intense than gas and liquid production. Beyond these eco-friendly requirements, and well reported in the literature, polyolefins such as polyethylene are energetically favorable to produce wax [10].

Waxes are divided into several well-established groups, including paraffin waxes (from petroleum oil lubricating distillates [28]), microcrystalline wax (from residual lubricating oil fractions [28]), and polyethylene waxes (from low molecular weight and high-density raw materials [29]). Each wax type has been reported to have specific physical properties making them especially attractive. For example, polyethylene waxes are often used to formulate colorants for plastics [30], in polyvinyl chloride lubricants [31], adhesives, and inks to decrease friction [32]. Under catalytic presence, the wax can be converted into fuel, such as jet fuel [33].

Thesis goals

The thesis's general objective was to develop a self-sustainable energy device that uses low-grade fuels as heat-drive to pyrolysis, perform the polyethylene waste thermal cracking, and recover an energy-dense material. The steps toward achieving these objectives were:

- to launch a novel device in which the input energy for pyrolysis is driven by a combustion front propagating in a porous matrix, at this step, a new methodology was established to obtain a longitudinal temperature profile (LTP) for reactors with temperature increasing with time;

- to describe quantitatively and qualitatively for the first time, the propagation of a smoldering front in annular space - through temperature in time, gas analysis, and LTP - that wraps a concentric cylinder chamber in which the heat released by the combustion front is transferred for waste conversion;

- to characterize a recycled polyethylene waste to determine its molecular composition and kinetics pathway from a single-step to a multi-step perspective;

- and finally, to conduct experiments toward the production and recovering of an energy-dense pyrolysis product in the form of wax and to characterize the wax employing FTIR to identify the functional groups, and a detailed kinetic analysis.

Thesis outline

This thesis was written in "Integrated Article Format." A brief description of each chapter is presented below. Note that some redundant textual elements were added to the thesis structure as an exigence of the Doctoral School. That means an extra Introduction and Conclusion in the French language. For chapters 2, 3, 4, and 5, based on papers accepted or submitted, a one-page summary was added as the chapter's cover, giving the article's ins and outs and the details of my role in the article production.

Chapter 2, titled "Developing a combustion-driven reactor for waste conversion," a novel device called C-DPyR, in which a self-sustaining combustion front drives the input energy for pyrolysis was proposed. A new methodology to define a representative longitudinal temperature profile based on the time-averaged method at each thermocouple position was introduced. This chapter was submitted on September 09th, 2020, for considering publication.

Chapter 3, titled "Self-sustaining combustion in annular section: an alternative heat source for waste conversion," was focused on the smoldering front propagation in an annular section pathway and the implications of heat released by combustion as the energy source to overcome pyrolysis enthalpy of reaction.

Chapter 4, titled "The influence of the recycling stress history on LDPE waste pyrolysis," was highlighted that the PE recycling stress history increased long carbon chains groups; the thermal and mechanical stress weakens the boundary among PE compounds; the recycling stress decreases the pyrolysis enthalpy, and the pyrolysis pathway is a competition of phase change and chemical reactions. This chapter was published on February 28th, 2020, in the Polymer Testing journal.

Chapter 5, titled "Combustion-driven pyrolysis reactor: converting LDPE waste into hydrocarbons," presented the proof of the C-DPyR concept. The waxes recovered were characterized by TGA, DSC, FTIR.

Chapter 6 summarized the significant conclusions of the thesis and presented a series of recommendations for future work.

Finally, the Appendices provide the Supplementary Materials used through the text.

Bibliography

[1] Nielsen, Tobias D., *et al.*. *Politics and the plastic crisis: A review throughout the plastic life cycle.* Wiley Interdisciplinary Reviews: Energy and Environment 9.1 (2020): e360.

[2] Guglielmi, Giorgia. *In the next 30 years, we'll make four times more plastic waste than we ever have.* Science (2017).

[3] PlasticsEurope *The facts 2018, 2018, arXiv:arXiv:1011.1669v3 http://dx.doi.org/10.1016/j.marpolbul.2013.01.015.*

[4] Qureshi, Muhammad Saad, *et al.*. *Pyrolysis of plastic waste: opportunities and challenges.* Journal of Analytical and Applied Pyrolysis (2020): 104804.

[5] Silva, Ana L. Patrício, *et al.*. *Increased plastic pollution due to COVID-19 pandemic: Challenges and recommendations.* Chemical Engineering Journal (2020): 126683.

[6] Adyel, Tanveer M. *Accumulation of plastic waste during COVID-19.* Science 369.6509 (2020): 1314-1315.

[7] Anjana, K., *et al.*. *Review on plastic wastes in marine environment–Biodegradation and biotechnological solutions.* Marine Pollution Bulletin 150 (2020): 110733.

[8] Butler, Eoin, Ger Devlin, and Kevin McDonnell. *Waste polyolefins to liquid fuels via pyrolysis: review of commercial state-of-the-art and recent laboratory research.* Waste and biomass valorization 2.3 (2011): 227-255.

[9] Okan, Meltem, *et al.*. *Current approaches to waste polymer utilization and minimization: a review.* Journal of Chemical Technology & Biotechnology 94.1 (2019): 8-21.

[10] Al-Salem, S. M., *et al.*. *A review on thermal and catalytic pyrolysis of plastic solid waste.* Journal of Environmental Management 197 (2017): 177-198.

[11] Geyer, Roland, *et al.*. *Production, use, and fate of all plastics ever made.* Science advances 3.7 (2017): e1700782.

[12] Mahari, Wan Adibah Wan, *et al.*. *Production of value-added liquid fuel via microwave co-pyrolysis of used frying oil and plastic waste.* Energy 162 (2018): 309-317.

[13] Sahajwalla, Veena, and Vaibhav Gaikwad. *The present and future of e-waste plastics recycling.* Current Opinion in Green and Sustainable Chemistry 13 (2018): 102-107.

[14] Das, Pallab, and Pankaj Tiwari. *Valorization of packaging plastic waste by slow pyrolysis.* Resources, Conservation and Recycling 128 (2018): 69-77.

[15] A. Hornung, U. Hornung, A. Schoeneberger, J. Weichmann, H. Bockhorn. *Staged Pyrolysis, a Process for Chemical Separation of Waste Plastics.* Gestufte Pyrolyse Als Verfahrensprinzip Zur Chemischen Auftrennung Von Kunststoffgemischen, (1996).

[16] C. Roy, A. Chaala, H. Darmstadt, *The vacuum pyrolysis of used tires: end-uses for oil and carbon black products.* J. Anal. Appl. Pyrolysis (1999) 201–221 1999/07/01.

[17] Fred-Ahmadu, Omowunmi H., *et al.*. *Interaction of chemical contaminants with microplastics: Principles and perspectives.* Science of The Total Environment 706 (2020): 135978.

[18] Chen, Zhi-Feng, *et al.*. *Discrimination of Virgin and Recycled Polyethylene Based on Volatile Organic Compounds Using a Headspace GC-MS Coupled with Chemometrics Approach.* Food Packaging and Shelf Life 26 (2020): 100553.

[19] Yu, Youlu. *A Short-Chain Branching Distribution Determination Technique for Polyethylene Using IR5-Detected GPC.* Macromolecular Symposia. Vol. 390. No. 1. 2020.

[20] Zhang, Xiaoning, *et al.*. *Complex refractive indices measurements of polymers in visible and near-infrared bands.* Applied Optics 59.8 (2020): 2337-2344.

[21] Duque, João Vitor F., *et al.*. *The influence of the recycling stress history on LDPE waste pyrolysis.* Polymer Testing (2020): 106460.

[22] Asensio, Ruth Chércoles, *et al.*. *Analytical characterization of polymers used in conservation and restoration by ATR-FTIR spectroscopy.* Analytical and bioanalytical chemistry 395.7 (2009): 2081-2096.

[23] McBrierty, Vincent J., and Kenneth J. Packer. *Nuclear magnetic resonance in solid polymers.* Cambridge University Press, 2006.

[24] López, A., *et al.*. *Pyrolysis of municipal plastic wastes II: Influence of raw material composition under catalytic conditions.* Waste Management 31.9-10 (2011): 1973-1983.

[25] Kai, Xingping, *et al.*. *TG-FTIR-MS study of synergistic effects during co-pyrolysis of corn stalk and high-density polyethylene (HDPE).* Energy conversion and management 181 (2019): 202-213.

[26] Ferreira Duque, J. V., *et al.*. *Biodegradable masterbatch blends: The implications on thermal conversion and recycling stream of polyethylene.* Open Journal of Chemistry 6.1 (2020): 008-010.

[27] Fivga, Antzela, and Ioanna Dimitriou. *Pyrolysis of plastic waste for production of heavy fuel substitute: A techno-economic assessment.* Energy 149 (2018): 865-874.

[28] Cottom, William P. *Waxes.* Kirk-Othmer Encyclopedia of Chemical Technology (2000).

[29] Chang, Main. *Method for preparing polyethylene wax by gas phase polymerization.* U.S. Patent No. 4,914,253. 3 Apr. 1990.

[30] Banning, Jeffrey H., Bo Wu, and C. Wayne Jaeger. *Colorant compounds.* U.S. Patent No. 7,294,730. 13 Nov. 2007.

[31] Ejk, Adam J. *Lubricant composition for vinyl chloride polymers.* U.S. Patent No. 4,132,691. 2 Jan. 1979.

[32] Schaufelberger, Gretchen S. *Printing ink comprising carboxylic acid modified polyethylene wax.* U.S. Patent No. 3,216,885. 9 Nov. 1965.

[33] Zhang, Yayun, et al. *Jet fuel production from waste plastics via catalytic pyrolysis with activated carbons.* Applied Energy 251 (2019): 113337.

Introduction

La production de produits à base de plastique augmente d'année en année dans le monde et, donc la production de déchets suit la même courbe. Ce phénomène est dû au fait que la production de plastique est destinée majoritairement à des produits à usage unique, qui se transforment en déchets juste après la première utilisation, surchargeant ainsi les flux de déchets solides municipaux dans le monde entier. Cela peut être désigné comme l'une des causes de la crise mondiale de l'environnement et un problème pour la santé humaine généré par le dépôt illégal de déchets plastique [1], Figure 1.1.

En 2019, la production mondiale de plastique a presque atteint la barre historique de 368 millions de tonnes [3], Figure 1.2, contribuant à une accumulation de 6300 millions de tonnes depuis les années 1950, pour une projection de 1393 millions de tonnes pour l'année 2050 [4]. Les principaux types de plastiques traités sont le polyéthylène (PE), le polypropylène (PP), le polystyrène (PS), le polyéthylène téréphtalate (PET) et le polychlorure de vinyle (PVC). Environ 65% de la production de plastiques était principalement concentrée dans les pays en développement [3]. Historiquement, les déchets étaient très majoritairement des emballages. Plus récemment, une nouvelle génération de déchets a vu le jour de manière inattendue à savoir les déchets plastiques dus à la pandémie COVID-19 [5], Figure 1.3. Encore une fois, les plastiques à usage unique sont en vogue. Cependant, ce ne sont plus les emballages qui prédominent en terme de déchets plastiques, mais plutôt les équipements de protection individuelle (comme les masques faciaux, les gants et les blouses) dont la production a soudainement explosé dans le monde entier, mettant en échec les politiques de réduction des produits plastiques. Sans avoir le temps de réfléchir à des propositions durables pour la gestion des déchets et de renforcer la chaîne des solutions plastiques dites vertes (Appendix B), les déchets se répandent à travers le monde, souvent dans des endroits inappropriés, comme par exemple dans le milieu marin, où surgit un sujet de discussion majeur [7].

Comment le plastique peut-il être recyclé ?

Les voies de traitement des déchets plastiques ont été largement discutées dans la littérature à travers des schémas cinétiques mais aussi du point de vue des technologies [4, 8]. Des technologies dites primaire (ré-extrusion), secondaires (mécanique), tertiaires (chimique) et quaternaires (récupération d'énergie) recyclage, Figure 1.4, nécessitent une attention particulière concernant une bonne caractérisation des déchets avant leur emploi. Chaque technologie offre un ensemble unique d'avantages qui les rendent particulièrement avantageuses pour des applications spécifiques [10]. Geyer et al. [11] a estimé que, de tout le plastique produit entre 1950 et 2015, environ 12% ont été incinérés, 9% recyclés et, la plupart, environ 60%, ont été jetés dans des décharges ou dans des environnements d'élimination non planifiés, Figure 1.5.

En 2011, Butler [8] a projeté la pyrolyse comme une technologie de conversion thermochimique qui pourrait être considérée comme un processus de 'recyclage des matières premières'. En effet, certaines technologies thermochimiques ont émergé [12], et d'autres sont devenues commerciales [13]. Néanmoins, en raison des spécificités de chaque pays, l'espace pour développer de nouveaux appareils de pyrolyse des déchets plastiques est toujours d'actualité, car un problème subsiste quant à la conception des réacteurs [4, 8].

État de l'art récents de réacteurs à l'échelle du laboratoire et commerciale

Lorsque nous nous sommes concentrés sur les technologies de conversion thermochimique pour valoriser les déchets plastiques, en particulier sur la pyrolyse, plusieurs configurations ont été mises en œuvre et testées pour convertir les déchets plastiques à l'aide de procédés thermiques ou catalytiques. La pyrolyse a été étudiée à de nombreuses échelles, allant des configurations micro aux échelles pilotes et semi-industrielles [8].

De 2010 à nos jours, peu de nouvelles fonctionnalités ont été signalées du point de vue de l'échelle industrielle, comme la pyrolyse par microondes de matériaux polymères [12] et le concept de micro-usines miniatures dans le cadre du recyclage des déchets électroniques [13]. Cette dernière n'inclut pas nécessairement la conversion thermochimique. Une liste complète des anciennes technologies, pas nécessairement bien établies ou en fonctionnement, peut être trouvée dans [8].

Du côté des installations à l'échelle du laboratoire, ils visent généralement à étudier la cinétique de dégradation et les propriétés des matériaux lors d'analyse de thermogravimétrie, c'est-à-dire que le transfert de chaleur n'est pas limitant dans le processus de pyrolyse qui est, dans ce cas, régi cinétiquement [14]. Le transfert de chaleur concerne alors les réacteurs de conversion thermochimique, ce qui est un défi technique au fur et à mesure de la mise à l'échelle du réacteur. Cela nécessite un chauffage plus efficace du matériau dans le réacteur [4]. Par exemple, dans les réacteurs à four rotatif, la chaleur est généralement fournie au four par des parois chauffées de l'extérieur. Pour améliorer le transfert de chaleur, des sphères métalliques sont placées à l'intérieur du réacteur afin d'augmenter le transfert par conduction [4, 15]. Les réacteurs de pyrolyse sous vide ont été principalement développés dans le commerce [16], mais, en général, ils n'offrent pas de bonnes propriétés en ce qui concerne le transfert de chaleur. C'est aussi le cas des réacteurs à cuve agitée [4]. Fondamentalement, un réacteur de pyrolyse non conçu de manière optimale souffre d'un faible transfert de chaleur et le mauvais contrôle de la température entraîne la production d'un matériau polymère de qualité hétérogène à l'intérieur du réacteur [4].

Bien que le transfert de chaleur soit un processus clé pour la pyrolyse, d'autres facteurs opérationnels affectent également la pyrolyse comme le type de réacteur, le temps de séjour et la pression de fonctionnement. Dans le cadre de cette thèse, où un nouveau concept de réacteur est en cours de développé, ces facteurs seront implicitement abordés dans le manuscrit.

Pourquoi la caractérisation des polymères est-elle importante ?

L'identification de la masse, de la morphologie et de la structure moléculaire des matériaux polymères (synthétiques et naturels) est appelée caractérisation des polymères. Ces polymères sont constitués de chaînes de macromolécules, liées entre elles par des liaisons covalentes. Leurs composants chimiques / biologiques définissent les propriétés de telles structures. Cependant, ils sont généralement utilisés pour leur polyvalence dans bon nombre d'applications. Les polymères synthétiques comprennent les plastiques (polyéthylène et polystyrène), tandis que les polymères naturels comprennent la laine et le caoutchouc. Par conséquent, les déchets plastiques sont un défi même si les industries, principalement l'industrie du recyclage mécanique, trient les déchets par type de plastique. Cependant, tous possèdent des contaminants qui sont des constituants communs [17].

La plupart des polymères sont des mélanges complexes de molécules avec différentes longueurs de carbone, structures et fonctionnalités. Les tentatives de mesure de la composition chimique exacte sont rendues difficiles par la présence des contaminants dans les déchets plastiques. Pour ces raisons des méthodes instrumentales telles que la chromatographie en phase gazeuse [18], la chromatographie par perméation de gel (également connue sous le nom d'exclusion de taille) [19], l'indice de réfraction [20], la calorimétrie différentielle à balayage [21], la spectroscopie infrarouge [22], et la résonance magnétique nucléaire [23] sont utilisées pour la caractérisation. Des propriétés telles que la distribution du poids moléculaire, le degré de ramification, le degré de cristallinité et la fonctionnalité peuvent être facilement mesurées avec ces techniques.

Compte-tenu de la grande sensibilité des plastiques à la température, la caractérisation thermique est tout autant cruciale que la caractérisation chimique. Les contaminants peuvent servir de catalyseurs aux réactions chimiques [24]. Par conséquent, la connaissance du comportement thermique du plastique devient essentielle pour choisir la meilleure voie de recyclage. Pour évaluer le comportement lorsque les plastiques sont soumis à un changement de température, l'analyse thermique s'avère être la meilleure option [21, 25, 26].

Des déchets plastiques aux cires

Le concept de la conversion des plastiques en produits n'est pas nouveau. La conversion des déchets plastiques en matières premières pétrolières est techniquement viable mais également coûteuse [27]. La nécessité d'adapter une technologie de conversion unique à chacun des nombreux types de déchets plastiques existants contribue aux coûts élevés : polyéthylène, polypropylène, polystyrène, polyamide, polyméthacrylate de méthyle, polyéthylène téréphtalate, polyuréthane, chlorure de polyvinyle, chlorhydrate, déchets électriques et électroniques, hydrocarbures poly aromatiques.

Par conséquent, il est pertinent de concevoir un recteur autonome en énergie qui fonctionne à des températures intermédiaires à basses mais avec suffisamment d'énergie thermique pour surmonter les différentes perte de chaleur de pyrolyse générées par les types de plastiques présents au sein du réacteur. Néanmoins, dans une telle configuration, et sachant que la pyrolyse plastique conduit à un matériau gazeux, liquide et cireux, la production de cire se révèle énergétiquement moins intense que la production gazeuse et liquide. Au-delà de ces exigences écologiques, et bien rapportées dans la littérature, les polyoléfines telles que le polyéthylène sont énergétiquement favorables à la production de cire [10].

Les cires sont divisées en plusieurs groupes bien établis, à savoir, les cires de paraffine (provenant de distillats lubrifiants d'huile de pétrole [28]), les cires microcristallines (provenant de fractions d'huile lubrifiante résiduelle [28]) et les cires de polyéthylène (des matériaux à faible poids moléculaire et de haute densité [29]). Il a été rapporté que chaque type de cire avait des propriétés physiques spécifiques qui les rendaient particulièrement attrayantes. Par exemple, les cires de polyéthylène sont souvent utilisées pour formuler des colorants pour les plastiques [30], dans les lubrifiants au chlorure de polyvinyle [31], ou pour produire des adhésifs et des encres pour diminuer le frottement [32]. En présence de catalyseurs, la cire peut être convertie en carburant, tel que le carburéacteur [33].

Objectifs de la thèse

L'objectif général de la thèse était de développer un dispositif énergétique auto-durable qui utilise des combustibles de faible qualité comme moteur thermique pour la pyrolyse. Cela permet alors d'effectuer le craquage thermique des déchets de polyéthylène et de récupérer un matériau dense en énergie.

Les étapes pour atteindre ces objectifs étaient les suivantes :

- de lancer un nouveau dispositif dans lequel l'énergie d'entrée pour la pyrolyse est entraînée par un front de combustion se propageant dans une matrice poreuse. Une nouvelle méthodologie a été mise en place afin d'obtenir un profil de température longitudinal (LTP) pour les réacteurs dont la température augmente avec le temps;
- de décrire quantitativement et qualitativement la propagation d'un front de chaleur dans l'espace annulaire ainsi que la température au cours du temps. L'analyse des gazs produits ainsi que le LTP a été réalisé. Nous avons vérifié que dans cette chambre cylindrique concentrique, la chaleur dégagée par le front de combustion

est bien transférée pour la conversion des déchets;

- caractériser un déchet de polyéthylène recyclé pour déterminer sa composition moléculaire et ses schémas cinétiques de dégradation en partant d'un schéma à une seule étape mais en se projetant vers des schémas en plusieurs étapes;
- et enfin, mener des expériences en vue de la production et de la récupération d'un produit de pyrolyse dense en énergie sous forme de cire, de caractériser la cire en utilisant une méthode FTIR afin d'identifier les groupes fonctionnels, et d'obtenir une analyse cinétique détaillée.

Bibliography

[1] Nielsen, Tobias D., *et al.*. *Politics and the plastic crisis: A review throughout the plastic life cycle.* Wiley Interdisciplinary Reviews: Energy and Environment 9.1 (2020): e360.

[2] Guglielmi, Giorgia. *In the next 30 years, we'll make four times more plastic waste than we ever have.* Science (2017).

[3] PlasticsEurope *The facts 2018, 2018, arXiv:arXiv:1011.1669v3 http://dx.doi.org/10.1016/j.marpolbul.2013.01.015.*

[4] Qureshi, Muhammad Saad, *et al.*. *Pyrolysis of plastic waste: opportunities and challenges.* Journal of Analytical and Applied Pyrolysis (2020): 104804.

[5] Silva, Ana L. Patrício, *et al.*. *Increased plastic pollution due to COVID-19 pandemic: Challenges and recommendations.* Chemical Engineering Journal (2020): 126683.

[6] Adyel, Tanveer M. *Accumulation of plastic waste during COVID-19.* Science 369.6509 (2020): 1314-1315.

[7] Anjana, K., *et al.*. *Review on plastic wastes in marine environment–Biodegradation and biotechnological solutions.* Marine Pollution Bulletin 150 (2020): 110733.

[8] Butler, Eoin, Ger Devlin, and Kevin McDonnell. *Waste polyolefins to liquid fuels via pyrolysis: review of commercial state-of-the-art and recent laboratory research.* Waste and biomass valorization 2.3 (2011): 227-255.

[9] Okan, Meltem, *et al.*. *Current approaches to waste polymer utilization and minimization: a review.* Journal of Chemical Technology & Biotechnology 94.1 (2019): 8-21.

[10] Al-Salem, S. M., *et al.*. *A review on thermal and catalytic pyrolysis of plastic solid waste.* Journal of Environmental Management 197 (2017): 177-198.

[11] Geyer, Roland, *et al.*. *Production, use, and fate of all plastics ever made.* Science advances 3.7 (2017): e1700782.

[12] Mahari, Wan Adibah Wan, *et al.*. *Production of value-added liquid fuel via microwave co-pyrolysis of used frying oil and plastic waste.* Energy 162 (2018): 309-317.

[13] Sahajwalla, Veena, and Vaibhav Gaikwad. *The present and future of e-waste plastics recycling.* Current Opinion in Green and Sustainable Chemistry 13 (2018): 102-107.

[14] Das, Pallab, and Pankaj Tiwari. *Valorization of packaging plastic waste by slow pyrolysis.* Resources, Conservation and Recycling 128 (2018): 69-77.

[15] A. Hornung, U. Hornung, A. Schoeneberger, J. Weichmann, H. Bockhorn. *Staged Pyrolysis, a Process for Chemical Separation of Waste Plastics.* Gestufte Pyrolyse Als Verfahrensprinzip Zur Chemischen Auftrennung Von Kunststoffgemischen, (1996).

[16] C. Roy, A. Chaala, H. Darmstadt, *The vacuum pyrolysis of used tires: end-uses for oil and carbon black products.* J. Anal. Appl. Pyrolysis (1999) 201–221 1999/07/01.

[17] Fred-Ahmadu, Omowunmi H., *et al.*. *Interaction of chemical contaminants with microplastics: Principles and perspectives.* Science of The Total Environment 706 (2020): 135978.

[18] Chen, Zhi-Feng, *et al.*. *Discrimination of Virgin and Recycled Polyethylene Based on Volatile Organic Compounds Using a Headspace GC-MS Coupled with Chemometrics Approach.* Food Packaging and Shelf Life 26 (2020): 100553.

[19] Yu, Youlu. *A Short-Chain Branching Distribution Determination Technique for Polyethylene Using IR5-Detected GPC.* Macromolecular Symposia. Vol. 390. No. 1. 2020.

[20] Zhang, Xiaoning, *et al.*. *Complex refractive indices measurements of polymers in visible and near-infrared bands.* Applied Optics 59.8 (2020): 2337-2344.

[21] Duque, João Vitor F., *et al.*. *The influence of the recycling stress history on LDPE waste pyrolysis.* Polymer Testing (2020): 106460.

[22] Asensio, Ruth Chércoles, *et al.*. *Analytical characterization of polymers used in conservation and restoration by ATR-FTIR spectroscopy.* Analytical and bioanalytical chemistry 395.7 (2009): 2081-2096.

[23] McBrierty, Vincent J., and Kenneth J. Packer. *Nuclear magnetic resonance in solid polymers.* Cambridge University Press, 2006.

[24] López, A., *et al.*. *Pyrolysis of municipal plastic wastes II: Influence of raw material composition under catalytic conditions.* Waste Management 31.9-10 (2011): 1973-1983.

[25] Kai, Xingping, *et al.*. *TG-FTIR-MS study of synergistic effects during co-pyrolysis of corn stalk and high-density polyethylene (HDPE).* Energy conversion and management 181 (2019): 202-213.

[26] Ferreira Duque, J. V., *et al.*. *Biodegradable masterbatch blends: The implications on thermal conversion and recycling stream of polyethylene.* Open Journal of Chemistry 6.1 (2020): 008-010.

[27] Fivga, Antzela, and Ioanna Dimitriou. *Pyrolysis of plastic waste for production of heavy fuel substitute: A techno-economic assessment.* Energy 149 (2018): 865-874.

[28] Cottom, William P. *Waxes.* Kirk-Othmer Encyclopedia of Chemical Technology (2000).

[29] Chang, Main. *Method for preparing polyethylene wax by gas phase polymerization.* U.S. Patent No. 4,914,253. 3 Apr. 1990.

[30] Banning, Jeffrey H., Bo Wu, and C. Wayne Jaeger. *Colorant compounds.* U.S. Patent No. 7,294,730. 13 Nov. 2007.

[31] Ejk, Adam J. *Lubricant composition for vinyl chloride polymers.* U.S. Patent No. 4,132,691. 2 Jan. 1979.

[32] Schaufelberger, Gretchen S. *Printing ink comprising carboxylic acid modified polyethylene wax.* U.S. Patent No. 3,216,885. 9 Nov. 1965.

[33] Zhang, Yayun, et al. *Jet fuel production from waste plastics via catalytic pyrolysis with activated carbons.* Applied Energy 251 (2019): 113337.

CHAPTER 2

Developing a combustion-driven reactor for waste conversion

Contents

Summary

In this chapter, a novel device in which a combustion front drives the input energy for pyrolysis was proposed: the Combustion-Driven Pyrolysis Reactor, C-DPyR. The reactor was designed, built, tested, and launched as a novel experimental device capable of performing pyrolysis of condensed phase matters by using the oxidation of low-grade fuels as a heat-drive. The reactor was assessed under different operating conditions of inlet air velocities and bed compositions, and the reliability of twenty-nine experimental runs was verified through repeatability, empirical dimensionless correlations, and analysis of variance.

Charcoal-based beds were used as reactive porous media to propagate the self-sustaining combustion front and, from the experimental data of temperature evolution, a new methodology to define a representative longitudinal temperature profile (LTP) based on the time-averaged method at each thermocouple position was proposed. Also, attention was paid to demonstrate that it is mandatory to take into account the data frequency and not the peak temperature to establish a representative LTP. Using the LTP, different heat-drive conditions were described, average temperatures between 345 - 588 °C were reached and the effect of the heat losses through the walls revealed.

To investigate the influence of the input parameters on LTP, the reactor's dimensionless numbers based on Pi theorem were presented and revealed the power-law relationship between temperature and inputs. The analysis of variance ANOVA explained the independence of the input parameters on defining the longitudinal temperature profile. Small standard deviations on the temperature evolution, ranged from 30 °C to 54 °C, emphasized that the measurements were very consistent, i.e., the experiments demonstrated excellent repeatability.

A positive energy balance was a characteristic of all experiments, and the main conclusion of this chapter is that the combustion-driven pyrolysis reactor can be used as an alternative device for waste conversion, taking advantage over conventional pyrolysis reactors, in terms of scalability to industrial application and in terms of electricity consumption.

Candidate contribution: Conceptualization, methodology, experimental design and execution, formal analysis, resources, data curation, writing - original draft, visualization.

2.1 Introduction

It is fundamental to acknowledge the advantages of pyrolysis on waste valorization [1, 2, 3, 4]. Ghosh et al. [4] report that pyrolysis's major advantage lies in environmental concerns because it is a cost-effective technology and helps curb environmental pollution. On the hand of the process, but still concerning pollutants, the main advantage reported by [2] is that during pyrolysis, the organic components of materials are decomposed. However, the inorganic ingredients (fillers, metals, etc.) remain practically unaltered and free of organic matter and pathogens.

Besides the byproduct potentials, as exemplified above, pyrolysis's valuable products, e.g., char, oil, and combustible gases, are used for energy production and heat generation [5]. Typical pyrolysis experiments on municipal solid waste [6], plastic waste [7], human waste [8], and, more traditionally, biomasses [9], have been intensely studied regarding the pyrolysis products and experimental parameters. Nevertheless, the improvement of pyrolysis reactors is always welcome [10], specially when it comes to energy consumption, which is a contribution from this work. Also, according to Ramirez and Rainey [11], incentives towards improving process conversion ratios, increasing thermal efficiency, and reducing process losses are necessary to increase these cleaner production technologies' profitability even though plants on multi-feedstock are successfully in operation around the world [12, 13, 14].

A variety of reactors, such as batch, rotary kiln, vacuum, and fluidized-bed used for pyrolysis, are heated externally by an electric device to initiate the process and maintain the desired bed temperature value [15]. For instance, microwave pyrolysis has been reported to consume between $0.58 - 0.65$ kWh per kilogram of sample [16], whereas pyrolysis in a batch reactor consumed 0.29 kWh per kilogram of sample [17]. Beyond the energy consumption, the heat source is reported as one of the difficulties in measuring the so-called pyrolysis temperature. One of the reactor's classifications based on the heat source proposed by Lédé and Authier [18] considered the reactor temperature increasing with time from the moment the sample is introduced in the reactor.

The heat transfer concept between the reactor walls and the sample is crucial for optimizing product yields and compositions. Another main characteristic of the heat transfer concept is forming a zero-temperature gradient zone, commonly called a hot zone, or thermostatic zone [19]. The length of the zone is associated with the reactor's scale; this, in turn, is related to the wall heat loss. The challenge is to improve or develop a scalable pyrolysis reactor with a heat source capable of heating the entire sample as rapidly as possible, consuming a low amount of energy [20]. Note that the challenging background is related to the solid sample's thermal resistance, commonly defined as the Biot number [18].

Therefore, a self-sustaining heat supply mechanism for pyrolysis is yet desirable. Sun et al. [21, 22] have made a proposition in this direction, such as the self-pyrolysis process applied for in situ fracture for oil shale recovery, consisting of a chemical heat-enhanced process with partial oxidation of kerogen to diminish the external energy input. Another approach was proposed by Tagutchou et al. [23]. Both [21, 22] and [23] are oxygen-controlled processes similar to smoldering [24]. In these so-called topological reactors, the pyrolysis/gasification occurs in the same chamber profiting from the char oxidation heat release within a controlled and spatially fixed zone in which the heat is supplied. The drawback of the topological reactors is the pyrolysis products and char's flue gases interact.

Smoldering combustion is a flameless and heterogeneous oxidation reaction limited by the rate at which oxygen diffuses into the surface of a condensed matter [25]. Smoldering is a self-sustaining front when, after the ignition energy input, the heat released by the fuel's oxidation overcomes the heat losses to the surroundings [24]. Literature reports several applications for smoldering combustion from laboratory [26, 27] to full-scale reactors [28, 29]. However, to the best of the authors' knowledge, none work reports its use as an energy source to pyrolyze matters in a coupled chamber, where temperature and atmosphere are controlled to some extent as in electrical furnaces.

The challenge within this proposition is associating heat to a controlled temperature with enough sensitivity to the operational parameters. For pyrolysis, the critical input parameters generally are summarized in the heating rate, residence time, and temperature [19]. In contrast, for smoldering combustion, the main parameters are the inlet air velocity, bed composition, and bed properties [30, 31].

In the present study, a novel device in which pyrolysis's input energy is driven by a self-sustaining combustion front propagating in a porous matrix is proposed. This work also contributes to previous researches by introducing a new method based on the temperature frequency distribution of temperature measurements to obtain an accurate representation of the longitudinal temperature profile. A sensitivity analysis of the experimental parameters, inlet air velocity and bed composition, is carried out based on analysis of variance complemented by an empirical correlation built following a dimensionless analysis.

2.2 The combustion-driven pyrolysis reactor (C-DPyR)

2.2.1 Description of the reactor

A new application for self-sustaining smoldering combustion in a reactive porous medium and a novel experimental device is presented. The ideas were to use the energy released in combustion to drive the heat supply to a pyrolysis process; and arrange two concentrical vertical cylinders forming two chambers, the inner for pyrolysis and the outer for combustion. Although the chambers' inlet and outlet followed independent paths, heat transfer occurred through the interface wall. Fig. 2.1 shows the reactor sketch.

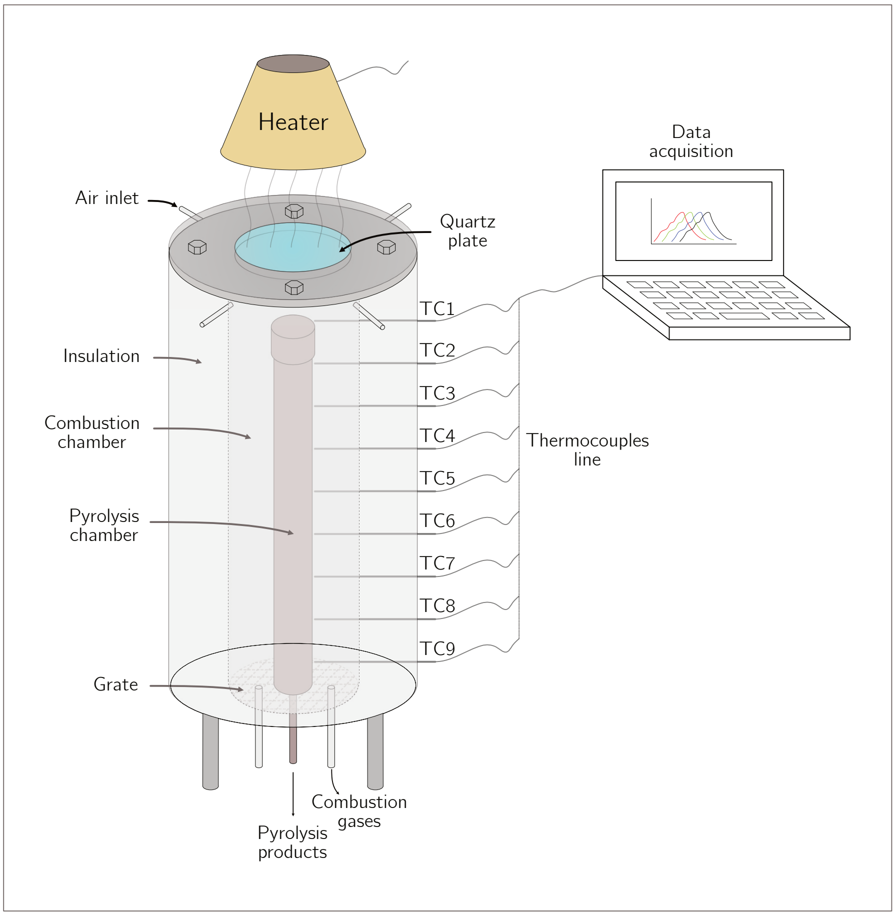

Figure 2.1: Sketch of the combustion-driven pyrolysis reactor proposed in this work.

Combustion chamber The combustion chamber consists of a vertical stainless steel cylinder (73 mm diameter and 450 mm height) wrapped by a heat-insulating layer of 50 mm (blanket Superwool 607, 0.28 W/mK at 982 °C). Along the longitudinal axis, near the interface wall, nine thermocouples type-K (3 mm diameter) were evenly distributed each 50 mm to measure the temperature. The combustion chamber's top is sealed with a 3.2 mm thick quartz disc, attached by a stainless steel flange. Just below the quartz disc, air inlets provide a constant flow guaranteed by a mass flow controller (MFC 8741, 0-30 Nl/min, Burkert Ltda). A grate is used to hold the fuel bed at the bottom, allowing the flue gases to exit.

For the ignition process, a conical spiral heater (1600 W - 220 V AC) is placed at the reactor's top to supply the required energy. The heat by radiation crosses the quartz disc reaching the fuel bed. The heater temperature is controlled, and the energy consumption is recorded by a digital power meter.

Pyrolysis chamber This chamber is made of stainless steel cylinder, 25.4 mm diameter, coaxially placed inside the reactor. It has an inlet, sealed by a screw-on metallic cap, and at the bottom, an outlet designed to allow the pyrolysis products to exit. The top and lateral walls are the interfaces between the chambers in which the heat is transferred. Further details are intentionally omitted due to the patent process.

2.2.2 Experimental protocol

A complete experimental protocol was created to investigate the influence of the experimental parameters that govern the front propagation.

After filling the reactor with the charcoal-based mixtures, it was sealed and connected to the compressed air supply via the mass flow controller. The desired airflow rate and the temperature recording were initiated. The heater was turned on, blocked by thermal insulation until it reached 700 °C when the insulation was removed, starting the ignition process. The heater was turned off when thermocouple TC_1 reached the peak. During the ignition procedure, electricity consumption was recorded by a digital power meter.

The experiment was considered finished after all monitored thermocouples were in the cooling process. Table 2.1 summarizes the twenty-nine experiments in terms of the input parameters, inlet air velocity, v_a, and bed composition properties, and the response variables, longitudinal temperature profile, T_z, process runtime, mass consumption rate, dm/dt, and net energy available for pyrolysis, E_{net}.

Table 2.1: Input parameters and summarized results for different runs.

		Input parameters						Response variables			
Exp.	n*	Bed	φ	ρ_m [kg/m^3]	$\lambda_m(\times 10^2)$ [W/mk]	c_{p_m} [J/KgK]	$v_a(\times 10^2)$ [m/s]	T_z [°C]	Runtime [s]	$dm/dt(\times 10^5)$ [kg/s]	$E_{net}(\times 10^4)$ [kWh/kg]
1	1	B_1	0.51	313.1	2.7	1070.1	3.0	464	13816	3.3	2.5
2	1	B_1	0.51	313.1	2.7	1070.1	4.0	479	12636	3.1	2.1
3	1	B_1	0.51	313.1	2.7	1070.1	4.9	494	6990	6.6	4.1
4	4	B_1	0.51	313.1	2.7	1070.1	5.9	542	6824	6.1	3.8
5	1	B_1	0.51	313.1	2.7	1070.1	6.9	518	5537	7.3	4.1
6	1	B_1	0.51	313.1	2.7	1070.1	8.9	550	3668	11.0	4.6
7	1	B_1	0.51	313.1	2.7	1070.1	10.9	588	3196	12.3	4.7
8	1	B_2	0.52	335.8	7.4	1320.3	5.9	510	5420	8.5	3.1
9	1	B_3	0.48	352.2	11.4	1534.2	5.9	477	4693	11.1	3.0
10	1	B_4	0.57	408.3	5.7	1061.6	5.9	473	4216	8.1	2.0
11	1	B_4	0.57	408.3	5.7	1061.6	8.9	540	3616	11.6	2.8
12	1	B_5	0.60	464.0	7.4	1057.3	4.0	382	6631	5.2	0.8
13	4	B_5	0.60	464.0	7.4	1057.3	5.9	386	3841	9.4	1.4
14	1	B_5	0.60	464.0	7.4	1057.3	8.9	458	2116	17.7	1.9
15	4	B_6	0.60	564.1	9.8	1053.3	5.9	356	5231	7.9	0.7
16	1	B_6	0.60	564.1	9.8	1053.3	8.9	345	1390	28.7	1.2
17	2	B_6	0.60	564.1	9.8	1053.3	10.9	402	994	36.6	1.1
18	2	B_6	0.60	564.1	9.8	1053.3	11.9	389	2537	18.0	1.3

*Number of repetitions.

2.2.3 Longitudinal temperature profile (LTP)

The best way to find a representative temperature for the pyrolysis chamber is to time-average the temperature evolution at each thermocouple position, such as $\int_0^t T(t)dt / \int_0^t dt$. In this case, the result is a longitudinal temperature profile with nine points. The LTP can be used to fit a representative function and to obtain the heat flux driven from the combustion front to the pyrolysis chamber. Considering these premises, the temperature frequency distribution, plotted as histograms or condensed as violin plots, evidentiates each temperature range's contribution to the temperature time-average. Fig. 2.2 shows a conceptual flow diagram of the statistical foundation used to obtain the LTP.

2.2.4 Characteristics of the fed material

The primary strategy to ensure and control the pyrolysis reactor's heat was to vary the bed composition served as a reactive porous media to propagate the self-sustaining combustion front. For that, charcoal beds (B_1 to B_3) and different charcoal-based mixtures with inorganic material (B_4 to B_6) were investigated and summarized in terms of the proximate composition and heating value (Table 2.2).

The materials were crushed and then sieved according to the desired granulometry, between 2 and 3 mm, and stored in sealed pails. Each sample was characterized so that its proximate analysis could be determined following ASTM D3172-13; D3173; D3173M-

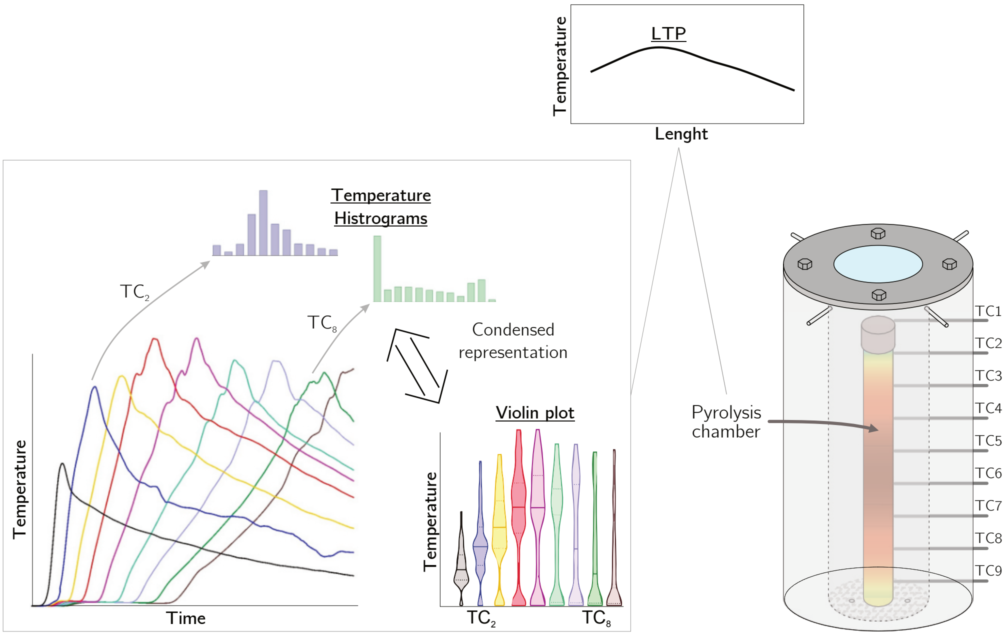

Figure 2.2: A conceptual flow diagram.

17a; D3174-12; D3175-20. The lower heating value, Q, was calculated based on Dermibas [32].

Table 2.2: Proximate analysis and heating value of the beds used during the experiments.

Bed	Proximate analysis, db (wt.%)					$Q^*(MJ/kg)$
	FC	VM	MC	Ash	IM	
B_1	58.8	28.4	3.4	9.4	0.0	22.7
B_2	49.0	23.7	19.5	7.8	0.0	18.9
B_3	42.0	20.3	31.0	6.7	0.0	16.2
B_4	47.9	22.7	2.7	7.5	20.1	18.2
B_5	39.2	19.9	2.2	6.3	33.3	15.1
B_6	29.4	14.2	1.7	4.7	50.0	11.4

* Deviation of 4%.

2.2.5 Statistical analysis

Repeatability Individual runs were conducted varying the bed composition and inlet air velocity to cover a wide experimental range. The response variables temperature evolution and longitudinal profile, total fuel consumption were evaluated, searching for a characteristic trend. Observed the trend, three classes of experiments stood out, representing low, medium, and high longitudinal temperature profiles. These three classes of experiments were repeated at least three times.

Analysis of variance The effects of air velocity and bed composition on the longitudinal temperature profile were tested using the analysis of variance, considering a null hypothesis (H_0) where there was no influence of the variables (and interactions) on the outcome. The temperature observations were described by the effects model [33]:

$$T_{ijk} = \mu + \tau_i + \beta_j + (\tau\beta)_{ij} + \epsilon_{ijk} \tag{2.1}$$

Where T is the longitudinal temperature observations, τ is the effect of the bed composition, β is the effect of air velocity, $(\tau\beta)$ is the effect of variables interaction, and ϵ is the random error effect. Indexes i, j, k are the number of observations from bed composition, air velocity, and the replicates, respectively, with $i\,\{1, ..., a\}\,, j\,\{1, ..., b\}\,, k\,\{1, ..., n\}$.

To consider a parameter statistically significant, the null hypothesis, $\tau = \beta = (\tau\beta) = 0$, was tested by comparing the P-values from F-test with a confidence level of α=0.01. For $P < \alpha$, the null hypothesis was rejected and the parameter was considered statistically significant.

The P-values were calculated from the ANOVA F-test, developed using sums of squares:

$$SS_T = SS_\tau + SS_\beta + SS_{\tau\beta} + SS_\epsilon \tag{2.2}$$

$$SS_T = \sum_{i=1}^{a}\sum_{j=1}^{b}\sum_{k=1}^{n} T_{ijk}^2 - \frac{T_{...}^2}{abn} \tag{2.3}$$

$$SS_\tau = \frac{1}{bn}\sum_{i=1}^{a} T_{i..}^2 - \frac{T_{...}^2}{abn} \tag{2.4}$$

$$SS_\beta = \frac{1}{an}\sum_{j=1}^{b} T_{.j.}^2 - \frac{T_{...}^2}{abn} \tag{2.5}$$

$$SS_{\tau\beta} = \frac{1}{n}\sum_{i=1}^{a}\sum_{j=1}^{b} T_{ij.}^2 - \frac{T_{...}^2}{abn} - SS_\tau - SS_\beta \tag{2.6}$$

Equation 2.2 shows that the total sum of squares (SS_T) is equal to a sum of square due to bed composition effects (SS_τ), a sum of square due to air velocity effects (SS_β), a sum of square due to the effects of interaction between variables ($SS_{\tau\beta}$), and a sum of square due to error (SS_ϵ). From Equations 2.3-2.6, the terms $T_{i..}$, $T_{.j.}$,$T_{..k}$, $T_{...}$, and its combinations are the grand averages varying i,j, and k. The mean squares were calculated by dividing the squares' sum by the degree of freedom of each variable. Detailed information regarding the ANOVA methodology can be consulted in Reference [33].

2.3 Results and discussion

2.3.1 Temperature measurements reliability

The numerous experiments performed to establish the propagation characteristics of a combustion front in annular space were evaluated in terms of temperature evolution, in which all data for the upcoming analysis came from it. Therefore, it is crucial to present these data's experimental reproducibility in terms of the standard deviation, Fig. 2.3.

By analyzing all the experiments covering the bed composition and air velocity ranges (Table 2.1), three experimental conditions were chosen to assess the reproducibility: exp. 4, 13, and 15, see Table 2.1.

Fig. 2.3 represents the averaged temperature evolution (continuous line) and the respective standard deviations (shaded area) based on at least three repetitions. For bed B_1 (Fig. 2.3a), the average standard deviation was around 30 °C. Given the complexity brought by mixing charcoal and inorganic materials, the beds B_5 and B_6 showed slightly higher deviations, 39 °C and 54 °C, respectively (Fig. 2.3b,c).

These low standard deviations on the temperature evolution emphasized that the measurements were very consistent, i.e., the experiments demonstrated excellent repeatability and suggested that any variation falling outside the deviations was due to variations of the input parameters.

2.3.2 Temperature frequency distribution (TFD)

The data frequency of each of the nine thermocouple's recordings was evaluated following the methodology from section 2.2.3. Here the distributions of three classes of experiments were represented as violin plots (Fig. 2.3d, e, f).

For instance, TFD from bed B_1 (exp. 4, Fig. 2.3d), tended to increase towards TC_9

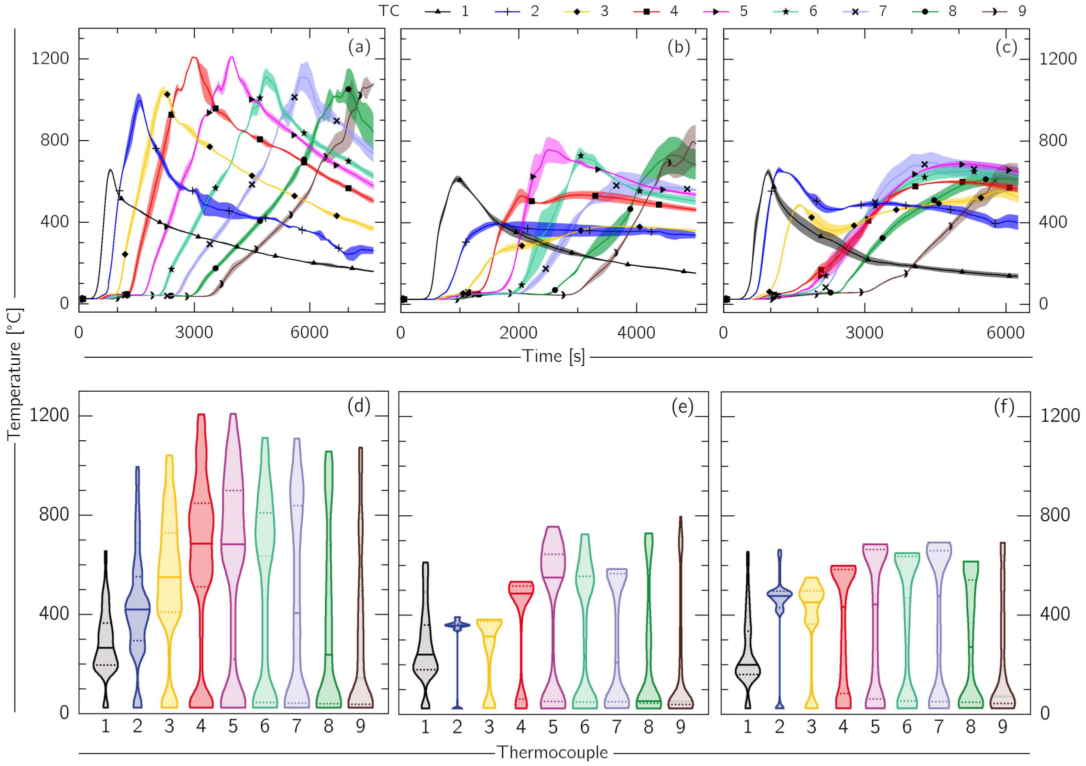

Figure 2.3: Temperature evolution for exp. 4 (a), 13 (b), and 15 (c). The shaded zones represents the average deviation. Temperature frequency distribution for exp. 4 (d), 13 (e), 15 (f). Continuous vertical lines represent median, and dashed vertical lines represent upper and lower quartiles. (Color version available on the web.)

in the low-temperature range of 25 °C to 100 °C. Also, it increased for the intermediate temperature range, from 250 °C to 900 °C (in the first half of the reactor), whereas, for temperatures above 900 °C, the TFD tended to be low during the whole experiment, in general.

As we introduced heterogeneity in the bed composition (exp. 13 and 15, Fig. 2.3e,f), the high frequencies were distributed in the extreme temperature ranges, from 25 °C to 100 °C and from 400 °C to 700 °C. Nevertheless, the maximum temperatures for these experiments' bed compositions decreased significantly compared to results from bed B_1 (exp. 4).

Noteworthy, the results suggested that it is mandatory to account for the data frequency to establish a representative LTP.

2.3.3 LTP analysis

Granted that the new combustion-driven reactor benefits from being self-sustained in terms of energy, it is not so simple to adequately define a reference temperature as setting up the temperature in tubular electric furnaces. In such devices, the thermostatic zone is located around the central region of the furnace [34, 35, 36]. The implication is converting a small sample size of just a few milligrams at a given reference temperature. Consequently, the conversion of relatively large sample size by extending the thermostatic zone along the reactor length is an optimization process.

On the other hand, in the combustion-driven reactor, the LTP must be established carefully. The use of temperature peak - to define the LTP [26, 30, 37] - is not correct since it is clear that the peak temperatures represent just a few seconds of the experiment time-scale (low TFD), overestimating the temperature profile. Fig. 2.4a,b shows the LTP differences obtained from temperature peaks and average-time temperature for some experiments. In the case of exp. 7, the temperature profile obtained from temperature peaks was overestimated in 70% from the actual temperature profile when we considered a reference zone between 175 mm and 225 mm along the pyrolysis chamber wall. Note that the actual temperature profile revealed the heat transfer effect in the reactor top and bottom, caused by heat losses through the walls.

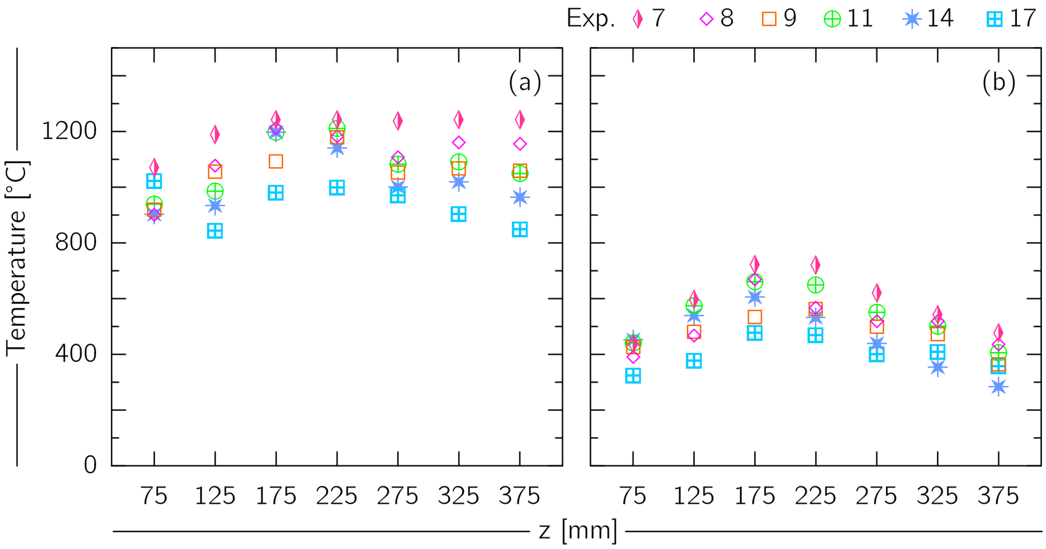

Figure 2.4: Longitudinal temperature profile obtained from (a) temperature peaks and (b) average-time temperature.

2.3.4 Sensitivity analysis

2.3.4.1 Dimensionless parameters

To investigate the influence of the input parameters on LTP, the reactor's dimensionless numbers based on Pi theorem is presented as follows. Setting as base variables T_z, the average longitudinal temperature in K, T_{in} the inlet air temperature in K, v_a, the inlet air velocity in m/s, Q, the bed higher heating value in MJ/kg, λ_m, the bed thermal conductivity in W/mK, c_{p_m}, the specific heat capacity at constant pressure in J/kgK, ρ_m, the bulking density in kg/m^3, r, the annular distance in m, and L, the reactor's characteristic length in m; and developing the relationship among the dimensionless groups, three numbers were obtained, Table 2.3. Similar numbers are presented in previous works of Dosanjh et al. [38].

Table 2.3: Dimensionless parameters governing the C-DPyR

$\Pi_1 = \frac{r v_a c_{p_m} T_z}{Q^{1.5} L}$	Energy by convection per chemical generation (varies from 10^{-8} to 10^{-7})
$\Pi_2 = \frac{v_a^2}{Q}$	Momentum by convection per chemical generation (varies from 10^{-6} to 10^{-5})
$\Pi_3 = \frac{\rho_m Q^{1.5} L}{T_{in} \lambda_m}$	Chemical generation per energy by diffusion (varies from 10^{11} to 10^{12})

A practical approach to show this influence was to present the governing dimensionless numbers in the logarithm base (Fig. 2.5). The log-log plot displayed straight lines showing that the relationship between the parameters Π_1 and Π_2 was a power-law type.

Solving for T_z, the relationship was expressed as $T_z = CQ^{\sigma}v_a^{\omega}$, where C, σ, ω are the constants limited to the range of experimental inputs (See Appendix C). For example, for $\log \Pi_3 = 12.3$, $C = 1.3 \times 10^{-4}$, $\sigma = 0.94$, $\omega = 0.12$, expressing results for T_z with a relative error around 1.4%. Thus, for $\log \Pi_3 = 11.7$ the relative error was up to 2.2%, and for $\log \Pi_3 = 11.5$ the error was around 2.1%.

Still in Fig. 2.5, by intersecting the common air velocities in each of Π_3 lines, the outcome also revealed linearity between the range of Π_3 and the air velocities, represented as dashed lines. The use of the angular coefficients to assess each input parameter's importance is a classical methodology [39]. Therefore, taking the ratio between the angular coefficients of the constant air velocity and the $\log(\Pi_3)$ lines, the effect of changing the latter on T_z is about twice as changing the former. Nevertheless, non-linear effects and individual interactions between the parameters can not be approached with this analysis.

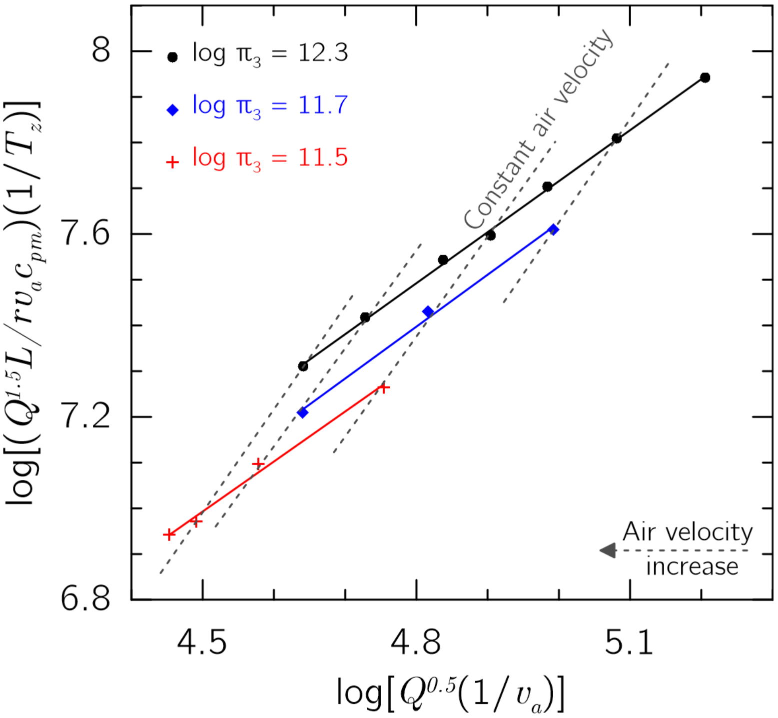

Figure 2.5: Empirical correlations between C-DPyR dimensionless numbers. $R^2 = 0.994$ for all plots. (●) $\log(1/\Pi_1) = 1.12 \log(1/\Pi_2) + 2.14$, (◆) $\log(1/\Pi_1) = 1.14 \log(1/\Pi_2) + 1.95$, (+) $\log(1/\Pi_1) = 1.09 \log(1/\Pi_2) + 2.07$. The dashed lines represent constant air velocity with angular coefficient of about 2.19

2.3.4.2 ANOVA

Table 2.4 reports the results calculated from the ANOVA F-test developed using sums of squares [33]. The sensitivity analysis showed that the bed composition ($P = 0.0001$) and air velocity ($P = 0.0045$) have a statistically significant effect on the LTP, rejecting the null hypothesis. Nevertheless, no interaction effects between the two variables were found ($P = 0.6407$), indicating that they are not dependent on each other. It implies that the operator might choose the more convenient input parameter to control the temperature.

Table 2.4: Analysis of variance for longitudinal temperature profile data

Source of variation	Sum of squares	Degrees of freedom	Mean square	F_0	P-value
Bed composition	106,389.50	1	106,389.50	719.05	0.0001
Air velocity	4,501.53	2	2,250.77	15.21	0.0045
Interaction	141.78	2	70.89	0.48	0.6407
Error	887.76	6	147.96	-	-
Total	111,920.57	11	-	-	-

2.3.5 C-DPyR operational constraints

Figure 2.6 summarized all experiments outcome by categorizing it varying the bed composition and fixing the air velocity (Figure 2.6a-c), and varying the air velocity fixing the bed composition (Figure 2.6d-f).

The C-DPyR thermal behavior is comparable to a common tubular furnace. For a thermostatic zone located around the middle of the reactor, 175mm $< z <$ 225mm, a temperature gradient range of $0.04-1.3$ °C/mm was obtained, as reported in References [34, 35, 36].

One alternative to avoid high longitudinal temperature gradients, from the middle to the top of the reactor, is to balance the heat flux per volume unit produced by the oxidation zone with a satisfactory heat-insulating at the top of the reactor. However, a poor heat-insulation combined with low heat generation from the heterogeneous bed provided distinct thermostatic zones ($z \approx 150$mm), such as those obtained in experiments 12, 15, 16, and 18 (Fig. 2.6). In these cases, the reactor application is indicated to treat waste materials, where drying, sterilizing, and reducing volume is desirable [8, 7], taking advantage of a higher volume of the pyrolysis chamber in comparison with lab-scale tubular furnaces [40, 41] that are limited for samples sizes of a few grams due to high energy consumption. For more controlled applications, such as materials synthesis processing [34, 35, 36] and conventional biomasses pyrolysis [5], it is required to improve insulation to gain a uniform LTP. Nevertheless, processes demanding an

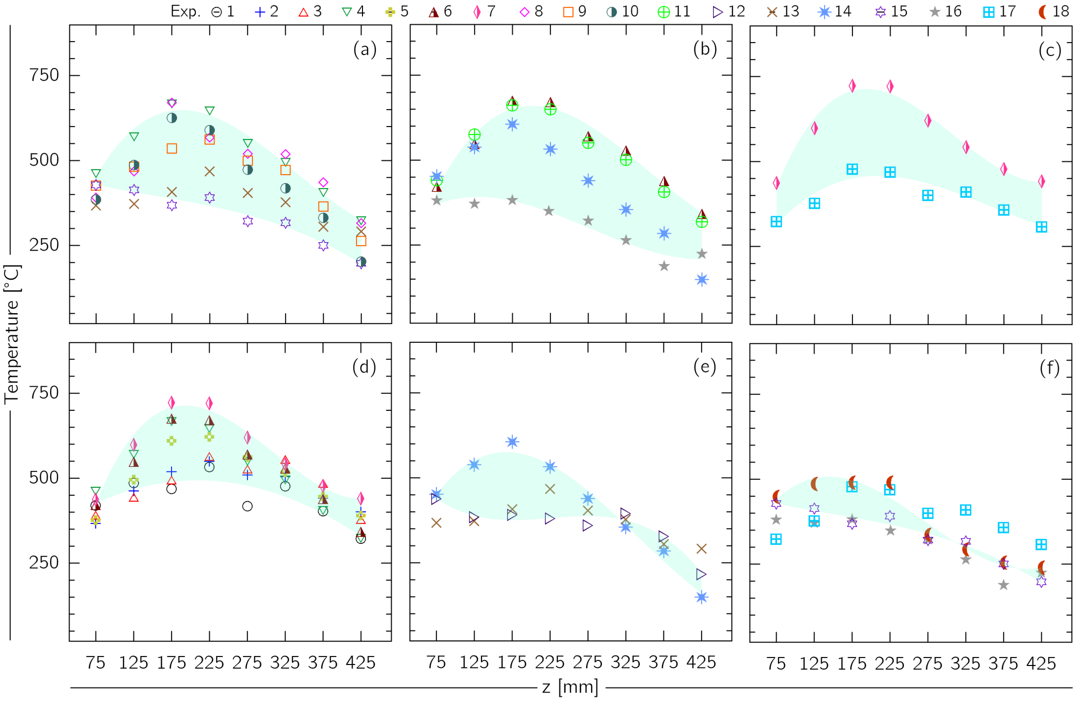

Figure 2.6: Longitudinal temperature profile obtained varying the bed composition and fixing the air velocity at (a) $5.9 \times 10^{-2} m/s$, (b) $8.9 \times 10^{-2} m/s$, and (c) $10.9 \times 10^{-2} m/s$, and varying the air velocity while fixing the bed composition at (d) B_1, (e) B_5, and (f) B_6.

accurate optimum temperature control might be laborious due to indirect control of the temperature.

The shaded areas in Fig. 2.6 indicate the relative control of the LTP obtained by varying air velocity and bed composition. One can observe that the temperature was more sensitive to the bed composition's control effect, represented by a larger shaded area. The contrary was noted while trying to control the temperature varying the air velocity for a given bed composition (Fig. 2.6e,f). Indeed, the air velocity control effect is diminished when the inlet air velocity stops the temperature increase drastically while cooling the combustion front, served as a heat convective sink.

Since the LTPs shown in Fig. 2.6 represent the profile obtained averaging each thermocouple's temperature in the runtime process (values in Table 2.1), the C-DPyR can provide the same interface wall heat flux spread over time, only by adjusting the input parameters. For instance, experiments 2 and 9 resulted in approximately the same heat flux for different runtimes, i.e., the C-DPyR can be controlled to work in different thermal resistance scenarios inside the pyrolysis chamber. Considering the ratio between convective and conductive resistances, represented as the Biot number, being much more than unity, i.e., a high-temperature gradient in the pyrolysis chamber, experiment 2 would provide sufficient time to heat all the pyrolysis chamber.

Still analyzing experiments 2 and 9, an energy balance verifies the net thermal energy available to the pyrolysis chamber, E_{net}[kWh/kg]= $E_{comb} - E_{hl} - E_{ig} - E_{comp}$. The output is respectively the energy generated from combustion, $E_{comb} = Q\frac{dm}{dt}t_{run}$ (5.0 kWh/kg and 4.2 kWh/kg), and the lost energies from ignition heater (average of 0.3 kWh/kg), air compressor consumption (1.1 kWh/kg and 0.3 kWh/kg), and walls, $E_{hl} = hA(T_e - T_\infty) + \epsilon\sigma T_e^4$ (1.6 kWh/kg and 0.5 kWh/kg). The balance is positive of about 2.1 kWh/kg and 3.0 kWh/kg, for experiments 2 and 9, respectively, representing the thermal energy available to the pyrolysis chamber. Table 2.5 shows the results from the energy balance expanded for all experiments ranging between +0.7 kWh/kg and +4.7 kWh/kg.

2.4 Conclusions and implications

A combustion-driven reactor was designed, built, and tested as a novel experimental device capable of performing pyrolysis of condensed phase matters heat-driven by smoldering low-grade fuels instead of electricity. Particular attention was paid to propose a representative longitudinal temperature profile based on the time-averaged method at each thermocouple position.

The C-DPyR was assessed under operating conditions of air velocities for typical

Table 2.5: Energy balance.

Exp.	n*	Bed	$E_{comb}(\times 10^4)$ [kWh/kg]	$E_{hl}(\times 10^4)$ [kWh/kg]	$E_{ig}(\times 10^4)$ [kWh/kg]	$E_{comp}(\times 10^4)$ [kWh/kg]	$E_{net}(\times 10^4)$ [kWh/kg]
1	1	B_1	5.8	1.8	0.3	1.2	2.5
2	1	B_1	5.0	1.6	0.3	1.1	2.1
3	1	B_1	5.8	0.9	0.3	0.6	4.1
4	4	B_1	5.6	0.9	0.3	0.6	3.8
5	1	B_1	5.7	0.8	0.4	0.5	4.1
6	1	B_1	5.7	0.5	0.3	0.3	4.6
7	1	B_1	5.7	0.5	0.2	0.3	4.7
8	1	B_2	4.5	0.6	0.3	0.4	3.1
9	1	B_3	4.2	0.5	0.3	0.3	3.0
10	1	B_4	2.9	0.4	0.2	0.3	2.0
11	1	B_4	3.6	0.4	0.2	0.3	2.8
12	1	B_5	2.1	0.6	0.3	0.4	0.8
13	4	B_5	2.3	0.4	0.3	0.2	1.4
14	1	B_5	2.3	0.2	0.1	0.1	1.9
15	4	B_6	1.6	0.4	0.2	0.3	0.7
16	1	B_6	1.7	0.1	0.2	0.1	1.2
17	2	B_6	1.5	0.1	0.2	0.1	1.1
18	2	B_6	1.7	0.2	0.1	0.1	1.3

*Number of repetitions.

lab-scale reactors and bed compositions simulating different fuels. The experiments' reliability was tested under twenty-nine runs - which presented an average deviation ranging from 30 to 54 °C for the experiment of homogeneous and heterogeneous beds -, and also through dimensionless analysis. The operation's success was confirmed by ANOVA, which revealed the independence of the input parameters (P = 0.6407) on defining the longitudinal temperature profile.

It is also worth ratifying that a self-sustaining combustion process carried enough energy to supply pyrolysis ranging from 1.5 to 5.8 kWh/kg of initial fuel mass. The consequence was a positive energy balance of 0.7 kWh/kg for the worst scenario and 4.7 kWh/kg for the best, even considering ignition and compressor consumptions and wall heat loss.

Additionally, the findings from the present study have some practical and theoretical implications. These include:

- Although the heterogeneous bed presented a propagation with all the complexities, it has shown a consistent repetition, which implies that other fuel mixtures can be considered for combustion.
- Temperature evolution time-averaging at each thermocouple position leads to a

more accurate representation of the LTP; therefore, it should be used to determine the average from the temperature in time acquisition.

- The dimensional and statistical analysis proved the temperature sensibility to the control of the combustion input parameters. The parameters can be adjusted to overcome operational contraints such as poor heat insulation or adapt to the type of material that will be converted, such as plastic, biosolids, sludge, and feces.
- the C-DPyR can be controlled to work in different thermal resistance scenarios inside the pyrolysis chamber. Thus, the problem of heat transfer insufficiency in scaling-up can be mitigated.
- The heat balance proves that the heat released by combustion can be driven and sustain an energy-intensive process, indicating the C-DPyR potential of converting wet materials.

Bibliography

[1] Poritosh Roy and Animesh Dutta. Life cycle assessment (lca) in municipal waste management decision making. In *Plastics to Energy*, pages 377–402. Elsevier, 2019.

[2] D Czajczyńska, L Anguilano, H Ghazal, R Krzyżyńska, AJ Reynolds, Nik Spencer, and Hussam Jouhara. Potential of pyrolysis processes in the waste management sector. *Thermal Science and Engineering Progress*, 3:171–197, 2017.

[3] Yaning Zhang, Yunlei Cui, Paul Chen, Shiyu Liu, Nan Zhou, Kuan Ding, Liangliang Fan, Peng Peng, Min Min, Yanling Cheng, et al. Gasification technologies and their energy potentials. In *Sustainable Resource Recovery and Zero Waste Approaches*, pages 193–206. Elsevier, 2019.

[4] Pooja Ghosh, Subhanjan Sengupta, Lakhveer Singh, and Arunaditya Sahay. Life cycle assessment of waste-to-bioenergy processes: a review. In *Bioreactors*, pages 105–122. Elsevier, 2020.

[5] Ayhan Demirbas and Gönenç Arin. An overview of biomass pyrolysis. *Energy sources*, 24(5):471–482, 2002.

[6] AM Li, XD Li, SQ Li, Y Ren, N Shang, Y Chi, JH Yan, and KF Cen. Experimental studies on municipal solid waste pyrolysis in a laboratory-scale rotary kiln. *Energy*, 24(3):209–218, 1999.

[7] João Vitor F Duque, Márcio F Martins, Gérald Debenest, and Marcos Tadeu D'Azeredo Orlando. The influence of the recycling stress history on ldpe waste pyrolysis. *Polymer Testing*, page 106460, 2020.

[8] Flávio Lopes Francisco Bittencourt, Atílio Barbosa Lourenço, Elias Antônio Dalvi, and Márcio Ferreira Martins. Thermodynamic assessment of human feces gasification: an experimental-based approach. *SN Applied Sciences*, 1(9):1077, 2019.

[9] Daniel Neves, Henrik Thunman, Arlindo Matos, Luís Tarelho, and Alberto Gómez-Barea. Characterization and prediction of biomass pyrolysis products. *Progress in Energy and Combustion Science*, 37(5):611–630, 2011.

[10] Dinesh Mohan, Charles U Pittman Jr, and Philip H Steele. Pyrolysis of wood/biomass for bio-oil: a critical review. *Energy & fuels*, 20(3):848–889, 2006.

[11] Jerome A Ramirez and Thomas J Rainey. Comparative techno-economic analysis of biofuel production through gasification, thermal liquefaction and pyrolysis of sugarcane bagasse. *Journal of Cleaner Production*, 229:513–527, 2019.

[12] A Downie, P Munroe, P Klatt, and R Downie. Slow pyrolysis: Australian demonstration plant successful on multi-feedstock's. 2007.

[13] Mohammad I Jahirul, Mohammad G Rasul, Ashfaque Ahmed Chowdhury, and Nanjappa Ashwath. Biofuels production through biomass pyrolysis—a technological review. *Energies*, 5(12):4952–5001, 2012.

[14] Muhammad Saad Qureshi, Anja Oasmaa, Hanna Pihkola, Ivan Deviatkin, Anna Tenhunen, Juha Mannila, Hannu Minkkinen, Maija Pohjakallio, and Jutta Laine-Ylijoki. Pyrolysis of plastic waste: opportunities and challenges. *Journal of Analytical and Applied Pyrolysis*, 152:104804, 2020.

[15] Maria Laura Mastellone, F Perugini, M Ponte, and Umberto Arena. Fluidized bed pyrolysis of a recycled polyethylene. *Polymer degradation and stability*, 76(3):479–487, 2002.

[16] Xiqiang Zhao, Jian Zhang, Zhanlong Song, Hongzhen Liu, Longzhi Li, and Chunyuan Ma. Microwave pyrolysis of straw bale and energy balance analysis. *Journal of analytical and applied pyrolysis*, 92(1):43–49, 2011.

[17] Hossam A Gabbar, Mohamed Aboughaly, and Awais Choudhary. An energy evaluation for thermal conversion of thermoplastic waste to refined oil products using pyrolysis reaction process system. *International Journal of Process Systems Engineering*, 4(1):65–79, 2016.

[18] Jacques Lédé and Olivier Authier. Temperature and heating rate of solid particles undergoing a thermal decomposition. which criteria for characterizing fast pyrolysis? *Journal of Analytical and Applied Pyrolysis*, 113:1–14, 2015.

[19] F-X Collard, M Carrier, and JF Görgens. Fractionation of lignocellulosic material with pyrolysis processing. In *Biomass Fractionation Technologies for a Lignocellulosic Feedstock Based Biorefinery*, pages 81–101. Elsevier, 2016.

[20] JP Tagutchou, F Mermoud, E Martin, S Salvador, et al. A new experimental continuous fixed bed reactor to characterise wood char gasification. *Fuel*, 89(11):3320–3329, 2010.

[21] Youhong Sun, Fengtian Bai, Baochang Liu, Yumin Liu, Mingyi Guo, Wei Guo, Qiuwen Wang, Xiaoshu Lü, Fang Yang, and Yang Yang. Characterization of the oil shale products derived via topochemical reaction method. *Fuel*, 115:338–346, 2014.

[22] You-Hong Sun, Feng-Tian Bai, Xiao-Shu Lü, Qiang Li, Yu-Min Liu, Ming-Yi Guo, Wei Guo, and Bao-Chang Liu. A novel energy-efficient pyrolysis process: self-pyrolysis of oil shale triggered by topochemical heat in a horizontal fixed bed. *Scientific reports*, 5:8290, 2015.

[23] Mathieu Milhé, Laurent van de Steene, Michaël Haube, Jean-Michel Commandré, Wanignon-Ferdinand Fassinou, and Gilles Flamant. Autothermal and allothermal

pyrolysis in a continuous fixed bed reactor. *Journal of Analytical and Applied Pyrolysis*, 103:102 – 111, 2013. Pyrolysis 2012.

[24] José L Torero, Jason I Gerhard, Marcio F Martins, Marco AB Zanoni, Tarek L Rashwan, and Joshua K Brown. Processes defining smouldering combustion: Integrated review and synthesis. *Progress in Energy and Combustion Science*, 81:100869, 2020.

[25] Thomas J Ohlemiller. Modeling of smoldering combustion propagation. *Progress in Energy and Combustion Science*, 11(4):277–310, 1985.

[26] FAF Monhol and MF Martins. Cocurrent combustion of human feces and polyethylene waste. *Waste and Biomass Valorization*, 6(3):425–432, 2015.

[27] Marco AB Zanoni, José L Torero, and Jason I Gerhard. Delineating and explaining the limits of self-sustained smouldering combustion. *Combustion and Flame*, 201:78–92, 2019.

[28] L Kinsman, J Gerhard, J Torero, G Scholes, and C Murray. Upscaling self-sustaining treatment for active remediation (star): Experimental study of scaling relationships for smouldering combustion to remediate soil. *AGUFM*, 2013:H41H–1351, 2013.

[29] Gabriel Sabadell, David Thomas, Paul Bireta, Grant Scholes, Cody Murray, Benoit Boulay, Gavin Grant, Dave Major, et al. Treatment of oil-impacted soil and oily waste: Overview of two field demonstration projects. In *SPE International Conference and Exhibition on Health, Safety, Security, Environment, and Social Responsibility*. Society of Petroleum Engineers, 2018.

[30] Marcio F Martins, Sylvain Salvador, J-F Thovert, and Gerald Debenest. Co-current combustion of oil shale–part 1: Characterization of the solid and gaseous products. *Fuel*, 89(1):144–151, 2010.

[31] Marcio F Martins, Sylvain Salvador, J-F Thovert, and Gerald Debenest. Co-current combustion of oil shale–part 2: Structure of the combustion front. *Fuel*, 89(1):133–143, 2010.

[32] Ayhan Demirbaş. Properties of charcoal derived from hazelnut shell and the production of briquettes using pyrolytic oil. *Energy*, 24(2):141–150, 1999.

[33] Douglas C Montgomery. *Design and analysis of experiments.* John wiley & sons, 2017.

[34] Xunxiang Hu, Kurt A Terrani, Brian D Wirth, and Lance L Snead. Hydrogen permeation in fecral alloys for lwr cladding application. *Journal of Nuclear Materials*, 461:282–291, 2015.

[35] Ashoka Nukkanahalli Venkataswamy, George Thomas Chirayil, and Srinivasan Kannaiyan. Investigation of structural formation of starting composition 2245 in the bi-pb-sr-ca-cu-o system superconductors. *Journal of Solid State Physics*, 2014, 2014.

[36] Franz J Dutz, Andreas Heinrich, Rolf Bank, Alexander W Koch, and Johannes Roths. Fiber-optic multipoint sensor system with low drift for the long-term monitoring of high-temperature distributions in chemical reactors. *Sensors*, 19(24):5476, 2019.

[37] Tarek L Rashwan, Jason I Gerhard, and Gavin P Grant. Application of self-sustaining smouldering combustion for the destruction of wastewater biosolids. *Waste management*, 50:201–212, 2016.

[38] S Dosanjh, J Peterson, AC Fernandez-Pello, and PJ Pagni. Buoyancy effects on smoldering combustion. *Acta Astronautica*, 13(11-12):689–696, 1986.

[39] Max D Morris. Factorial sampling plans for preliminary computational experiments. *Technometrics*, 33(2):161–174, 1991.

[40] Yayun Zhang, Dengle Duan, Hanwu Lei, Elmar Villota, and Roger Ruan. Jet fuel production from waste plastics via catalytic pyrolysis with activated carbons. *Applied Energy*, 251:113337, 2019.

[41] Diyar Tokmurzin, Botagoz Kuspangaliyeva, Berik Aimbetov, Bexultan Abylkhani, Vassilis Inglezakis, Edward J Anthony, and Yerbol Sarbassov. Characterization of solid char produced from pyrolysis of the organic fraction of municipal solid waste, high volatile coal and their blends. *Energy*, 191:116562, 2020.

Chapter 3

Self-sustaining combustion in annular space: an alternative heat source for waste conversion

---

Contents

Summary

In this chapter, the main aspects of smoldering front propagation in an annular section were shown based on homogeneous and heterogeneous bed compositions and different inlet airflow to propagate the combustion front. The combustion front thermochemical characteristics were assessed through new contributions in the classical methodologies of establishing the longitudinal temperature profile, calculating the front velocity, and determining the combustion regime and front structure.

The experimental data reliability was tested by analyzing the standard deviations of the temperature evolution curves and flue gas analysis.

All experiments were self-sustaining, and the temperature evolution curves showed a similar behavior compared with the classical smoldering experiments in non-annular volumes. The time-average method proposed to determine the longitudinal temperature profile led to consistent results, and, from them, the heat fluxes to the pyrolysis chamber wall could be determined. Two methods were used to calculate the front velocity. In general, despite the heterogeneous beds' complexity, the front velocity followed a linear trend as airflow was increased, and constant to increasing velocities profiles were observed.

A mass balance was modeling to establish the smoldering propagation regime and determine reactions stoichiometry based on the experimental front velocity and gas analysis. The model returned the equivalence ratio (ER), the total oxygen mass, front velocity correction, and the actual amount of fixed carbon oxidized by the front. It was evidenced by the ER results and the high levels of CO and H_2 in the flue gas that the combustion front propagates under a gasification regime. Details about the combustion front structure were assessed by calculating the thermal and chemical fronts velocities. The analysis showed that the oxidation reaction's heat was mostly convected downstream of the reaction front in the homogeneous and heterogeneous beds. That helped increase the average longitudinal temperature in both scenarios analyzed, increasing the airflow rate and increasing the bed heterogeneities by stimulating endothermic reactions.

A case study was finally developed to demonstrate that the combustion-driven pyrolysis reactor, C-DPyR, can be employed as an alternative device to perform pyrolysis of waste. The energy available drive for pyrolysis was more than sufficient in all experiments conducted, even using a low-grade fuel in the C-DPyR as a heat source.

Candidate contribution: Conceptualization, methodology, software, validation, formal analysis, resources, data curation, writing - original draft, Writing - review & editing, visualization.

3.1 Introduction

Waste conversion technologies are commonly associated with non-incineration technologies used to convert the non-recyclable solid portion of the municipal waste stream to electricity, fuels, or chemical feedstocks. The most investigated technologies are based on the following processes: gasification [1], plasma arc gasification [2, 3], pyrolysis [4], hydrolysis/fermentation [5], anaerobic digestion [6], autoclave/mechanical processing [7]. Moreover, recently, the smoldering process was scaled-up to serve this purpose as well [8]. Each of these technologies has advantages: emission control, feedstock flexibility, and a wide range of end-product opportunities [9, 10]. The disadvantages, however, lie in gas cleaning equipment cost [11], understanding the degradation mechanism is crucial for scale-up [12, 13], and low system efficiency or high system costs [14].

The smoldering thermal process is based on forcing air through a material bed to propagate a low- to high-temperature flameless combustion form. This process has the main advantage of self-sustaining the reaction releasing a relatively large amount of heat that can be used for various ends [15, 16, 17, 18, 19]. The purpose ends, in its turn, is linked to how the heat will be used. In the in-bed process, both the materials sharing the same bed where the front is propagating and the so-called thermochemical front structures are managed to allow the front' heat to destroy most of the waste [20, 21]. For the first time launched in this work, the out-of-bed heat use process, the focus is the heat crossing the reactor walls. Thus, the reactor is designed to take advantage of the thermochemical front structure to recover most of the energy from combustion to drive the heat for a heat-intensive secondary process.

Regardless of the heat use strategy to be employed, in controlled smoldering experiments, key operational parameters such as injected air flux, bed composition with homogeneous mixtures, or heterogeneous mixtures affect the system performance. The literature reports wide-ranged results focused on these parameters' effect on smoldering front propagation in cylindrical reactors [8, 22, 23]. For all of these studies, the in-bed use of the heat released by combustion was investigated.

Monitoring of the propagating combustion front to describe the front structure or determine the combustion regime for these systems is still in its early stages. It is understandable because the temperature inside the reactor can easily surpass 1000 °C melting the instrumentation; while, the methodologies are limited to the interpretation of temperature data versus time that describes the combustion front structure qualitatively. Separately, a few attempts were made using infra-red measurements [16, 24] or local measurements [21]. However, there is still a need for other methods or methodologies for interpreting the temperature data acquisition.

In terms of the combustion front structure, at least the relative position in the bed between the heat transfer front and the oxidation front [25, 26, 27] could be determined using the bed and feed air properties (resulting in the velocity of the thermal, v_T, and chemical front, v_f). Therefore, the maximum energy accumulation in the bed, denoted by the maximum temperature that a given propagation can attain, $T_{z,teo}$, could be established by knowing the fronts' overlap degree. However, due to either the bed heterogeneities [8] and shrinkage (the case of almost all solid wastes undergoing thermal conversion), the filtration combustion theory is limited [28].

Another viewpoint on the combustion structure consists of establishing the smoldering propagation regimes related to fuel and oxygen interaction; that is, the flue gases need to be analyzed. In general, the smoldering literature neglects the smoldering process's product information, reinforcing the marginal aspect of establishing the regime. Nevertheless, smoldering experiments are similar to gasification in some aspects. For example, pyrolysis (or devolatilization) gases are the smoldering products that can be recovered [21, 23]. For this reason, we are introducing in the present work the use of the concept of equivalence ratio (ER) to determine the smoldering front propagation regime. ER is defined as the ratio of the actual air/fuel ratio (A/F) to the stoichiometric air/fuel ratio $(A/F)_{stoic}$, such as $ER = \frac{(flow\ rate\ of\ air\ supply)\times(runtime)}{(mass\ input\ of\ fuel)\times(A/F)_{stoic}}$ [1, 29]. In this respect, we can classify the smoldering regime as pure smoldering ER = 1, partial gasification regime, $0.45 < \text{ER} < 1$, and gasification regime, when ER is within the range for ideal and theoretical gasification, 0.19–0.43.

Although we are demonstrating, for the first time, a new reactor design for out-of-bed heat recovering, this work aims to investigate the classical aspects of smoldering front propagation while presenting new concepts and making new contributions in the classical methodology of establishing the longitudinal temperature profile, of calculating the front velocity, and of determining the basic structure of combustion front.

This new design propagates the combustion front in an annular section pathway rather than a circular. In this regard, some previous works [21, 30] were used to support the argument that two concentric cylinders arrangement, i.e., the inner cylinder wrapped by a smoldering bed, is, at present, the best configuration for recovering, through the cylinder wall, most of the heat released by the combustion front. According to Martins et al. [21] analysis of the front shape, the front is a curved surface with a hill (maximum temperature) around the reactor's axis.

3.2 Experimental device

A new design of smoldering combustion reactor, Figure 3.1, was developed to study the characteristics of a combustion front propagation in an annular section, the Combustion-

Driven Pyrolysis Reactor (C-DPyR). Two stainless steel tubes with circular sections were arranged vertically in a coaxial configuration giving rise to two independent chambers here defined as combustion chamber and pyrolysis chamber. Although the chambers' inlet and outlet followed independent paths; the heat transfer occurred through the interface wall. Fig. 3.1 shows the reactor sketch.

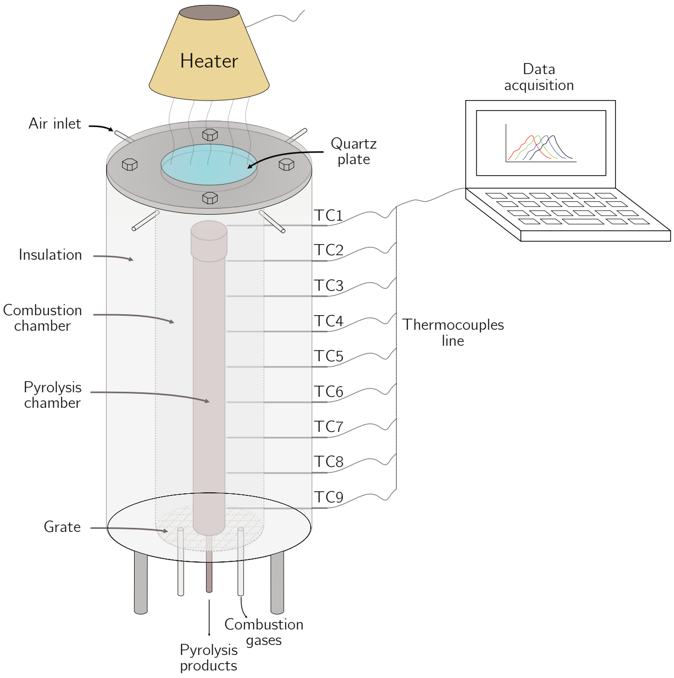

Figure 3.1: Combustion-driven pyrolysis reactor, C-DPyR.

The combustion chamber (the outer stainless steel cylinder of 73 mm diameter and 450 mm height, wrapped by a heat-insulating layer of 50 mm - blanket Superwool 607) consists of the annular region in which the combustion front is propagated. At the top, it has a main inlet through which the reactor is fed with solid fuel and, also, small auxiliary inlets used for compressed air injection (MFC 8741, 0-30 Nl/min, Burkert Ltda). The reactor is sealed by a quartz disk sandwiched between flexible graphite gasket rings held by a stainless steel flange. At the bottom, a grate and two small tubes allow the flue gas exhaustion. Nine thermocouples (TC) type-K (3 mm diameter) were positioned at the reactor's longitudinal axis, one every 50 mm, to measure the combustion front's temperature at the interface wall along with the height.

For the ignition process, a controlled conical-spiral heater (1600 W - 220 V AC) is placed at the reactor's top to supply the ignition's required radiant energy.

The pyrolysis chamber is located coaxially in the center of the reactor, where thermochemical conversions of materials can be performed. It has an inlet that can be closed or not by a screw-on metallic cap to allow or prevent the sample's contact with the inlet air. The heat released by combustion is transferred through the top and sidewalls to drive the material's thermal conversion. At the bottom, an outlet allows the exit of the products.

The experimental protocol's first stage consists of preparing and characterizing the solid fuel that will compose the particle bed. The reactor is then filled and sealed. The desired inlet airflow is initiated and kept constant by a mass flow controller. For the ignition process, a conical spiral heater with PID temperature control is placed above the reactor and serves as a radiant energy source. An insulator shield blocks the reactor's quartz windows until the heater reaches 700 °C. The shield is then removed, and the radiation passes through the quartz disk and reaches the bed's surface. When TC_1 reaches its peak, the resistance is turned off, and the energy released by combustion might sustain the propagation. Electricity consumption during ignition is recorded by a digital power meter.

The propagation of the combustion front is monitored through temperature measurement and flue gas analysis. The thermocouples signals are recorded by a data acquisition device every second of the whole experiment. At the reactor's exit, the gas analysis is performed online during ignition and globally during the experiment through extractions of gas samples performed at the peak of TC_3, TC_5, and TC_7. The volume fraction of CO_2 was analyzed by NDIR and O_2, CO, NO, H_2, NO_2, and C_xH_y by electrochemical cells. The detection limits are 0.01 vol.% O_2, 1 ppm CO, 1 ppm NO, 0.1 ppm NO_2, 1 ppm H_2, 0.01 vol.% CO_2, and 10 ppm C_xH_y. Once all thermocouples have registered their peak temperature, indicating the cooling process's predominance, the inlet airflow is interrupted, and the experiment is considered finished.

3.2.1 Longitudinal temperature profile

Since the smoldering propagation is a transient process, obtaining a longitudinal temperature profile (LTP) representing the whole experiment is not trivial. The only attempt reported in the literature is the use of temperature peak [19, 21, 31]; however, it is noteworthy that the TCs peaks represent just a few seconds of the experiment timescale, overestimating the temperature level to use as a longitudinal profile. Therefore, we propose a time-average method where at each thermocouple position the temperature evolution is defined by $\int_0^t T(t)dt/\int_0^t dt$. The result is a longitudinal temperature profile with n points (n is the number of thermocouples). The LTP can be used to fit a representative function and to obtain the heat flux driven from the combustion front to the pyrolysis chamber.

3.2.2 Methods for front velocity estimation

The front propagation velocity calculation is focused on quantifying the rate of solid fuel consumption during combustion. Two different methodologies were applied, one more suitable for experiments with well-defined temperature evolution pattern (**tavg** method) and other for general patterns (**dmdt** method).

From the interpretation of the temperature evolution data, the front velocity was calculated by $v_f = (z_n - z_{n-1})/(t_n - t_{n-1}), n = 2, 3, ..., 9$. Where n is the thermocouple number, z is the thermocouple position and t is the average time corresponding to the inflection points in the first-derivative temperature curve. The relevant time intervals were chosen in the temperature-rise segment for the thermocouples n and $n-1$, the reason in which the method is called **tavg**, the sketch in Figure 3.2 shows how the specific times intervals are selected.

The second method, called **dmdt**, is a global estimative of the front velocity using the following experimental data: initial sample mass m_0; mass post-combustion m_f; runtime Δt (the time interval between the TC_1 and TC_9 peak); apparent bed density ρ_b; and annular section area A_s. The equation is defined by $v_f = \frac{m_0 - m_f}{\Delta t} \frac{1}{\rho_b A_s}$.

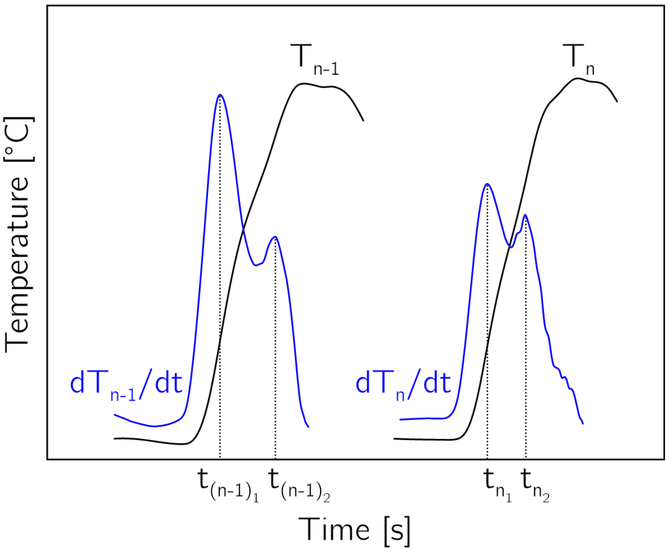

Figure 3.2: Calculation of the combustion front velocity.

3.3 Measurements reliability

Twenty-nine (29) experiments were performed using two input parameters: the inlet air and bed composition. The latter was planned to comprehend two types of beds: one homogeneous (charcoal grains), other heterogeneous mixtures of charcoal grains, and $NaHCO_3$ powder. Here, we supposed that the mixture of these two materials might engender spatial permeability changes in the medium since both materials have different densities; therefore, their mixture becomes difficult due to filling the reactor while maintaining a homogeneous mixture.

The charcoal grains have irregular geometries with a density of 640 kg/m^3 and 2 mm$< dp <$ 4 mm. While the $NaHCO_3$ is fine powder particles of diameter order of 100 µm and a density of 2200 kg/m^3. The charcoal bed's bulk density was between 311 - 352 kg/m^3, and for heterogeneous bed in the range of 408 kg/m^3 to 564 kg/m^3. Table 3.1 summarizes all experiments and presents the materials as a function of proximate composition (based on [32, 33, 34, 35]). The experiments were run with an airflow rate between 6 Nl/min and 24 Nl/min. That corresponds to a Darcy air velocity in the range 0.03 - 0.12 m/s at 20 °C.

The experiments were first run randomly, and then the results were analyzed to ascertain the general trend and then choose the bed configurations to assess the reproducibility. Experiments 4, 13, and 15 were selected and repeated four times (n = 4). The standard deviation of the two primary measurements, temperature evolution, and gas analysis, are displayed in Figure 3.3 and Figure 3.4.

The averaged temperature evolution (continuous line) and the respective standard deviations (shaded zone) are shown in Figure 3.3. For the Exp. 4 (Figure 3.3a), the charcoal grains' bed, the maximum standard deviation was around 30 °C. Given the complexity brought by the mixture charcoal/$NaHCO_3$ (Exp. 13 and 15, Figure 3.3b,c), the heterogeneous beds, a slightly higher deviation was calculated, 39 °C and 54 °C, for 33 wt.% and 50 wt.% of $NaHCO_3$ in the mixture, respectively.

It is noteworthy that the maximum standard deviations were located in the cooling zones of the temperature curve, contributing to increasing the average standard deviation, mainly for the front propagating in the heterogeneous bed. Indeed, these can be considered low standard deviations, emphasizing that the repetitions and their measurements were very consistent, despite the apparent complexity imposed in working with heterogeneous bed mixtures. It suggests that the temperature behavior of the other experiments followed the same trend.

Ratifying the data reliability, Figure 3.4 shows the average standard deviation of gas yields at the reactor exit. The maximum deviations observed for O_2, CO, and CO_2 were

0.4 vol.%, 1.1 vol.%, and 0.8 vol.%, respectively.

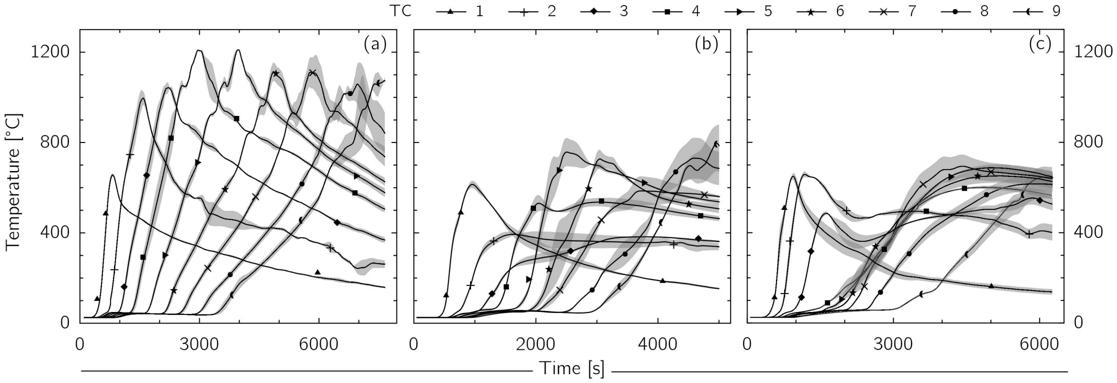

Figure 3.3: A typical plot of temperature evolution for a annular section. (a) Exp. 4 (100 wt.% charcoal, 12 Nl/min), (b) Exp. 13 (67 wt.% charcoal and 33 wt.% $NaHCO_3$, 12 Nl/min), (c) Exp. 15 (50 wt.% charcoal and 50 wt.% $NaHCO_3$, 12 Nl/min). Each shaded zone represents the standard deviation of its respective thermocouple.

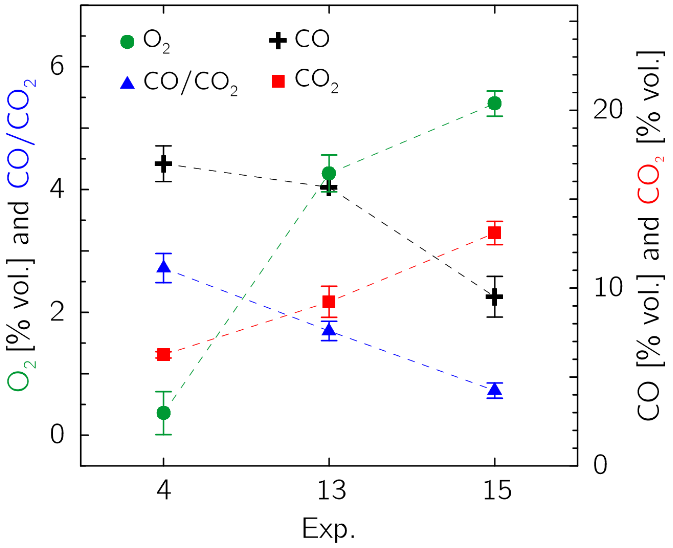

Figure 3.4: Flue gas composition with standard deviation.

Table 3.1: Input parameters and summarized results for different runs.

		Input parameters						Response variables									
Exp.	n*	FC [wt.%]	VM [wt.%]	MC [wt.%]	Ash [wt.%]	IM [wt.%]	ϕ_{air} [Nl/min]	T_z [°C]	Runtime [s]	$dm/dt(\times10^2)$ [g/s]	$v_f(\times10^5)$ [m/s]	O_2 [vol.%]	H_2 [vol.%]	CO [vol.%]	CO_2 [vol.%]	CO/CO_2	EA [% J/J]
1	1	58.8	28.4	3.4	9.4	0	6	464	13816	3.3	4.6	0.5	3.3	9.3	16.5	0.6	98
2	1	58.8	28.4	3.4	9.4	0	8	479	12636	3.1	5.5	0.1	4.6	12.1	11.9	1.0	96
3	1	58.8	28.4	3.4	9.4	0	10	494	6990	6.6	7.9	0.5	4.4	15.8	13.8	1.1	93
4	4	58.8	28.4	3.4	9.4	0	12	542	6824	6.1	7.8	0.4	5.0	17.0	6.2	2.7	92
5	1	58.8	28.4	3.4	9.4	0	14	518	5537	7.3	10.4	0.4	7.9	24.2	7.5	3.2	87
6	1	58.8	28.4	3.4	9.4	0	18	550	3668	11.0	12.5	0	9.9	29.1	8.0	3.6	84
7	1	58.8	28.4	3.4	9.4	0	22	588	3196	12.3	15.8	0	10.0	35.8	8.1	4.4	83
8	1	49.0	23.7	19.5	7.8	0	12	510	5420	8.5	9.2	0.7	4.3	14.4	13.5	1.1	94
9	1	42.0	20.3	31.0	6.7	0	12	477	4693	11.1	9.8	0.6	3.3	13.8	14.6	0.9	95
10	1	47.9	22.7	2.7	7.5	20.1	12	473	4216	8.1	5.5	4.7	6.1	17.6	6.5	2.7	87
11	1	47.9	22.7	2.7	7.5	20.1	18	540	3616	11.6	7.9	4.7	8.6	20.1	4.5	4.5	84
12	1	39.2	19.9	2.2	6.3	33.3	8	382	6631	5.2	3.1	-	-	-	-	-	86
13	4	39.2	19.9	2.2	6.3	33.3	12	386	3841	9.4	5.6	4.3	4.9	15.7	9.2	1.7	73
14	1	39.2	19.9	2.2	6.3	33.3	18	458	2116	17.7	10.5	5.1	7.6	17.3	7.1	2.4	73
15	4	29.4	14.2	1.7	4.7	50.0	12	356	5231	7.9	3.9	5.4	4.5	9.5	13.1	0.7	84
16	1	29.4	14.2	1.7	4.7	50.0	18	345	1390	28.7	15.1	5.2	4.7	13.6	10.5	1.3	11
17	2	29.4	14.2	1.7	4.7	50.0	22	402	994	36.6	18.8	5.2	5.0	14.2	10.2	1.4	16
18	2	29.4	14.2	1.7	4.7	50.0	24	389	2537	18.0	8.5	5.3	6.2	14.5	10.0	1.4	72

*Number of repetitions. FC: fixed carbon, VM: volatile matter, MC: moisture content, IM: inorganic matter.

3.4 Self-sustaining combustion in annular section

3.4.1 Temperature evolution

The thermocouples inside the combustion chamber, taking measurements at the interface wall, showed a similar behavior compared with the classical smoldering experiments in non-annular volumes. In general, all experiments were self-sustaining, considering a qualitative criterion of observing a sharp rise - indicating ignition processes taking place - in the temperature signal for all thermocouples. However, some particularities can be pointed out for both bed types.

For the homogeneous bed (Fig. 3.5a), a well-defined propagation pattern was observed, in which the thermocouples peaked in different instants, with visually fixed time steps. As the mixture became heterogeneous ($NaHCO_3$), the propagation pattern started to change, as observed in Fig. 3.5b, where the thermocouples TC_6 - TC_9 start to reveal a plateau after the sharp temperature rise, indicating a stark reduction of the cooling rate. The experiments showed in Fig. 3.5a, b, the regular propagation pattern suggests that the bed shrinks as the oxidation front propagates downwards.

Conversely, the experiment showed in Fig. 3.5c revealed a quasi-simultaneous ignition at all thermocouple positions suggesting that $NaHCO_3$ conductivity drives the heat used to start the experiment, from top to bottom. It is noteworthy that $NaHCO_3$ thermal conductivity is around thirteen times higher than the charcoal [36], maximizing the heat conduction through the bed. However, once it reached the $NaHCO_3$ pyrolysis activation temperature, an intensive competition between the heat released by charcoal oxidation and the heat sunk by $NaHCO_3$ pyrolysis shifts the temperature curve forming a plateau along the bed.

The classical temperature plateau around 60 °C, due to the water condensation [21], could be observed in all experiments. Supplementary temperature evolution plots are available in Appendix D.

3.4.2 Front velocity

Fig. 3.6 shows the average front velocity calculated for the homogeneous beds using **tavg** method (Fig. 3.6a), and for the heterogeneous beds using **dmdt** method (Fig. 3.6b). Although the two methods widely reported in the literature [19, 22] are accurate for determining the velocity for a stable front propagation - where the peak in temperature is unique, and the sharp temperature rise has visually fixed time-steps, these methods are not reliable for calculating the front velocity for the combustion propagation pattern

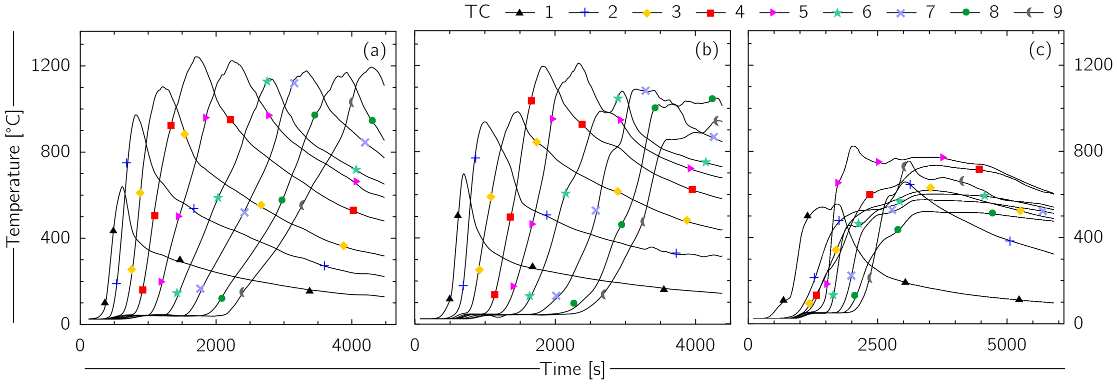

Figure 3.5: (a) Temperature evolution for homogeneous bed, Exp. 6 (100 wt.% charcoal, 18 Nl/min). (b) and (c) Temperature evolution for heterogeneous bed, Exp. 11 (80 wt.% charcoal and 20 wt.% $NaHCO_3$, 18 Nl/min) and Exp. 16 (50 wt.% charcoal and 50 wt.% $NaHCO_3$, 18 Nl/min), respectively.

such as presented in Fig. 3.5c. Here, we focused on the relationship between the average front velocity and the airflow rate that delineates the mass consumption's global behavior based on the oxygen-limited or reaction-limited propagation regimes, as reported in [37]. The front velocity followed a linear trend as airflow was increased from 8 to 22 Nl/min (Fig. 3.6). This linear behavior is similar to the majority of literature-reported experiments [38]. Nonetheless, for the bed with 50 wt.% of $NaHCO_3$, when the airflow increased from 22 Nl/min, the combustion regime changes from oxygen-limited to convective cooling [37].

Aside from this linear behavior, the presence of $NaHCO_3$ at 50 wt.% clearly increased the average front velocity in the heterogeneous bed compared to the homogeneous bed, for the range of 12 to 22 Nl/min. Since the heat transfer and chemical reaction fronts are independent, as reported in [20], each front progresses with its velocity. As suggested by Fig. 3.5c, the heat transfer front crosses the bed, leaving the reaction fronts behind. It looks as though the reaction trailing structure governs the propagation pattern. The outcome is that an accurate method to calculate the front velocity for these cases follows an instantaneous **dmdt** method instead of a global approach [21]. Therefore, it seems that the velocity calculated from the global **dmdt** might be overestimated.

Fig. 3.7 shows the difference between the average velocity calculated by both methods. In one case, for the experiments with homogenous beds, this difference remains constant, implying that the actual front velocity value is between the extremes. In the other case, the difference increases as the bed heterogeneity increases for the heterogeneous beds, at the point that **tavg** becomes inaccurate (experiments 16 - 18). Note that if, on the one hand, both methods overestimate the average velocities, on the other, it is not a coincidence that they follow the general velocity trend.

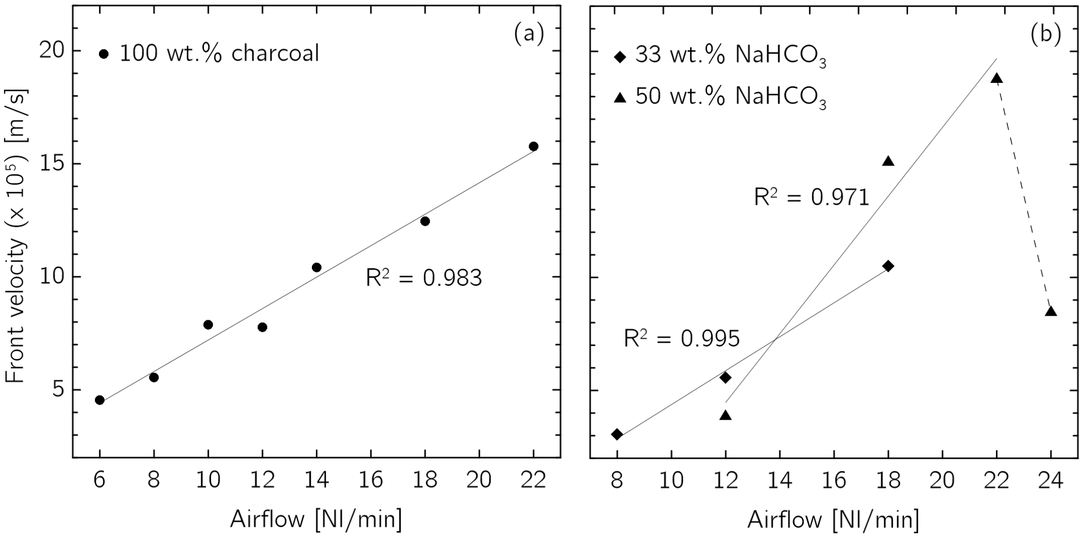

Figure 3.6: Relationship between average front velocity and inlet airflow. (a) Homogeneous bed, from left to right: Exp. 1 to Exp. 7 and (b) heterogeneous bed.

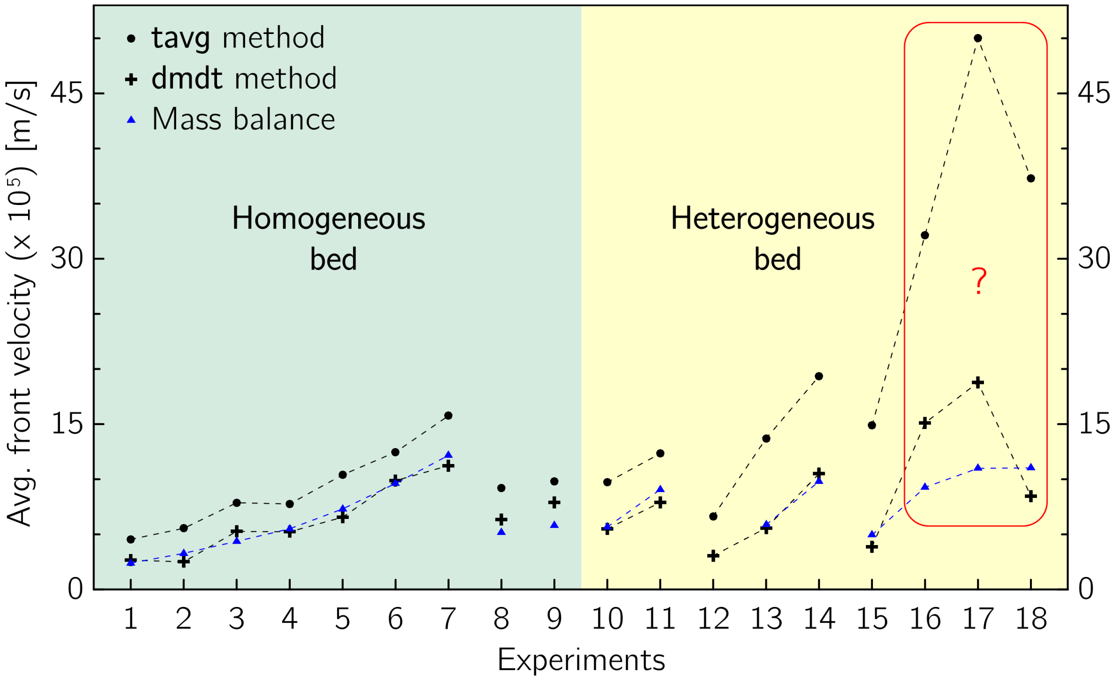

Figure 3.7: The influence of the method used to calculate the front velocity.

By applying the **tavg** method to evaluate the local-average velocity, another interpretation can be carried out to evaluate the gradual, solid fuel consumption along the reactor, Fig.3.8. This analysis is limited by the spatial resolution of 50 mm that was the distance between the thermocouples. It is important to emphasize that the method was successfully applied for homogeneous beds (Exp. 1 - 9), presenting a quite constant profile, whereas it was used with restrictions in heterogeneous beds (Exp 10 -15). For Exp. 16 - 18, **tavg** was unreliable. Martins et al. [21], and Torero and Pello [38], using a different approach, obtained from a constant to increasing velocities profiles in a cylindrical reactor. However, these authors' results must be carefully taken since their estimates were susceptible to the calculation method employed.

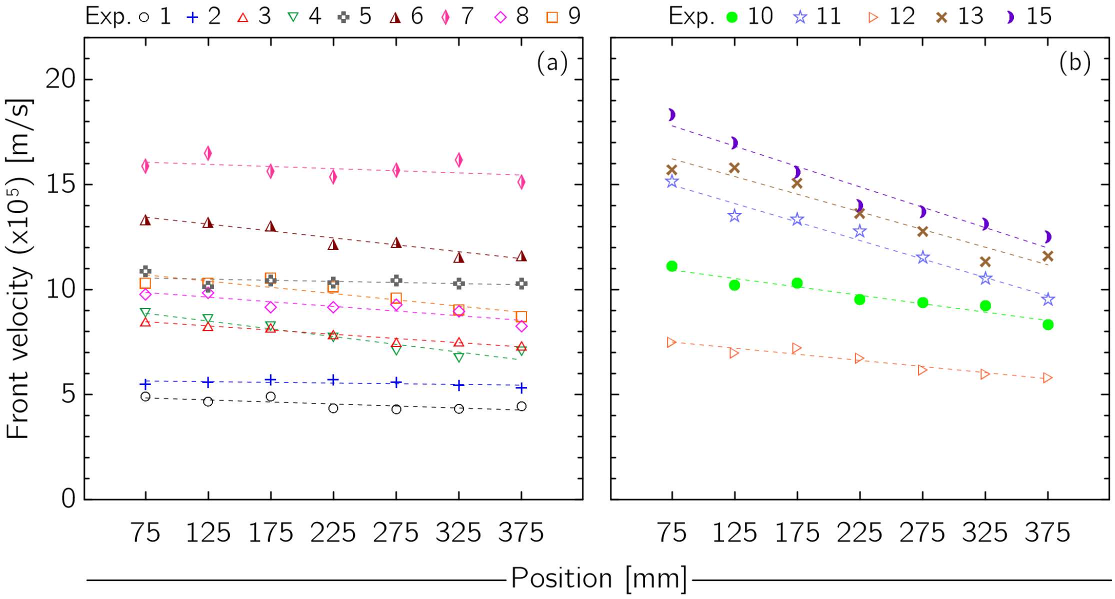

Figure 3.8: Front velocity as a function of position calculated from **tavg** method. (a) Homogeneous bed and (b) heterogeneous bed.

3.4.3 Combustion regimes

Figure 3.9 summarizes the gas analysis, average longitudinal temperature, and equivalent ratio (ER) for the airflow range of 6 to 24 Nl/min. The results of the gas analysis presented in Figure 3.9 c-f was used to set up a mass balance (MB) (Appendix E,[20]) modeling to verify whether the reactions stoichiometry and front velocity have a linear relationship with the product formation rate (CO, CO_2, O_2, and H_2). This strategy was chosen because solely assessing the gas analysis is challenging to interpret, considering that the airflow provokes both chemical reactions and changes in the average bed temperatures. Note that, although NO, NOx and C_xH_y were measured, their quantities were neglected for being below the minimum range of the analyzer.

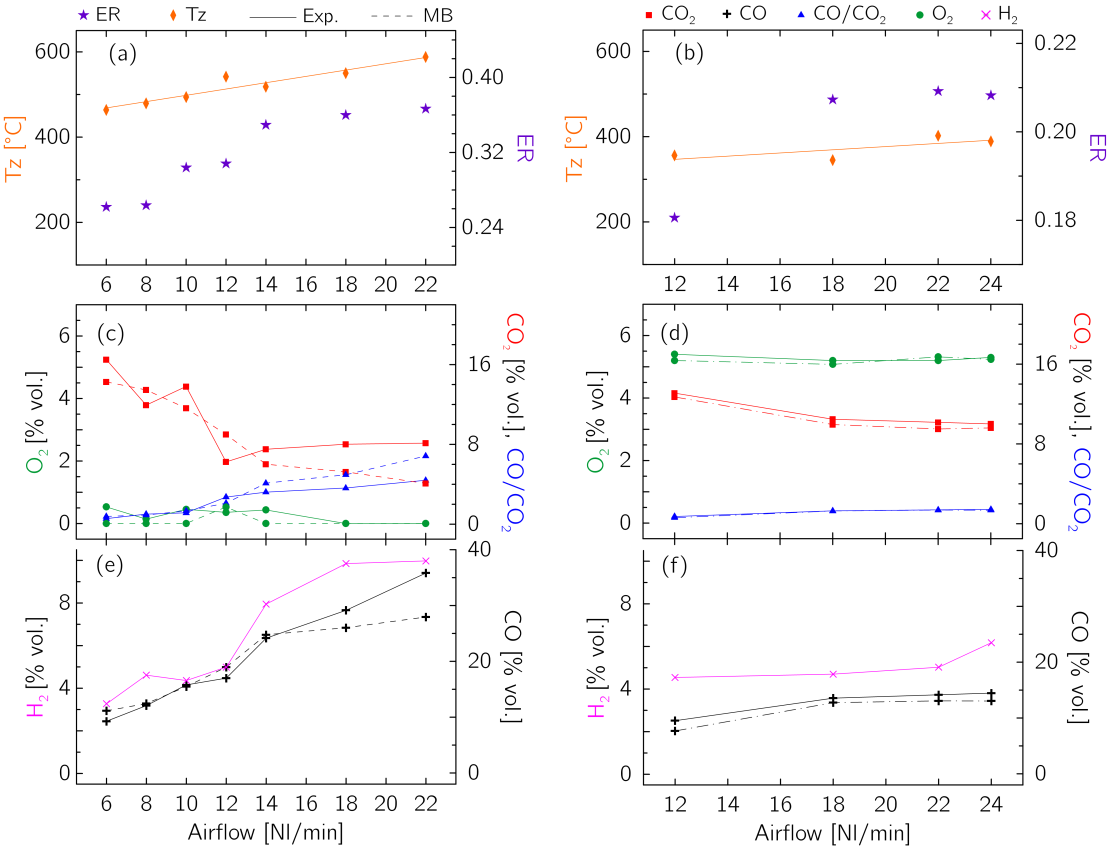

Figure 3.9: Average longitudinal temperature, equivalent ratio, and flue gas composition fixing the bed and varying the inlet airflow. (a), (c), and (e) 100 wt.% Charcoal and (b), (d), and (f) 50 wt.% Charcoal + 50 wt.% $NaHCO_3$.

The main assumptions for the mass balance analysis was one global oxidation reaction $C + (1 - \frac{fr}{2})O_2 \longrightarrow fr\mathrm{CO} + (1 - fr)\mathrm{CO}_2$ (R1), for the homogeneous bed, and a second reaction $\mathrm{NaHCO_3} \longrightarrow 0.5\mathrm{Na_2CO_3} + 0.5\mathrm{CO_2} + 0.5\mathrm{H_2O}$ (R2) for the heterogeneous bed. The model was solved to fr, the fraction of carbon oxidized into CO, running a searching algorithm using as constraints the front velocity in the range determined by **tavg** and **dmdt**, and the gas yields from the flue gas analysis. As a result, the model returned the ER, the total oxygen mass, front velocity correction, and the actual amount of fixed carbon oxidized by the front. The mass balance results are summarized in Table 3.2 and Figure 3.9 c-f.

When the bed type was fixed and the airflow varied, the ER varied from 0.26 to 0.37 for the homogeneous bed. For the heterogeneous bed, it was practically constant around 0.21, indicating that the combustion front propagates under a gasification regime, as

Table 3.2: Combustion front velocity, the fraction of carbon oxidized into CO, and flue gas yields calculated from the mass balance.

Exp.	$v_f(\times 10^5)$ $[m/s]$	fr	O_2 [vol.%]	CO [vol.%]	CO_2 [vol.%]
1	2.4 ± 0.1	0.4	0.1 ± 0.1	11.1 ± 0.9	14.3 ± 1.1
2	3.3 ± 0.4	0.5	0.1 ± 0.1	12.5 ± 0.2	13.5 ± 0.8
3	4.4 ± 0.5	0.6	0.1 ± 0.1	15.5 ± 0.1	11.6 ± 1.1
4	5.5 ± 0.1	0.7	0.5 ± 0.1	19.0 ± 1.0	9.0 ± 1.4
5	7.3 ± 0.4	0.8	0.1 ± 0.1	24.8 ± 0.3	6.0 ± 0.7
6	9.6 ± 0.1	0.8	0.1 ± 0.1	26.0 ± 1.6	5.2 ± 1.4
7	12.2 ± 0.5	0.9	0.1 ± 0.1	28.0 ± 3.9	4.1 ± 2.0
8	5.2 ± 0.6	0.5	0.6 ± 0.1	13.6 ± 0.4	12.2 ± 0.7
9	5.8 ± 1.0	0.5	0.5 ± 0.1	13.7 ± 0.1	12.2 ± 1.2
10	5.7 ± 0.1	0.8	4.8 ± 0.1	17.7 ± 0.1	6.0 ± 0.3
11	9.1 ± 0.6	0.9	4.9 ± 0.1	20.7 ± 0.3	4.1 ± 0.2
13	5.9 ± 0.1	0.7	4.0 ± 0.1	15.3 ± 0.2	8.7 ± 0.3
14	9.8 ± 0.3	0.8	4.9 ± 0.3	19.0 ± 0.9	7.3 ± 0.1
15	4.9 ± 0.5	0.4	5.2 ± 0.1	7.7 ± 0.9	12.7 ± 0.2
16	9.3 ± 2.9	0.6	5.1 ± 0.1	12.8 ± 0.4	9.9 ± 0.3
17	11.0 ± 3.9	0.7	5.3 ± 0.1	13.1 ± 0.5	9.5 ± 0.3
18	11.0 ± 1.3	0.7	5.2 ± 0.1	13.0 ± 0.7	9.6 ± 0.2

evidenced by the high levels of CO and H_2 in the flue gas.

For the homogeneous bed, CO varied from up to 9 vol.% to 35 vol.% and H_2 from 3 to 10 vol.%. Note that O_2 hovered around 1 vol.% to its total consumption, as the airflow increased, and CO_2 halved from 16 vol.% to 8 vol.%. These variations follow the ER changes, as reported by Zainal [29], and the increase in the ER is associated with the average bed temperature increase [39]. The gas composition can be explained if we consider that the global reaction R1 is driven by primary-surface reactions ($1C + O_2 \longrightarrow CO_2$ and $2C + O_2 \longrightarrow 2CO$), and a secondary-surface reaction consuming carbon dioxide ($C + CO_2 \longrightarrow 2CO$). H_2 formation could be related to the steam-methane-reforming reaction. Strategically, the CO/CO_2 ratio was placed in Fig. 3.9b to guide the modeler to implement the classical framework of a one-oxidation reaction for modeling the combustion/smoldering front propagation commonly practiced in numerical works [40].

For the heterogeneous bed, reaction R2 is taken into account. For an airflow range of 12 to 24, this reaction completely modifies the front propagation structure, increasing O_2 levels to an average concentration of 6 vol.% and decreasing the average bed temperature compared to the homogeneous bed, reinforcing the strong endothermicity of reaction R2, as it absorbed energy to release CO_2 (Fig. 3.9). Indeed, the CO_2 concentration in the heterogeneous bed was higher than the homogeneous bed, in absolute terms. Note that the slight temperature increase, which did not follow ER, suggests that the heat released in reaction R1 is competing with the endothermic reaction R2. For the same airflow range, the CO_2 concentration in the homogeneous bed hovered around 7.5 vol.%, while for the heterogeneous bed, it had a low variation around 11 vol.%.

Another approach to interpreting why the ER increase leads to an increase in the average bed temperature, considers the relative velocity of the thermal front and the reaction front, expressed by $\delta = v_f/v_T$. For specific applications, it was useful to exploit such small offsets in v_f and v_T [28]. It already demonstrated that if $v_f < v_T$, the oxidation reaction's heat is mostly convected downstream of the reaction front, leading to an increment of bed average temperature. By examining the relationship between δ and $[1 - (\Delta T_z/\Delta T_{z,teo})]$, Fig. 3.10, for homogeneous and heterogeneous beds, the general trend is an increase of $[1 - (\Delta T_z/\Delta T_{z,teo})]$ due to the reduction in the ratio $\Delta T_z/\Delta T_{z,teo}$ caused to the increase in $\Delta T_{z,teo}$. That means, since the two fronts tend to propagate less separately (the offset between v_f and v_T is being reduced), the average longitudinal temperature has increased. Consequently, an increase in the average longitudinal temperature occurs for the homogeneous bed, driven by the airflow increasing. For the heterogeneous bed, the continuous increase in the ratio $T_z/T_{z,teo}$ confirms the intense endothermic characteristic of reaction R2 pushing down the average temperature even though δ leans towards 1.

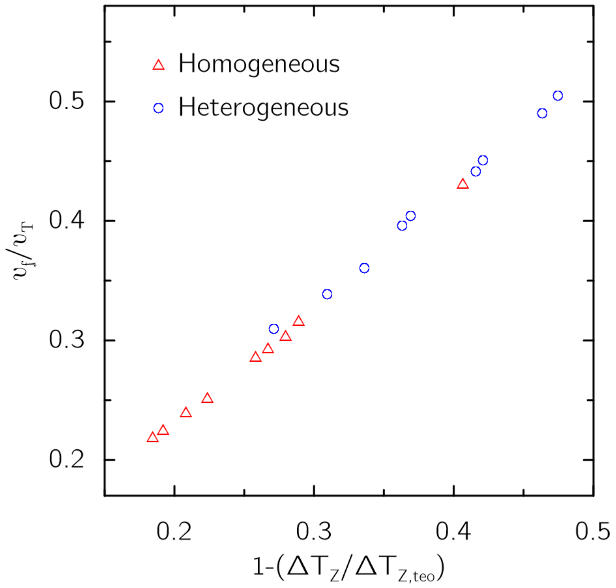

Figure 3.10: Combustion front structure: relationship between $\Delta = v_f/v_T$ and $[1 - (\Delta T_z/T_{z,teo})]$. Each point represents an experiment: Exp. 1 to Exp. 9, from left to right, for the homogeneous bed, and Exp. 10 to Exp. 18, from left to right, for the heterogeneous bed. Note that, $v_T = v_{air}(\rho c_p)_{air}/(\rho c_p)_{bed}$ and $\Delta T_{z,teo} = \Delta T_z[1/(1 - v_f/v_T)]$ adapted from [25, 26, 27, 28].

3.4.4 Energy availability for pyrolysis

We defined the Energy Availability percentage, EA (Joule/Joule of the wall energy flow), the difference of the energy flowing through the pyrolysis chamber wall, and the pyrolysis energy expense to convert a given material, divided by the wall energy flow. The wall energy flow was calculated using the LTP (Chapter 3) to obtain the net wall heat flux (W/m^2). Then the flux was converted into energy by multiplying by wall area and experimental runtime. The pyrolysis energy expense was calculated as the product of the waste enthalpy of pyrolysis (J/g) times the mass of waste material (g) that fits in the pyrolysis chamber volume. The analyzed cases were done for polyethylene waste with an overall enthalpy of pyrolysis of 1100 J/g in average (Appendix D, [41]) and mass varying from 30 g to 60 g inside the pyrolysis chamber, Table 3.1.

Fig. 3.11 shows the EA for two classes of experiments. Ones with high EA (Exp. 4, 5, and 6), in the range 83-91%, and the second class of low EA (Exp. 16 and 17), range 9-15%. A high EA means that the pyrolysis process will consume just around 10 to 20% of the wall energy flow to the pyrolysis chamber wall. Conversely, a low EA indicates that 80 to 90% of the net energy was consumed. Regardless of the EA variation from high to low, it is crucial to highlight that the energy available to perform pyrolysis was more than sufficient. Some outcomes can be pointed out: the use of low-grade fuels (low EA) as heat-driven is feasible; the C-DPyR reactor can be optimized to minimize the mass of fuel per batch and; consequently, the consumption, or maximize the amount of waste converted; high intensive energy waste conversion is conceivable, for instance, wet residues such as biosolids [1, 19].

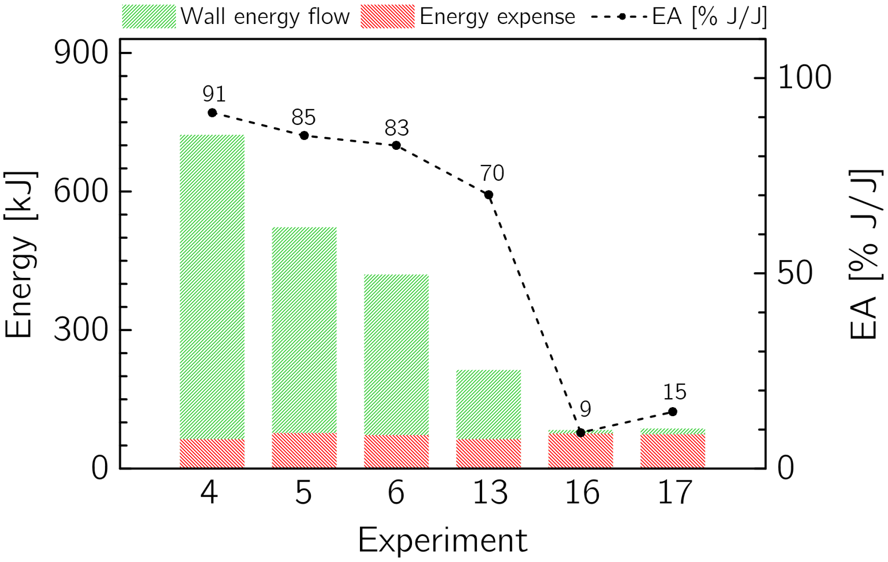

Figure 3.11: Assessment of energy availability for pyrolysis.

3.5 Conclusion

In this paper, the main aspects of smoldering front propagation in an annular section were shown through twenty-nine experiments. It was demonstrated a new reactor design, C-DPyR, for out-of-bed heat recovering to perform waste pyrolysis. We proved that at present, C-DPyR has the best configuration for recovering heat released by the combustion front to drive a secondary process. The classical aspects of smoldering front propagation were presented, and new methodologies were proposed to establish a longitudinal temperature profile (LTP), calculate the front velocity, and determine the structure of the combustion front.

The LTP could be used as the best representative temperature profile to obtain the net heat flux available to pyrolysis. Three methods were used to evaluate the front velocity for batch experiments using homogeneous and heterogeneous beds. The methods diverged as the bed heterogeneity increased, at the point that the tavg method became inaccurate. The concepts of equivalent ratio (ER) and the relative velocity of thermal and reaction fronts were applied to investigate the smoldering propagation regime. The smoldering front propagated under a gasification regime, ER, ranged from 0.26 to 0.37 and around 0.21, respectively, for the homogeneous and heterogeneous. The front structure study indicated that the two fronts tend to propagate less separately, leading to increased average bed temperature (oxidation reaction's heat was mostly convected downstream of the reaction front).

A case study was developed and demonstrated that the C-DPyR could be employed as an alternative device to perform waste pyrolysis. For that, an Energy Availability (EA) assessment based on the pyrolysis chamber wall's heat fluxes, determined from the LTP, and a fictitious case considering pyrolysis heat of 1100 kJ/kg was carried out. It confirmed that the energy to pyrolysis was more than sufficient in all experiments conducted, i.e., for the lowest EA, about 90% of the net energy available was consumed, while for the highest, only 9% of the net energy was consumed.

The global C-DPyR outcomes were:

- The feasibility of using low-grade fuels (low EA) to drive heat.
- The reactor's modifiability since it can be optimized to minimize the mass of fuel per batch and, consequently, the consumption or maximize the amount of waste converted.
- The high energy availability allowing the conversion of energy-intensive materials, such as wet residues.

Bibliography

[1] Flávio Lopes Francisco Bittencourt, Atílio Barbosa Lourenço, Elias Antônio Dalvi, and Márcio Ferreira Martins. Thermodynamic assessment of human feces gasification: an experimental-based approach. *SN Applied Sciences*, 1(9):1–13, sep 2019.

[2] İbrahim Yayalık, Ahmet Koyun, and Mesut Akgün. Gasification of Municipal Solid Wastes in Plasma Arc Medium. *Plasma Chemistry and Plasma Processing*, 40(6):1401–1416, nov 2020.

[3] Wenchao Ma, Chu Chu, Ping Wang, Zhenfei Guo, Bin Liu, and Guanyi Chen. Characterization of tar evolution during dc thermal plasma steam gasification from biomass and plastic mixtures: Parametric optimization via response surface methodology. *Energy Conversion and Management*, 225:113407, 2020.

[4] S.M. Al-Salem, A. Antelava, A. Constantinou, G. Manos, and A. Dutta. A review on thermal and catalytic pyrolysis of plastic solid waste (PSW). *Journal of Environmental Management*, 197:177–198, jul 2017.

[5] Sibel Ügdüler, Kevin M. Van Geem, Ruben Denolf, Martijn Roosen, Nicolas Mys, Kim Ragaert, and Steven De Meester. Towards closed-loop recycling of multilayer and coloured PET plastic waste by alkaline hydrolysis. *Green Chemistry*, 22(16):5376–5394, 2020.

[6] K. Moustakas, P. Parmaxidou, and S. Vakalis. Anaerobic digestion for energy production from agricultural biomass waste in Greece: Capacity assessment for the region of Thessaly. *Energy*, 191:116556, jan 2020.

[7] Nauman Ahmad, Nabeel Ahmad, Ibrahim M. Maafa, Usama Ahmed, Parveen Akhter, Nasir Shehzad, Um e-salma Amjad, and Murid Hussain. Thermal conversion of polystyrene plastic waste to liquid fuel via ethanolysis. *Fuel*, 279:118498, 2020.

[8] Rebecca Solinger, Gavin P Grant, Grant C Scholes, Cody Murray, and Jason I Gerhard. Starx hottpad for smoldering treatment of waste oil sludge: Proof of concept and sensitivity to key design parameters. *Waste Management & Research*, 38(5):554–566, 2020.

[9] Muhammad Saad Qureshi, Anja Oasmaa, Hanna Pihkola, Ivan Deviatkin, Anna Tenhunen, Juha Mannila, Hannu Minkkinen, Maija Pohjakallio, and Jutta Laine-Ylijoki. Pyrolysis of plastic waste: Opportunities and challenges. *Journal of Analytical and Applied Pyrolysis*, page 104804, 2020.

[10] Sonil Nanda and Franco Berruti. Thermochemical conversion of plastic waste to fuels: a review. *Environmental Chemistry Letters*, sep 2020.

[11] J. Loipersböck, G. Weber, R. Rauch, and H. Hofbauer. Developing an adsorption-based gas cleaning system for a dual fluidized bed gasification process. *Biomass Conversion and Biorefinery*, sep 2020.

[12] Zeyang Song, Xinyan Huang, Claudia Kuenzer, Hongqing Zhu, Juncheng Jiang, Xuhai Pan, and Xiaoxing Zhong. Chimney effect induced by smoldering fire in a u-shaped porous channel: A governing mechanism of the persistent underground coal fires. *Process Safety and Environmental Protection*, 136:136 – 147, 2020.

[13] Alexandra L. Duchesne, Joshua K. Brown, David J. Patch, David Major, Kela P. Weber, and Jason I. Gerhard. Remediation of PFAS-Contaminated Soil and Granular Activated Carbon by Smoldering Combustion. *Environmental Science & Technology*, 54(19):12631–12640, oct 2020.

[14] Grant C. Scholes, Jason I. Gerhard, Gavin P. Grant, David W. Major, John E. Vidumsky, Christine Switzer, and Jose L. Torero. Smoldering Remediation of Coal-Tar-Contaminated Soil: Pilot Field Tests of STAR. *Environmental Science & Technology*, 49(24):14334–14342, dec 2015.

[15] G. Gianfelice, M. Della Zassa, A. Biasin, and P. Canu. Onset and propagation of smouldering in pine bark controlled by addition of inert solids. *Renewable Energy*, 132:596 – 614, 2019.

[16] Yuqi Hu, Eirik Christensen, Francesco Restuccia, and Guillermo Rein. Transient gas and particle emissions from smouldering combustion of peat. *Proceedings of the Combustion Institute*, 37(3):4035 – 4042, 2019.

[17] Ivo Fabris, Daniel Cormier, Jason I. Gerhard, Tomek Bartczak, Mark Kortschot, Jose L. Torero, and Yu-Ling Cheng. Continuous, self-sustaining smouldering destruction of simulated faeces. *Fuel*, 190:58 – 66, 2017.

[18] L. Yermán, H. Wall, and José L. Torero. Experimental investigation on the destruction rates of organic waste with high moisture content by means of self-sustained smoldering combustion. *Proceedings of the Combustion Institute*, 36(3):4419 – 4426, 2017.

[19] Tarek L Rashwan, Jason I Gerhard, and Gavin P Grant. Application of self-sustaining smouldering combustion for the destruction of wastewater biosolids. *Waste management*, 50:201–212, 2016.

[20] M.F. Martins, S. Salvador, J.-F. Thovert, and G. Debenest. Co-current combustion of oil shale – part 1: Characterization of the solid and gaseous products. *Fuel*, 89(1):144 – 151, 2010.

[21] M.F. Martins, S. Salvador, J.-F. Thovert, and G. Debenest. Co-current combustion of oil shale – part 2: Structure of the combustion front. *Fuel*, 89(1):133 – 143, 2010.

[22] Marco A.B. Zanoni, José L. Torero, and Jason I. Gerhard. Delineating and explaining the limits of self-sustained smouldering combustion. *Combustion and Flame*, 201:78 – 92, 2019.

[23] José L. Torero, Jason I. Gerhard, Marcio F. Martins, Marco A.B. Zanoni, Tarek L. Rashwan, and Joshua K. Brown. Processes defining smouldering combustion: Integrated review and synthesis. *Progress in Energy and Combustion Science*, 81:100869, 2020.

[24] Hafiz M.F. Amin, Yuqi Hu, and Guillermo Rein. Spatially resolved horizontal spread in smouldering peat combining infrared and visual diagnostics. *Combustion and Flame*, 220:328 – 336, 2020.

[25] A.P. Aldushin, I.E. Rumanov, and B.J. Matkowsky. Maximal energy accumulation in a superadiabatic filtration combustion wave. *Combustion and Flame*, 118(1):76 – 90, 1999.

[26] A.A.M Oliveira and M Kaviany. Nonequilibrium in the transport of heat and reactants in combustion in porous media. *Progress in Energy and Combustion Science*, 27(5):523 – 545, 2001.

[27] G Debenest, V V Mourzenko, and J F. Thovert. Smouldering in fixed beds of oil shale grains: governing parameters and global regimes. *Combustion Theory and Modelling*, 9(2):301–321, 2005.

[28] S. Zhdanok, Lawrence A. Kennedy, and G. Koester. Superadiabatic combustion of methane air mixtures under filtration in a packed bed. *Combustion and Flame*, 100(1):221 – 231, 1995.

[29] Z.A Zainal, Ali Rifau, G.A Quadir, and K.N Seetharamu. Experimental investigation of a downdraft biomass gasifier. *Biomass and Bioenergy*, 23(4):283–289, oct 2002.

[30] Filipe Arthur Firmino Monhol and Marcio Ferreira Martins. Ignition by Thermal Radiation of Polyethylene and Human Feces Combustible Wastes: Time and Temperature to Ignition. *Advanced Materials Research*, 911:373–377, mar 2014.

[31] FAF Monhol and MF Martins. Cocurrent combustion of human feces and polyethylene waste. *Waste and Biomass Valorization*, 6(3):425–432, 2015.

[32] ASTM D3172-13. Standard practice for proximate analysis of coal and coke. Technical report, ASTM International, West Conshohocken, PA, 2013.

[33] ASTM D3173 / D3173M-17a. Standard test method for moisture in the analysis sample of coal and coke. Technical report, ASTM International, West Conshohocken, PA, 2017.

[34] ASTM D3174-12(2018). Standard test method for ash in the analysis sample of coal and coke from coal. Technical report, ASTM International, West Conshohocken, PA, 2018.

[35] ASTM D3175-20. Standard test method for ash in the analysis sample of coal and coke from coal. Technical report, ASTM International, West Conshohocken, PA, 2020.

[36] P. Umponpanarat and S. Wansom. Thermal conductivity and strength of foamed gypsum formulated using aluminum sulfate and sodium bicarbonate as gas-producing additives. *Materials and Structures*, 49(4):1115–1126, apr 2016.

[37] Donghoon Shin and Sangmin Choi. The combustion of simulated waste particles in a fixed bed. *Combustion and Flame*, 121(1):167 – 180, 2000.

[38] J.L. Torero and A.C. Fernandez-Pello. Forward smolder of polyurethane foam in a forced air flow. *Combustion and Flame*, 106(1):89 – 109, 1996.

[39] Prabir Basu. Chapter 6 - design of biomass gasifiers. In Prabir Basu, editor, *Biomass Gasification and Pyrolysis*, pages 167 – 228. Academic Press, Boston, 2010.

[40] Victor Pozzobon, Germain Baud, Sylvain Salvador, and Gerald Debenest. Darcy scale modeling of smoldering: Impact of heat loss. *Combustion Science and Technology*, 189(2):340–365, 2017.

[41] Sahar Khedri and Siamak Elyasi. Determination of the heat of pyrolysis of hdpe via isothermal differential scanning calorimetry. *Journal of Thermal Analysis and Calorimetry*, 131(2):1509–1515, 2018.

Chapter 4

The influence of the recycling stress history on LDPE waste pyrolysis

---

Contents

Summary

This chapter deals with the characterization of low-density polyethylene (LDPE) waste. The main objective was to understand if the physical stress undergone by two categories of polyethylene waste within the mechanical recycling cycles has an influence on the kinetics and pyrolysis pathway. The quantitative aspects such as enthalpy of conversion and hydrocarbon arrangement were also investigated. Virgin polyethylene was used as a reference for establishing a comparison with the wastes in terms of thermochemical behavior and composition.

To understand the basic thermochemical behaviors of the samples, such as mass loss and heat flux absorbed or released, thermogravimetric analysis (TGA) and differential scanning calorimetry (DSC) were performed. The kinetic triplet was also obtained processing the TGA data and by using differential and integral isoconversional methods. To determine the sample composition and hydrocarbon arrangements, ultimate, proximate, and X-ray diffraction (XRD) analyses were carried out. Taking advantage of these analyses and combining them, a series-parallel pyrolysis pathway was formulated.

The thermal degradation study identified that the samples of virgin and recycled PE when subjected to pyrolysis, at different heating rates, lose almost all the mass in a single step. The onset and offset temperatures were around 350 °C and 500 °C, respectively. DSC curves under pyrolysis conditions showed two endothermic peaks. The first one assigned to the melting point (no mass loss) and the second peak attributed to the degradation reactions, which are associated with the complete mass loss on TGA. The waste of recycled polyethylene presented lower enthalpy of pyrolysis, at about 205 J/g against 299 J/g for a virgin PE. And also, when combined with XRD results, that identified the main chemical compounds of the crystalline phase, the DSC evidenced a multi-step reaction behavior of the pyrolysis. It was confirmed by the kinetic study that detected an important variation of activation energies as a function of the fraction reacted for the waste samples. Based on these results, a multi-step pathway including pre-heating, melting, bond breaking, evaporation, and pyrolysis reaction was delineated to describe the LDPE thermal decomposition.

The main conclusion of this chapter is that the recycling stress history promotes modifications in the structure of the samples, suggesting that different categories of LDPE wastes must be considered when dealing with either kinetics or modeling of the product recovery process.

Candidate contribution: Conceptualization, methodology, software, validation, formal analysis, resources, data curation, writing - original draft, visualization.

4.1 Introduction

It is elementary to recognize the benefits and, of course, the negative impacts of the use of plastic materials on modern societies. The global production of plastic materials has grown drastically. According to a European report [1], world plastic production has increased by around 40% in the last 10 years and polyethylene (PE) is the major plastic component present in municipal solid waste streams. In general, polyethylene accounts for 43% of the total plastic fraction present in municipal solid waste [2]. This is the reason for the rising processes of converting polyethylene waste into useful products [3, 4, 5, 6, 7, 8, 9]. Since these processes are supposed to convert waste plastics, some characteristics such as density and additives are well known to affect i.e. the rate of conversion and yields of products recovered [10, 11, 12]. Another characteristic might play an important role in the conversion processes: the physical stress history experienced by the waste in mechanical recycling. This process typically involves mechanical (separation, grinding, washing, agglutination) and thermal stress (drying, extrusion, and quenching) [3, 13, 14].

The polyethylene materials entering the mechanical recycling process can be described by the stream in Fig. 4.1. The virgin PE (VPE) pellets are used as raw material where noble plastic products are manufactured. Inside the industry is generated plastic residue that is well suited for the mechanical recycling process. The main part of plastic wastes is mostly generated by the final consumer. Depending on the infrastructure of each country, the plastic wastes can follow different paths (solid waste management cycle, landfills or waste pickers). The recycled material returns to manufacturing as feedstock producing less noble plastic products such as garbage bags and various packaging. Therefore, two categories of wastes are commonly generated: waste of virgin polyethylene (WVPE) and waste of recycled polyethylene (WRPE). In that way, the mechanical recycling process continues until the plastic waste previously recycled cannot be reused anymore.

Isoconversional methods are commonly used to evaluate the decomposition kinetics of polyethylene. The best-known methods recommended by the International Confederation for Thermal Analysis Calorimetry (ICTAC) to capture the kinetic triplet (the activation energy, E, the pre-exponential factor, A, and the reaction model, $f(\alpha)$) and widely used are Friedman (FR) [15], Ozawa Flynn and Wall (OFW) [16, 17, 18, 19], Kissinger Akahira and Sunnose (KAS) [20, 21], and Starink (ST) [22].

The previous studies successfully explained polyethylene kinetics through the evaluation of variable E and distributed A with the extent of the progress of the reaction [23, 24, 25, 26, 27, 28]. These authors were concerned about verifying the best statistical fit for the kinetic parameters. However, until now, there is no study concerned about how different categories of LDPE wastes can impact both kinetics values and pathways.

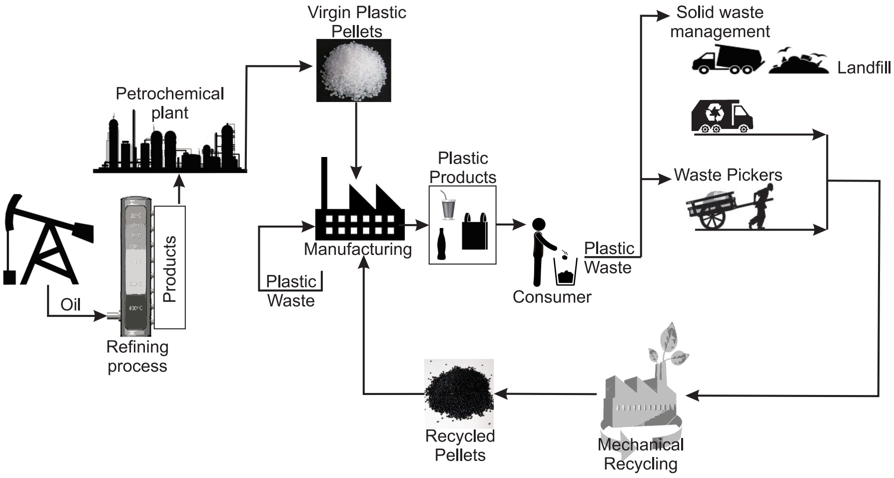

Figure 4.1: Lifecycle of PE materials.

The literature-oriented mainly consider that LDPE pyrolysis can be modeled as a single-step reaction, and it is true in some cases [29, 30], but some studies mention complex reaction mechanisms [26, 31, 32]. According to [33], a significant variation of the kinetics values indicates that a process is kinetically complex, therefore, the consideration of a single-step mechanism cannot be applied. The major problem might be the fact that some studies modeled wastes using virgin polyethylene as a sample whereas, in others, there is no clear concern about the origin of these wastes.

The aim of the present study is to understand if the physical stress undergone by two categories of low-density polyethylene waste (WVPE, WRPE) within the mechanical recycling cycles has an influence on the kinetics and pyrolysis pathway. The quantitative aspects such as enthalpy of conversion and hydrocarbon arrangement are also investigated. In the entire study process, the low-density VPE is used as a reference for establishing a comparison with PE wastes in terms of thermochemical behavior.

The differences between virgin/waste and waste/waste samples are characterized by the x-ray diffraction technique and complemented via differential scanning calorimetry. Both techniques have been widely employed to characterize qualitatively and quantitatively the crystalline structures and enthalpy of melting of polyethylene [34, 35]. For these reasons, they are applied in the present work also for pyrolysis.

4.2 Material and methods

Independently of the thermal conversion process employed during the treatment of any type of waste, it is important prior knowledge of the ultimate and proximate composition, as well as some other basic thermochemical behavior such as mass loss and heat flux absorbed or released. Thereby, a series of experiments were performed on samples of PE to address the problem in a critical and effective way.

4.2.1 Polyethylene samples

The plastic materials used were samples of LDPE, the virgin from the petrochemical industry and the recycled from municipal solid waste provided by LukPlast Ind. (ES-Brazil). VPE has regular geometry (button type) with an average diameter of around 4 mm and does not have any pigmentation (transparent color). The recycled samples are a mix of irregular geometries, 2 mm average particle size, and are organized into two types: WVPE, with a type of pigmentation resulting from the first and unique mechanical recycling process of waste VPE, and WRPE which underwent from two to undetermined numbers of mechanical recycling cycles, and carries all types of pigmentation (see Fig. 4.2).

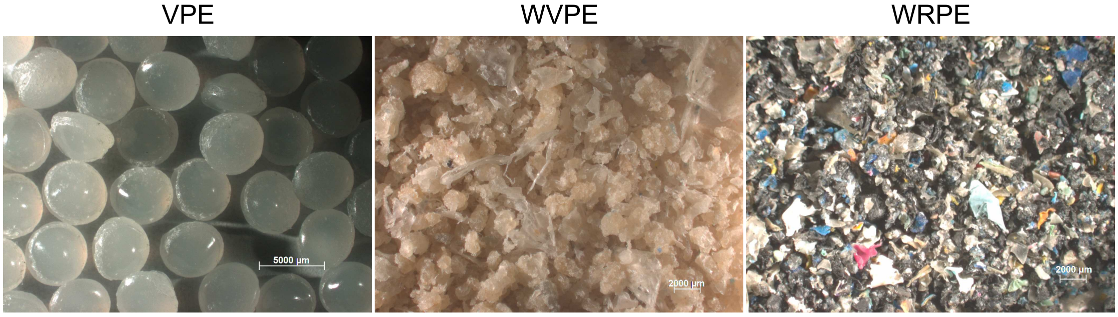

Figure 4.2: Polyethylene virgin and recycled samples.

4.2.2 Methods

The thermal degradation study was carried out by using thermogravimetric analysis (TGA) then the data were processed to obtain the kinetic triplet. X-ray diffraction (XRD), ultimate and proximate analyses were applied to investigate if LDPE samples could have a certain degree of differentiation either on composition and hydrocarbon arrangement. The XRD results combined with the analysis of differential scanning calorimetry (DSC) under an inert atmosphere and complementary under an oxidative one were used to formulate the pyrolysis pathway. From DSC curve integration, the average enthalpies of melting and pyrolysis were established. The configurations of each method are presented in Table 4.1.

Table 4.1: Experimentation details of PE samples.

Name of experiment	Make	Operating conditions	Reference
TGA	STA 449F3 - NETZSCH	Sample mass: 10-15 mg	ISO 11358
		Crucible: Al_2O_3	DIN 51006
		Carrier gas: N_2, Air, 60 ml/min	
		Temperature range: 20-670 °C	
		Heating rates, β: 5, 10, 15, and 20 °C/min	
XRD	ULTIMA IV - RIGAKU	CuK alpha radiation: average length $\lambda = 0.15419$	Souza et al. [36]
		Theta/2-theta Bragg-Brentano geometry	
		2-theta data range: 5.00° to 125.00°	
		Step size: 0.02°	
		CuK alpha doublet: wavelengths of 0.154056 (65%) and 0.154439 (35%) nm.	
		Radiation detector: LiF monochromator	
Ultimate analysis	EA 1110 - CE	Default settings	*ASTM D5373-16
Proximate analysis	Muffle furnace	Moisture and ash: Weight loss	ASTM D6980-17 / D5630-13
		Volatile matter: **by difference	-
DSC	SDT Q600 - TA	Sample mass: 20 mg	ASTM E2160-04
		Crucible: Al_2O_3	
		Carrier gas: N_2, Air, 50 ml/min	
		Temperature range: 20-570 °C	
		Heating rates, β: 20 °C/min	

* there is no specific standard for PE / ** based on the assumption that all the carbon and hydrogen, except for the moisture and ash contents, form the volatile matter matrix.

4.2.3 Data processing

The rate of non-isothermal solid decomposition, $d\alpha/dt$, registered by TGA can be expressed in terms of the rate constant, $k(T)$, and the reaction model, $f(\alpha)$, Eq. 4.1. The rate constant represents the dependence of the process rate on temperature and is parametrized through the Arrhenius equation, Eq. 4.2. The reaction model represents the dependence on the fraction reacted, α, Eq. 5.3, which is determined experimentally as a fraction of the total mass loss during the process.

$$\frac{d\alpha}{dt} = k(T)f(\alpha) \tag{4.1}$$

$$k(T) = Aexp\left(-\frac{E}{\Re T}\right) \tag{4.2}$$

$$\alpha = \frac{m_0 - m_i}{m_0 - m_f} \tag{4.3}$$

Where A and E are kinetic parameters, the pre-exponential factor, and the apparent activation energy, respectively, $\Re$ is the universal gas constant, T is the absolute temperature, and m_i, m_0, and m_f represent the instantaneous, initial, and final masses of the sample, respectively.

Combining Eq. 4.1 and Eq. 4.2 leads to Eq. 4.4, that is limited to describe the rate of decomposition of a single-step process [33, 37]. For constant heating rate non-isothermal conditions ($\beta = dT/dt$), Eq. 4.4 can be written in the form of Eq. 4.5.

$$\frac{d\alpha}{dt} = Aexp\left(-\frac{E}{\Re T}\right)f(\alpha) \tag{4.4}$$

$$\beta\frac{d\alpha}{dT} = Aexp\left(-\frac{E}{\Re T}\right)f(\alpha) \tag{4.5}$$

The degradation characteristics of VPE, WVPE, and WRPE were quantified through several parameters. Onset and offset temperatures, T_{on} and T_{off}, related to the start and end of the sample thermal conversion, were obtained from the TGA, its derivatives, DTG, and second-time derivatives, D_2TG, curves as the scheme demonstrated in Fig. 4.3. The onset temperature was determined by extrapolating the slope of the DTG curve in correspondence with the first peak in second-time derivatives curves and up to the zero levels of the DTG axis. The same procedure was used to determine the offset temperature, in this case, picking up the last peak in second-time derivatives curves [28, 38, 39, 40]. The peak temperatures, T_{peak}, related to the maximum rate of sample degradation, were obtained from DTG curves and correspond to the temperature of their peaks. The total mass losses, Δ_m, were obtained from the difference between the initial mass and the mass after pyrolysis.

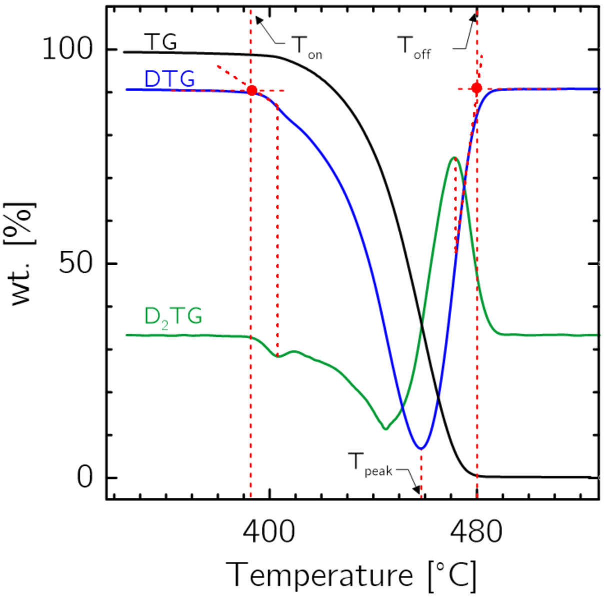

Figure 4.3: Method used to determine the onset, offset, and peak temperatures.

From the DSC data, the enthalpies of reactions were calculated by integrating the areas of the curves (heat flux versus time interval) using scientific graphing and data analysis software [41]. For that, an isothermal baseline was constructed based on the second derivative of the DSC signal; ergo, the onset and end temperatures of melting and pyrolysis were determined [38].

The diffraction patterns were analyzed using Fityk software, version 0.9.8.57 [41]. Phase identification was performed through the Hanawalt method [42, 43, 44] using the Crystallography Open Database (COD) [45] and PDF-2 database [46]. The quantification of the phases was performed with Rietveld refinement using the FullProf program [47].

4.2.4 Isoconversional methods

Isoconversional methods are an effective tool that can be used to solve Eq. 4.4 or Eq. 4.5 and determine the kinetic parameters as a function of the fraction reacted. These methods are based on the assumption that the rate of decomposition, at a constant value of α, is only a function of the temperature [37]. Taking into account the methodology adopted, the isoconversional methods can be separated into two main categories: differential and integral.

A widely used differential isoconversional method, based on the logarithm of Eq. 4.4 or Eq. 4.5, is the Friedman method [15], Eq. 5.4. By plotting $\ln(\beta d\alpha/dT)$ against $1/T$, the kinetic parameters can be calculated from the slope at each given α. It is important to point out that, although the differential methods do not use any approximation, they are very sensitive to experimental noises.

$$\ln\left(\frac{d\alpha}{dt}\right) = \ln\left(\beta\frac{d\alpha}{dT}\right) = \ln\left[Af(\alpha)\right] - \frac{E}{\Re T} \tag{4.6}$$

On the other hand, the variables in Eq. 4.5 can be separated and on integration gives Eq. 5.5

$$g(\alpha) \equiv \int_0^{\alpha} \frac{d\alpha}{f(\alpha)} = \frac{A}{\beta}\int_0^{T} exp\left(-\frac{E}{\Re T}\right) dT \tag{4.7}$$

where $g(\alpha)$ is the integral form of the reaction model. The integral in Eq. 5.5 does not have an analytical solution and several approximations can be found in the literature [33, 37]. Generally, the approximate solutions are represented by the general equation:

$$\ln\left(\frac{\beta}{T^B}\right) = const - C\left(\frac{E}{\Re T}\right) \tag{4.8}$$

where B and C are the parameters determined by the type of temperature integral approximation. Worth noting that the approximation used is directly related to the accuracy of the integral method.

Three different approaches, integral isoconversional methods, were considered in the present work: Starink, Eq. 5.6 [22]; Kissinger - Akahira - Sunose, Eq. 4.10 [20, 21]; and Ozawa - Flynn - Wall, Eq. 4.11 [16, 17, 18, 19].

$$\ln\left(\frac{\beta}{T^{1.92}}\right) = const - 1.0008\left(\frac{E}{\Re T}\right) \tag{4.9}$$

$$\ln\left(\frac{\beta}{T^2}\right) = \ln\left(\frac{A\Re}{Eg(\alpha)}\right) - \frac{E}{\Re T} \tag{4.10}$$

$$\ln(\beta) = \ln\left(\frac{AE}{\Re g(\alpha)}\right) - 5.331 - 1.052\frac{E}{\Re T} \tag{4.11}$$

The left-hand side of each method was plotted against $1/T$ for each experimental TGA data and the kinetic parameters were calculated from the slope of the straight lines fitted at each common value of α.

4.2.5 Reaction model

The dependence of the decomposition process on the fraction reacted can be expressed by using a wide variety of reaction models, each of these with a characteristic reaction profile [37]. The Criado method [28, 33, 48, 49] was used to determine the kinetic model able to describe the pyrolysis of each material investigated. The method is based on an approximate solution of the integral in Eq. 5.5 and leads to the construction of a generalized master plot. The relationship between the experimental data recorded under non-isothermal conditions, the generalized reaction rate, and the differential and integral forms of the theoretical solid-state reaction models, Table 4.2 [33, 37, 50], can be described by Eq. 5.7.

$$\left(\frac{T}{T_{0.5}}\right)^2 \frac{(d\alpha/dt)}{(d\alpha/dt)_{0.5}} = \frac{f(\alpha)\,g(\alpha)}{f(0.5)\,g(0.5)} \tag{4.12}$$

The equation above is normalized taking $\alpha = 0.5$ as a reference, being $T_{0.5}$ and $(d\alpha/dt)_{0.5}$, at the left hand side, and $f(0.5)$ and $g(0.5)$, at the right hand side, the temperature, the reaction rate and the conversion functions corresponding to 50% conversion.

The most suitable kinetic model is determined by the best match between the plot of the generalized reaction rate vs. the fraction reacted and the plots of the theoretical models. The Root Mean Square Error (RMSE), Eq. 4.13, was used to measure how much error there is between the curves, assisting identify the best correspondence.

$$RMSE = \sqrt{\frac{\sum_{i=1}^{n}\left[(d\alpha/dt)_{exp} - (d\alpha/dt)_{model}\right]^2}{n}} \tag{4.13}$$

Table 4.2: Algebraic expressions of the most widely used theoretical solid-state reaction models.

Model	Code	$f(\alpha)$	$g(\alpha)$
Power-law	P_n^a	$n\alpha^{(n-1/n)}$	$\alpha^{(1/n)}$
Zero-order	$F0$	1	α
First-order	$F1$	$1-\alpha$	$-ln(1-\alpha)$
Second-order	$F2$	$(1-\alpha)^2$	$[1/(1-\alpha)]-1$
Third-order	$F3$	$(1-\alpha)^3$	$[1/(1-\alpha)^2]-1$
Avrami-Erofeev	A_n^b	$n(1-\alpha)[-ln(1-\alpha)]^{1-1/n}$	$[-ln(1-\alpha)]^{1/n}$
Contracting geometry	R_n^c	$n(1-\alpha)^{1-1/n}$	$1-(1-\alpha)^{1/n}$
One-dimensional diffusion	$D1$	$(1/2)\alpha^{-1}$	α^2
Two-dimensional diffusion	$D2$	$[-ln(1-\alpha)]^{-1}$	$(1-\alpha)ln(1-\alpha)+\alpha$
Three-dimensional diffusion	$D3$	$(3/2)(1-\alpha)^{2/3}[1-(1-\alpha)^{1/3}]^{-1}$	$[1-(1-\alpha)^{1/3}]^2$
Ginstling-Brounshtein	$D4$	$(3/2)[(1-\alpha)^{-1/3}-1]^{-1}$	$1-(2\alpha/3)-(1-\alpha)^{2/3}$
Prout-Tompkins	$B1$	$\alpha(1-\alpha)$	$ln[\alpha/(1-\alpha)]$
Exponential-law	$E1$	α	$ln(\alpha)$

$^a n = 2/3, 2, 3, 4$ / $^b n = 2, 3, 4$ / $^c n = 2, 3$

4.3 Results and discussion

4.3.1 Thermogravimetric analysis (TGA)

TGA and DTG results under inert atmosphere are summarized in Fig. 4.4. In this figure, each column contains the respective decomposition profile of VPE, WVPE, and WRPE at four different heating rates.

The heating rates were strategically chosen to cover the influence of a wide range of temperatures on PE degradation. The samples of virgin and recycled PE when subjected to pyrolysis, at all heating rates, lose almost all the mass in a single step. The heating rate increase resulted in a lateral shift of the curves along the abscissa without changing its shape. The initial mass, onset temperature, offset temperature, peak temperature at maximum degradation rate, and the total mass losses after pyrolysis are presented in Table 4.3.

4.3.2 X-ray diffraction analysis

Fig. 4.5 shows the X-ray powder diffraction patterns for all samples. The compounds quantification was performed based on the volumetric proposition of the structures found in a sample volume of 1 mm x 10 mm x 0.005 mm. The mass proportion of the phases depends on the determination of the true density (crystallographic) of the phases present. The uncertainty volume value proposed for each phase found, as considered the volume

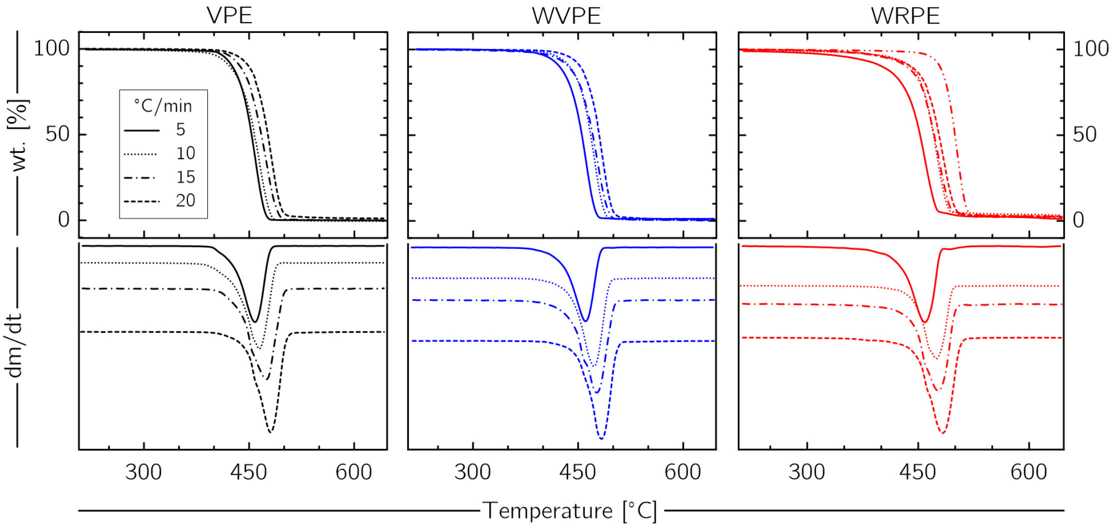

Figure 4.4: Polyethylene thermogravimetric analysis under inert atmosphere and its derivatives.

Table 4.3: Polyethylene thermogravimetric analysis: initial mass, onset, offset, and peak temperatures and total mass losses.

Sample	β [°C/min]	m_i [mg]	T_{on} [°C]	T_{off} [°C]	T_{peak} [°C]	Δ_m [wt.%]
VPE	5	13.3	392	480	458	99.9
	10	12.3	387	488	465	99.9
	15	13.2	396	500	475	99.9
	20	12.7	405	504	481	99.9
WVPE	5	14.6	376	484	461	98.8
	10	10.9	384	496	473	99.7
	15	14.0	388	502	477	99.9
	20	14.1	394	506	483	99.8
WRPE	5	13.4	357	480	459	98.9
	10	13.1	367	497	475	96.8
	15	13.4	367	502	477	98.0
	20	12.9	367	507	483	97.7

measured by XRD, is limited to 2% taken into account the copper radiation (CuKa, 0.15419nm), the Bragg-Brentano geometry, 0.5° divergent slit, 0.5° scattering slit and LiF monochromator.

It was possible to identify and quantify the chemical compounds of all samples without considering the amorphous phase. The average crystallinity was 48%, 51%, and 54% for VPE, WVPE, and WRPE respectively. The analysis indicated that the main chemical compounds of crystalline phase of VPE were pentatriacontane ($C_{35}H_{72}$) and n-paraffin $(CH_2)_x$, while the main compounds of the recycled samples were n-tetracontane ($C_{40}H_{82}$) and n-nonacosane ($C_{29}H_{60}$) (Table 4.4). The data collection details can be shown as supplementary material, Appendix F.

As one can observe in Table 4.4, the results suggest that the recycling stress history promotes the increase of long carbon chains in WVPE and WRPE compared to VPE. The cause might be the combination of thermal and extrusion stress experienced by the PE in the cycles of recycling.

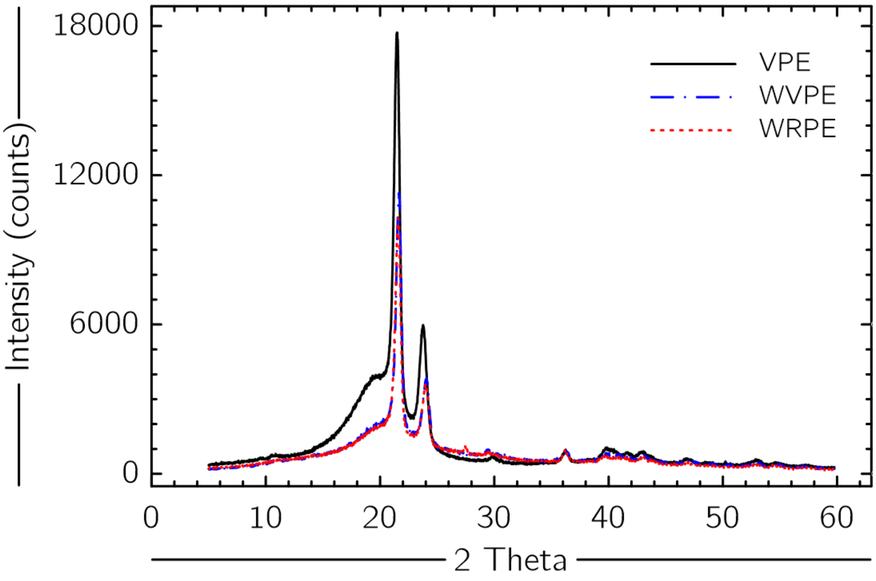

Figure 4.5: X-ray powder diffraction pattern.

4.3.3 Ultimate and proximate analyses

The results indicate mainly the presence of carbon and hydrogen for all samples. Small percentages of other elements, apart from CHNS, are present in the recycled samples: 0.3 and 2.0 wt.% in WVPE and WRPE, respectively. The samples were found to be non-hygroscopic materials and only a small amount of moisture, around 0.2 wt.%, was

Table 4.4: All samples content available by X-ray diffraction pattern analysis, values in vol.%.

Compound name	VPE	WVPE	WRPE
n-Paraffin $(CH_2)_x$	10.1	-	-
Paraffin wax (C - H)	4.9	-	-
n-Heptadecane ($C_{17}H_{36}$)	-	2.3	-
n-Tricosane ($C_{23}H_{48}$)	-	-	4.8
n-Nonacosane ($C_{29}H_{60}$)	4.2	15.8	16.4
Pentatriacontane ($C_{35}H_{72}$)	80.8	-	-
n-Tetracontane ($C_{40}H_{82}$)	-	81.9	78.8

Uncertainty volume value is limited to 2%.

found in WVPE and WRPE. When compared to VPE, the WRPE samples presented an approximately threefold relative increase in ash content, from 0.3 to 1.0 wt.%. The results of ultimate and proximate analyses are listed in Table 4.5.

Table 4.5: Polyethylene samples ultimate and proximate analyses, values in wt.%.

Component	VPE	WVPE	WRPE
C	85.7 ± 0.8	85.4 ± 0.1	84.3 ± 0.1
H	14.3 ± 0.2	14.3 ± 0.3	13.7 ± 0.3
N	0.0	0.0	0.0
S	0.0	0.0	0.0
Other elements*	0.0	0.3± 0.3	2.0 ± 0.3
Moisture	0.0	0.2	0.2
Ash	0.3	0.4	1.0
Volatile matter*	99.7	99.4	98.8

*Obtained by difference / Proximate analysis (mean ± 0.1).

4.3.4 Differential Scanning Calorimetry (DSC)

Analyzing the DSC curves under pyrolysis conditions, Fig. 4.6, two endothermic peaks are observed for all samples. The first one is assigned to the melting point and confirmed by checking TGA under nitrogen where no mass loss is identified in the temperature range of the first endothermic peak. The second peak is attributed to PE degradation reactions, which are associated with the complete mass loss on TGA.

The integration of the DSC curves can be used to estimate the magnitude order of the enthalpies of melting and pyrolysis. The values of enthalpies of melting were 75, 74, and 65 J/g for VPE, WVPE, and WRPE respectively. The values of 299, 332, and 205 J/g for enthalpies of pyrolysis of VPE, WVPE, and WRPE were respectively obtained.

Since the majority of the work does not categorize their type of residues, the values of enthalpies reported in [35, 51] for melting at about 90 J/g, and in [52] for pyrolysis at about 258 J/g provide a rough indication of the expected order of magnitude. Looking at the effect of the physical stress on these categories of polyethylene waste, the results suggest that WRPE suffered some modification in its structure leading to weakening of the material, see Section 4.3.2.

To complement the result analysis of the inert atmosphere, DSC under air was carried out. Through the oxidation of the PE samples, it can be observed one endothermic peak - related to the one found under an inert atmosphere -, and various exothermic peaks indicating that competing reactions are taking place. These reactions with some overlapping degree can be attributed to the key compounds forming the samples, see Table 4.4. Therefore, by simplifying the analysis, one can attribute mainly four oxidation reactions for VPE (r_1, r_3, r_4, and r_5) and three for WVPE and WRPE (r_1, r_3, and r_4) according to the number of the compounds of each sample. The reaction r_2 is attributed to endothermic phenomena such as phase change and pyrolysis reactions. As the degree of recycling increases (WVPE and WRPE), the endothermic phenomena r_2 become stronger extending through a wider range of temperatures. The TGA under the oxidative atmosphere can be visualized as supplementary material, Appendix G.

By integrating the DSC curves under air for VPE, WVPE, and WRPE, in the temperature range of reactions (r), the combustion enthalpies of the respective samples were about 2765, 3237, and 3665 J/g.

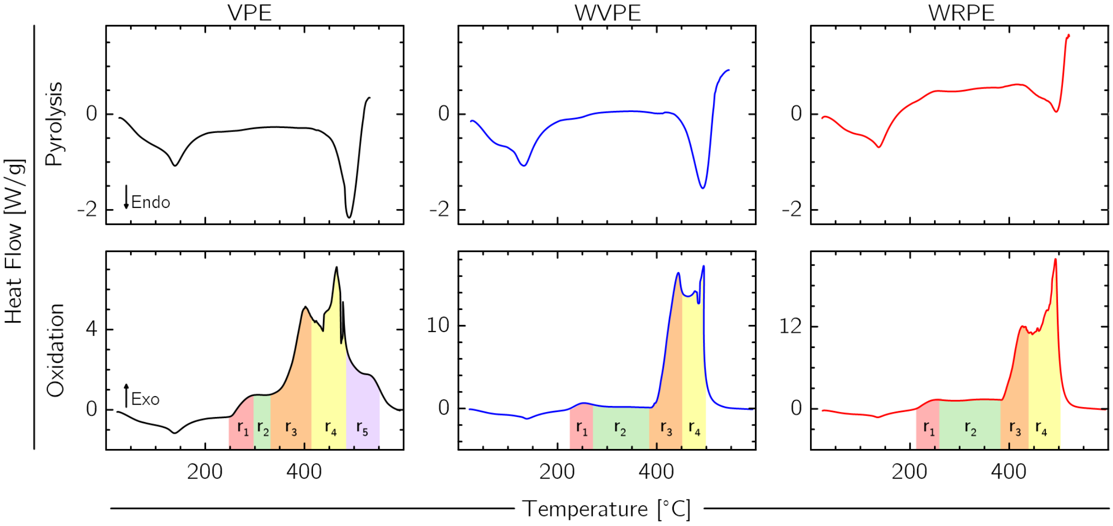

Figure 4.6: Polyethylene differential scanning calorimetry under inert and oxidative atmospheres at 20 °C/min, the heat flows.

4.3.5 Kinetic analysis

The plots obtained by the left-hand side of the equation of each isoconversional method considered against $1/T$ are shown in Fig. 4.7 for VPE, WVPE, and WRPE. The corresponding lines are obtained at different fraction reacted and different heating rates. It can be seen from Fig. 4.7 that two groups of straight lines are formed depending on the degree of fraction reacted and method: one with smaller slope and lower fraction reacted degree ($\alpha < 0.25$) and the other steeper lines and $0.25 < \alpha < 0.95$. A different tendency was observed when Friedman's isoconversional method was used.

For comparison, the values of the activation energy were determined in a wide range of $\alpha = 0.05 - 0.95$ with a step of 0.05 and the dependence was reported in a plot E vs. α, Fig. 4.8. This dependence is a warning about multi-step kinetics existence in a given process [33]. As can be seen from the curves presented in Fig. 4.8, from 0.05 to 0.95 of fraction reacted, the average activation energy (E_{avg}), varies in a range of 216 ± 46 kJ/mol, 225 ± 43 kJ/mol, and 186 ± 61 kJ/mol for VPE, WVPE, and WRPE, respectively. In percentage terms, the difference between the maximum (E_{max}) and minimum (E_{min}) values of the average are respectively 43%, 38%, and 66%.

Although the literature shows that a strong dependence of E within a wide range of α means that a given process cannot be considered as a single-step one, just one work pointed out the acceptable degree of this dependence, [53]. That author considers that the ratio $(E_{max} - E_{min})/E_{avg}$ should be less than 10%, which constitutes noteworthy impasse because many authors have been using a single-step reaction to describe multi-step ones with a relative degree of success [23, 24, 25, 26, 27, 28] in rebuild thermogravimetric curves. On the other hand, if the preliminary results from isoconversional methods are used as a tool of diagnostic toward detailed kinetics - related to the necessity of controlling the products yields at different reaction velocities -, a multi-step treatment should be performed.

The generalized master plots are shown in Fig. 4.9. At the top part of the figure, each column contains the respective master plot of VPE, WVPE, and WRPE with all theoretical models investigated. At the bottom part, only the most suitable models are presented. The RMSE between the experimental data and the theoretical reaction models, used to identify the best correspondence, are shown in Fig. 4.10.

The master plots results suggest that the thermal degradation of VPE could be governed by Avrami-Erofeev models (A_2, A_3, and A_4), as well as, by a first-order model (F_1). The same trend was obtained for the recycled samples, which, in addition, can also be approximated by the contracting geometry (R_3) and three-dimensional diffusion (D_3) models. These model equivalences were already expected since according to [48], it is not possible to distinguish between the models R_3 and D_3, and also is impossible

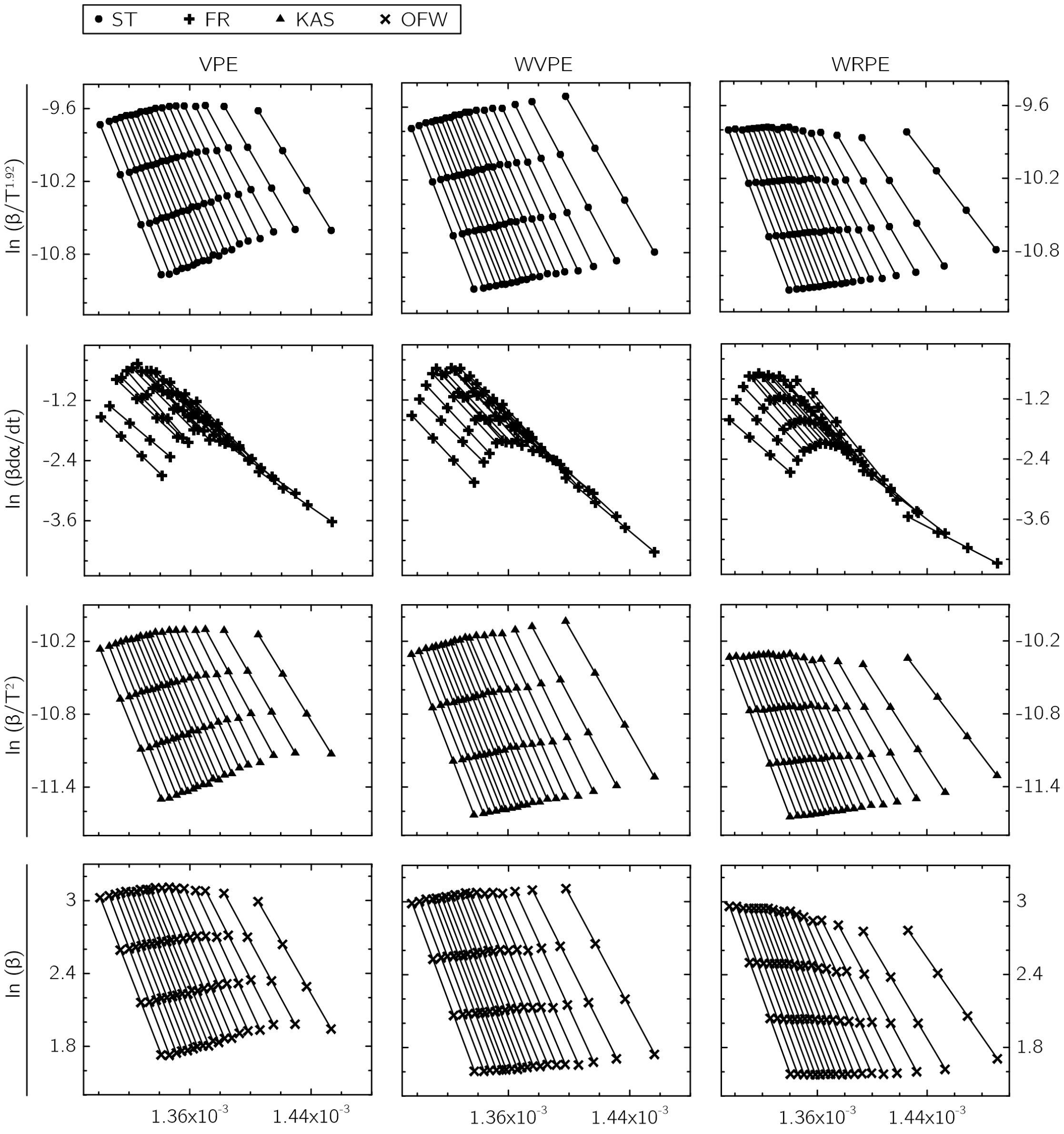

Figure 4.7: Isoconversional plot of Starink, Friedman, Kissinger-Akahira-Sunose and Ozawa-Flynn-Wall methods in a range of $\alpha = 0.05 - 0.95$ - from the TG under inert atmosphere data.

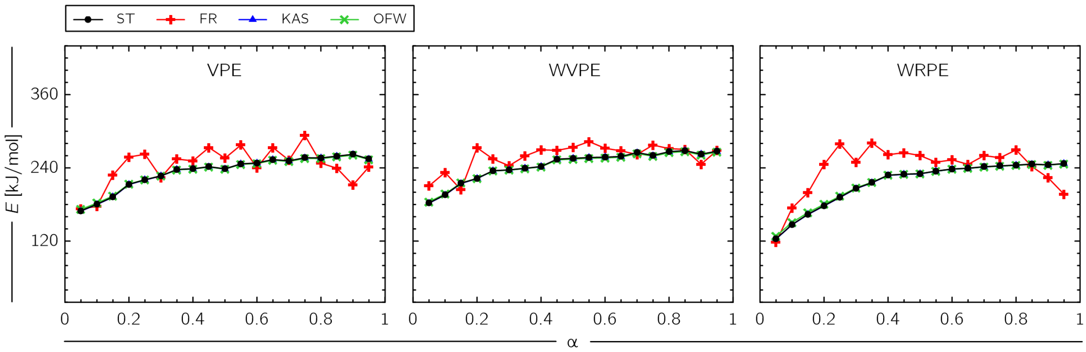

Figure 4.8: Distribution of activation energy from isoconversional methods in a range of $\alpha = 0.05 - 0.95$.

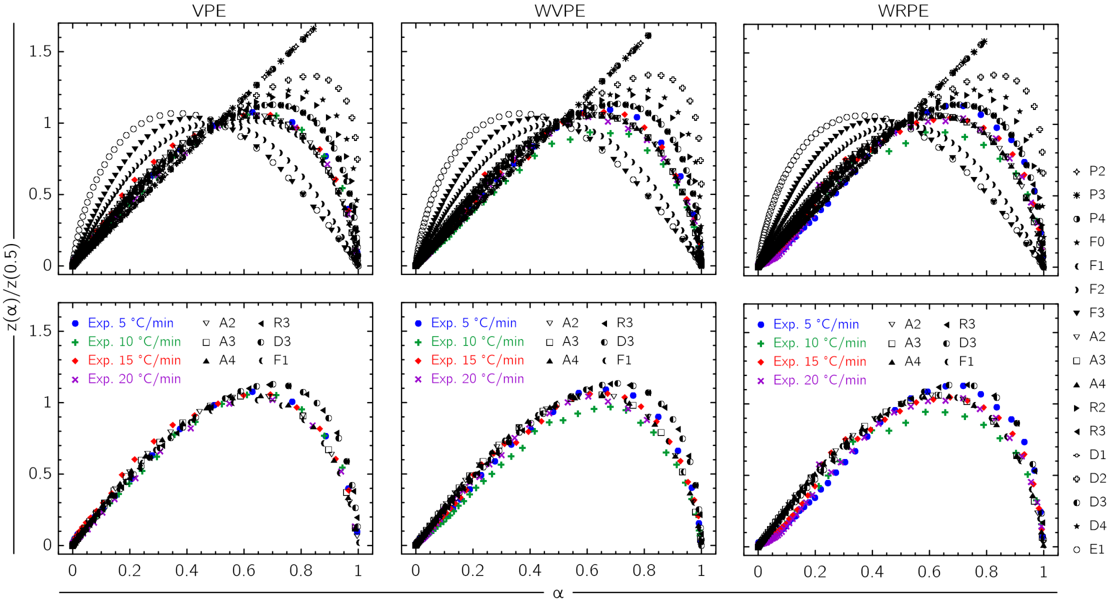

Figure 4.9: At the top: theoretical masterplots of different reaction models; bottom: the best master plots *vs.* experimental data calculated by Eq. 5.7.

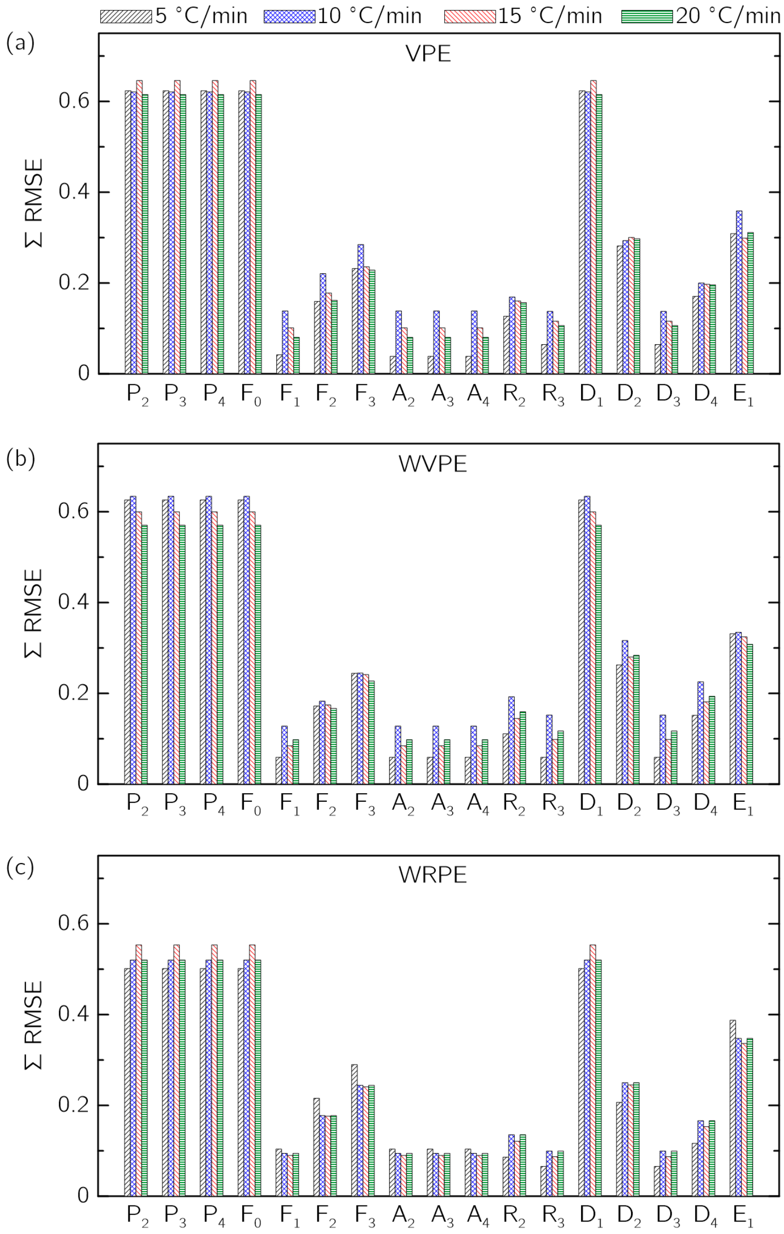

Figure 4.10: Sum of the RMSE between the experimental TG curve and each reaction model listed in the Table 4.2. (a) for VPE, (b) for WVPE, and (c) for WRPE.

to discern the differences between a first-order and Avrami-Erofeev models.

It is noteworthy that, although a number of experimental curves at different heating rates result in a series of master plots, a single dependence on α can be observed, which is practically independent of β, see in Fig. 4.9.

The values of the pre-exponential factor were determined using the reaction model predicted by Criado master plots and Eq. 4.4. The range of calculated values of E and A are summarized in Table 4.6 and Table 4.7, organized by sample and by the method. The dependence of the pre-exponential factor on the conversion is reported in Fig. 4.11. In general, the dependence of $\ln A$ on α increase as more recycled is the sample, which follows the same trend of $E(\alpha)$.

The kinetic parameters obtained from the different isoconversional methods were used to reconstruct the conversion profiles in comparison with the experimental data, Fig. 4.12, and then the RMSE was calculated to check the accuracy of each method, Fig. 4.13. From this analysis, the Starink method showed to be the most accurate approach to determine the kinetic parameters of the pyrolysis process of polyethylene virgin and wastes. On the other hand, the reconstruction of the conversion profiles using KAS and OFW methods did not match well the experiments, as already reported by [27].

For the values obtained from the Starink method, the logarithmic form of the pre-exponential factor was plotted against E. A linear relationship is observed between them, Fig. 4.14. The correlation coefficient, close to 1, indicates that for all heating rates the values of A are in accordance with the distributed activation energy along the conversion process.

Table 4.6: Range of activation energy, E [kJ/mol], for the pyrolysis of VPE, WVPE, and WRPE obtained from isoconversional methods at various heating rates.

Sample	β [°C/min]	ST	FR	KAS	OFW
VPE	5 10 15 20	170 - 262	173 - 293	169 - 262	172 - 261
WVPE	5 10 15 20	183 - 268	204 - 283	182 - 268	184 - 267
WRPE	5 10 15 20	124 - 247	118 - 281	124 - 247	128 - 247

Table 4.7: Range of pre-exponential factor, A [1/min], for the pyrolysis of VPE, WVPE, and WRPE obtained from isoconversional methods at various heating rates.

Sample	β [°C/min]	ST	FR	KAS	OFW
VPE	5	2.51×10^{12} - 1.15×10^{18}	7.65×10^{12} - 2.35×10^{20}	5.52×10^{10} - 9.86×10^{17}	9.79×10^{10} - 8.66×10^{17}
	10	5.65×10^{12} - 1.47×10^{18}			
	15	5.13×10^{12} - 8.23×10^{17}			
	20	4.03×10^{12} - 1.08×10^{18}			
WVPE	5	2.16×10^{13} - 2.98×10^{18}	4.30×10^{14} - 5.93×10^{19}	5.03×10^{11} - 2.06×10^{18}	7.76×10^{11} - 1.73×10^{18}
	10	1.82×10^{13} - 2.88×10^{18}			
	15	3.86×10^{13} - 2.88×10^{18}			
	20	2.58×10^{13} - 2.94×10^{18}			
WRPE	5	9.61×10^{8} - 9.57×10^{16}	3.90×10^{8} - 9.87×10^{19}	1.98×10^{7} - 7.32×10^{16}	6.16×10^{7} - 7.30×10^{16}
	10	7.36×10^{8} - 8.65×10^{16}			
	15	1.14×10^{9} - 9.23×10^{16}			
	20	1.25×10^{9} - 8.24×10^{16}			

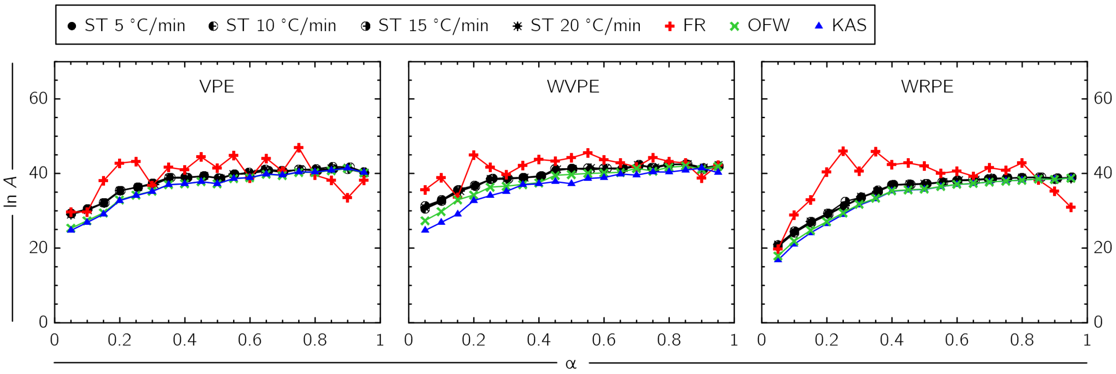

Figure 4.11: Distribution of pre-exponential factor from isoconversional methods in a range of $\alpha = 0.05 - 0.95$.

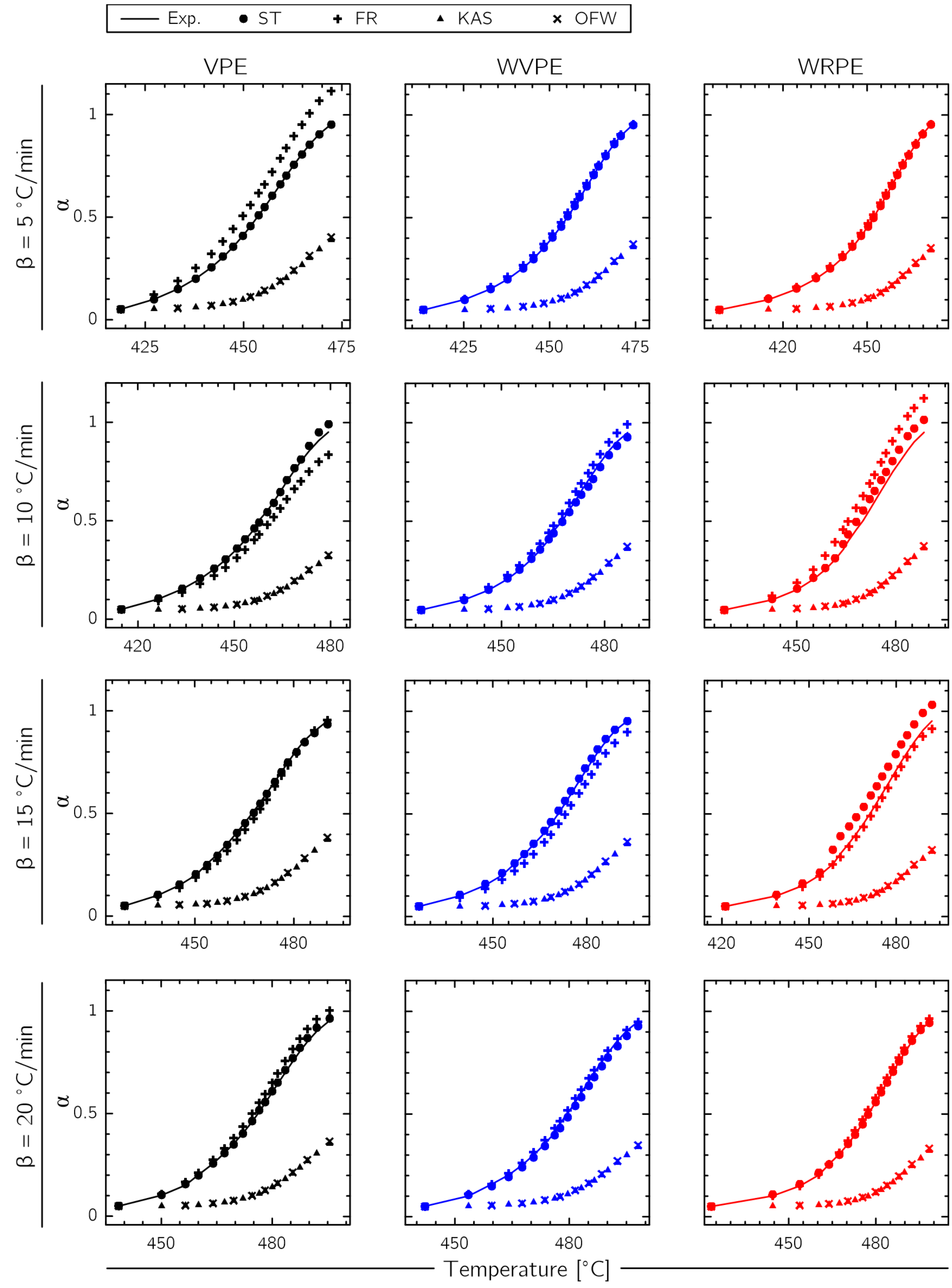

Figure 4.12: Fitness of the thermogravimetric analysis (fraction reacted, α) under inert atmosphere using the kinetic parameters obtained from isoconversional methods at various heating rates.

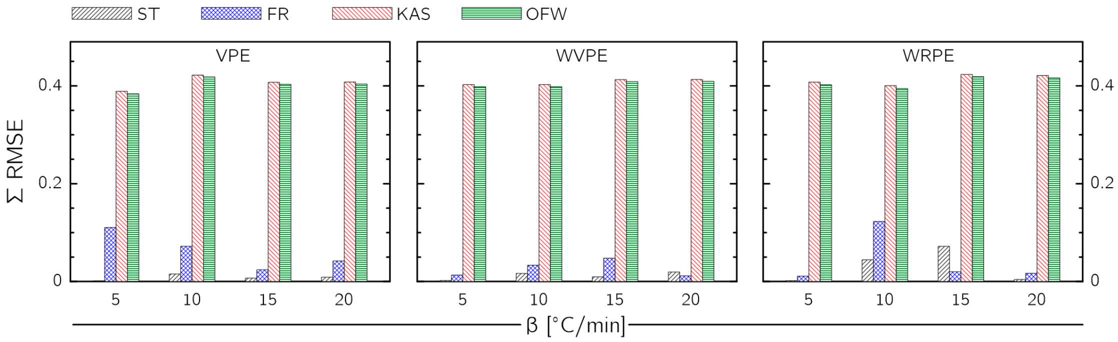

Figure 4.13: Comparison of different isoconversional methods based on the sum of the RMSE between the experimental and reconstructed fraction reacted (α).

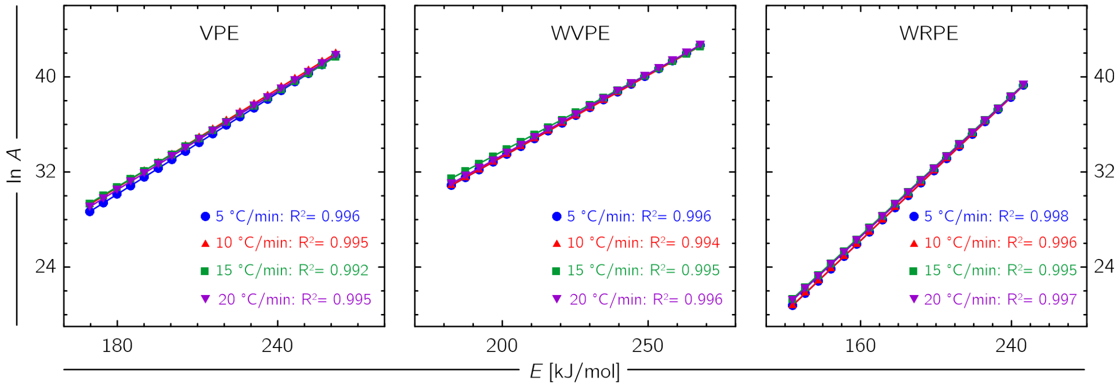

Figure 4.14: Estimated ln A versus E from the Starink method.

4.3.6 Pyrolysis pathway

According to the results presented above, the significant variation of the kinetics values indicated that polyethylene pyrolysis is indeed kinetically complex. The evidence was also observed using the characterization results, where the XRD analysis shows that PE is composed of bonded compounds, and a strong degree of overlapping was identified in DSC analysis. Therefore, a multi-step pathway is delineated below:

- Pre-heating. The stage in which the sample absorbs heat. At this stage, only increases in the sample temperature take place.
- Melting. The heat promotes changes from the solid phase, $PE_{(s)}$, to the liquid phase, $PE_{(l)}$, in an endothermic process.
- Bond breaking. After the melting, the bonds linking the compounds forming the PE are thermally broken in an endothermic process. The result is a multi-compound liquid mixture in which compounds with diverse molecular properties are present [54]. From this stage onwards, the liquid phase pyrolysis of the main compounds can take place.
- Evaporation. Once the boiling point of each compound is reached, the liquid phase starts to be vaporized.
- Pyrolysis reaction. Once a compound starts evaporation, it can be thermally cracked in series with respect to the evaporation, and in parallel with respect to the other compounds pyrolysis. The pyrolysis products formed in the individual reactions are grouped in P_p.

Note that, the phase change $PE_{(s)}$to $PE_{(l)}$ does not account for mass losses; negligible mass losses can be attributed to the bond-breaking [55]; the multi-compound mixture in the liquid phase is formed only by the compounds identified by XRD. Even if the compounds n-paraffin$_{(g)}$ and paraffin wax$_{(g)}$ are mixtures of hydrocarbons, they are modeled by their main constituents [56, 57]. The amorphous phases can be considered fractions of irregular groups remaining attached in each separated rigid structure (crystalline phase) identified [58]. Also, the pyrolysis products may include oil, wax, and gas [25, 29, 32, 59], and their yields are not investigated in the present work.

The pyrolysis pathways for VPE, WVPE, and WRPE are shown in the schemes in Table 4.8.

To implement the reaction mechanism shown in Table 4.8 in numerical modeling, the stoichiometric and kinetic parameters of each reaction must be quantified, as well as,

Table 4.8: Schemes of the pyrolysis pathways for VPE, WVPE and WRPE.

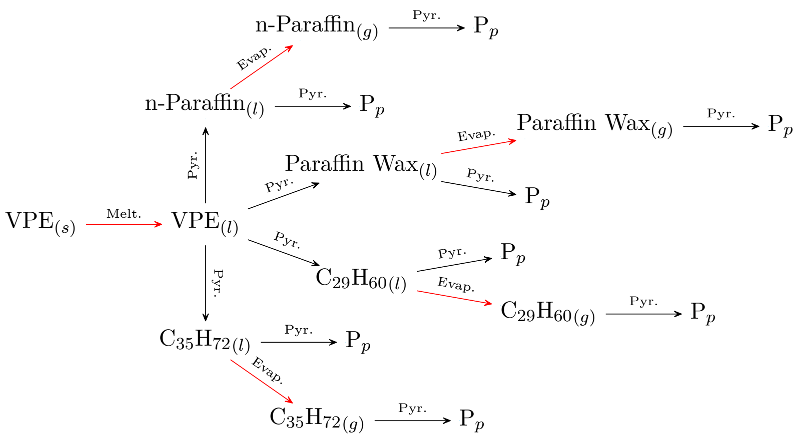

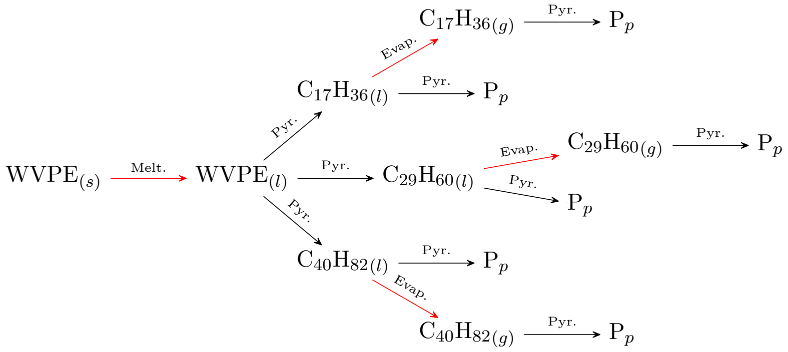

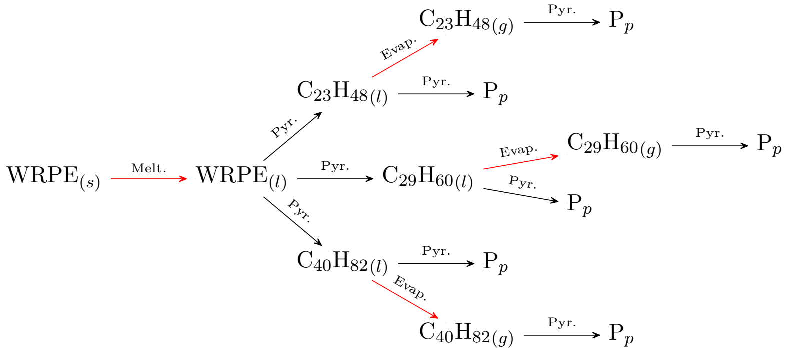

Melt. and Evap. means melting and evaporation phase changes/
Pyr. means pyrolysis reactions / P_p may include oil, wax, and gas.

the amorphous phase may be incorporated in the solid phase definition. It is necessary to reformulate the kinetic parameter estimation process as an optimization problem in terms of an objective function [32, 60, 61]. This procedure is beyond the scope of the present study, and for this reason, the kinetic parameters are not determined.

4.4 Conclusion

In this paper, two types of PE wastes with different degrees of recycling were used to investigate the influence of recycling stress history on the pyrolysis. The main results suggest that the thermal and mechanical stress promotes the increase of long carbon chains while weakening the boundaries among the compounds. This might explain the fact that recycled waste needs less activation energy than recycled samples to degrade thermally. The waste of recycled polyethylene presented the lowest enthalpy of pyrolysis, at about 205 J/g.

The DSC trials evidenced a multi-step reaction behavior. This behavior was confirmed by using different isoconversional methods for the kinetic study. Large variations around the average activation energy values were observed. The waste of recycled polyethylene presented a higher variation of about 66% in the range of 186 ± 61 kJ/mol. Also, it needs less activation energy than VPE and WVPE to degrade thermally. The degradation of all samples can follow Avrami-Erofeev (A_2, A_3, and A_4) and first-order (F_1) models, also, the recycled can be described by contracting geometry (R_3) and three-dimensional diffusion (D_3) models.

The pyrolysis pathway is a series-parallel phenomenon dominated mainly by the competition of evaporation and pyrolysis reactions.

We recommend that the physical stress history between different categories of polyethylene waste should be considered for kinetics purposes, as well as, for the modeling of the product recovery process.

Bibliography

[1] PlasticsEurope. The facts 2018. *PlasticsEurope*, 2018.

[2] Mónica Calero, María Ángeles Martín-Lara, Verónica Godoy, Lucía Quesada, David Martínez, Francisco Peula, and José Manuel Soto. Characterization of plastic materials present in municipal solid waste: preliminary study for their mechanical recycling. *Detritus*, In Press:1, 2018.

[3] S. M. Al-Salem, P. Lettieri, and J. Baeyens. Recycling and recovery routes of plastic solid waste (PSW): A review. *Waste manag.*, 29(10):2625–43, oct 2009.

[4] Bo Zhang, Zhaoping Zhong, Kuan Ding, and Zuwei Song. Production of aromatic hydrocarbons from catalytic co-pyrolysis of biomass and high density polyethylene: Analytical Py–GC/MS study . *Fuel*, 139(0):622–628, 2015.

[5] Farah Obeid, Joseph Zeaiter, Ala'a H Al-Muhtaseb, and Kamal Bouhadir. Thermo-catalytic pyrolysis of waste polyethylene bottles in a packed bed reactor with different bed materials and catalysts . *Energy Convers. Manage.*, 85(0):1–6, 2014.

[6] Xue-Cai Tan, Chun-Chun Zhu, Qing-Kun Liu, Tian-Yi Ma, Pei-Qing Yuan, Zhen-Min Cheng, and Wei-Kang Yuan. Co-pyrolysis of heavy oil and low density polyethylene in the presence of supercritical water: The suppression of coke formation . *Fuel Process. Technol.*, 118(0):49–54, 2014.

[7] Jan Mosio-Mosiewski, Marek Warzala, Ireneusz Morawski, and Tadeusz Dobrzanski. High-pressure catalytic and thermal cracking of polyethylene . *Fuel Process. Technol.*, 88(4):359–364, 2007.

[8] Fan Bai, Chun-Chun Zhu, Yin Liu, Pei-Qing Yuan, Zhen-Min Cheng, and Wei-Kang Yuan. Co-pyrolysis of residual oil and polyethylene in sub- and supercritical water . *Fuel Process. Technol.*, 106(0):267–274, 2013.

[9] L. Yermán, D. Cormier, I. Fabris, J. Carrascal, J. L. Torero, J. I. Gerhard, and Y.-L. Cheng. Potential Bio-oil Production from Smouldering Combustion of Faeces. *Waste Biomass Valorization*, 8(2):329–338, mar 2017.

[10] M Sarker, MM Rashid, MS Rahman, and M Molla. Low and high density polyethylene waste plastics conversion into liquid hydrocarbon fuel. *chimica oggi/Chemistry Today*, 30(6), 2012.

[11] Moinuddin Sarker, Mohammad Mamunor Rashid, Mohammed Molla, and Muhammad Sadikur Rahman. Thermal conversion of waste plastic (hdpe, pp, ps) to produce mixture of hydrocarbons. *American Journal of Environmental Engineering*, 2(5):128–136, 2012.

[12] Alejandro Villanueva and Peter Eder. End-of-waste criteria for waste plastic for conversion. *Institute for Prospective Technological Studies*, 2014.

[13] Kim Ragaert, Laurens Delva, and Kevin Van Geem. Mechanical and chemical recycling of solid plastic waste. *Waste Management*, 69:24–58, 2017.

[14] Mădălina Grigore. Methods of recycling, properties and applications of recycled thermoplastic polymers. *Recycling*, 2(4):24, 2017.

[15] Henry L. Friedman. Kinetics of thermal degradation of char-forming plastics from thermogravimetry. Application to a phenolic plastic. *Journal of Polymer Science Part C: Polymer Symposia*, 6(1):183–195, mar 1964.

[16] Ozawa Takeo. A New Method of Analyzing Thermogravimetric Data. *Bulletin of the Chemical Society of Japan*, 38(11):1881–1886, 1965.

[17] Joseph H. Flynn and Leo A. Wall. A quick, direct method for the determination of activation energy from thermogravimetric data. *Journal of Polymer Science Part B: Polymer Letters*, 4(5):323–328, may 1966.

[18] Joseph H. Flynn and Leo A. Wall. General treatment of the thermogravimetry of polymers. *Journal of Research of the National Bureau of Standards Section A: Physics and Chemistry*, 70A(6):487, nov 1966.

[19] J. H. Flynn. The isoconversional method for determination of energy of activation at constant heating rates. *Journal of Thermal Analysis*, 27(1):95–102, may 1983.

[20] H E Kissinger. Reaction Kinetics in Differential Thermal Analysis. *Analytical Chemistry*, 29(11):1702–1706, 1957.

[21] T Akahira and T Sunose. Method of determining activation deterioration constant of electrical insulating materials. *Res Rep Chiba Inst Technol (Sci Technol)*, 16:22–31, 1971.

[22] M.J Starink. The determination of activation energy from linear heating rate experiments: a comparison of the accuracy of isoconversion methods. *Thermochimica Acta*, 404(1-2):163–176, sep 2003.

[23] P. Grammelis, P. Basinas, a. Malliopoulou, and G. Sakellaropoulos. Pyrolysis kinetics and combustion characteristics of waste recovered fuels. *Fuel*, 88(1):195–205, jan 2009.

[24] A. Aboulkas, K. El harfi, and A. El Bouadili. Thermal degradation behaviors of polyethylene and polypropylene. Part I: Pyrolysis kinetics and mechanisms. *Energy Convers. Manage.*, 51(7):1363–1369, jul 2010.

[25] Sang Shin Park, Dong Kyun Seo, Sang Hoon Lee, Tae-U. Yu, and Jungho Hwang. Study on pyrolysis characteristics of refuse plastic fuel using lab-scale tube furnace and thermogravimetric analysis reactor. *J. Anal. Appl. Pyrolysis*, 97(0):29–38, sep 2012.

[26] L.S. Diaz Silvarrey and A.N. Phan. Kinetic study of municipal plastic waste. *International Journal of Hydrogen Energy*, 41(37):16352–16364, oct 2016.

[27] Sahar Khedri and Siamak Elyasi. Kinetic analysis for thermal cracking of HDPE: A new isoconversional approach. *Polymer Degradation and Stability*, 129:306–318, jul 2016.

[28] Pallab Das and Pankaj Tiwari. Thermal degradation kinetics of plastics and model selection. *Thermochim. Acta*, 654(June):191–202, 2017.

[29] J.A. Conesa, R. Font, A. Marcilla, and J.A. Caballero. Kinetic model for the continuous pyrolysis of two types of polyethylene in a fluidized bed reactor. *J. Anal. Appl. Pyrolysis*, 40-41:419–431, may 1997.

[30] Omar Gutiérrez and Humberto Palza. Effect of carbon nanotubes on thermal pyrolysis of high density polyethylene and polypropylene. *Polymer Degradation and Stability*, 120:122 – 134, 2015.

[31] Paula A. Costa, Filomena J. Pinto, Ana. M. Ramos, Ibrahim K. Gulyurtlu, Isabel A. Cabrita, and Maria. S. Bernardo. Kinetic Evaluation of the Pyrolysis of Polyethylene Waste. *Energy Fuels*, 21(5):2489–2498, sep 2007.

[32] S M Al-Salem and P Lettieri. Kinetic study of high density polyethylene (HDPE) pyrolysis. *Chem. Eng. Res. Des.*, 88(12):1599–1606, 2010.

[33] Sergey Vyazovkin, Alan K. Burnham, José M. Criado, Luis A. Pérez-Maqueda, Crisan Popescu, and Nicolas Sbirrazzuoli. ICTAC Kinetics Committee recommendations for performing kinetic computations on thermal analysis data. *Thermochimica Acta*, 520(1-2):1–19, 2011.

[34] Y Badr, ZI Ali, AH Zahran, and RM Khafagy. Characterization of gamma irradiated polyethylene films by DSC and X-ray diffraction techniques. *Polymer International*, 49(12):1555–1560, dec 2000.

[35] S. Ikhlef, S. Nekkaa, M. Guessoum, and N. Haddaoui. Effects of Alkaline Treatment on the Mechanical and Rheological Properties of Low-Density Polyethylene/ Spartium junceum Flour Composites. *ISRN Polym. Sci.*, 2012:1–7, 2012.

[36] Fernando G Souza Jr, Marcos TD Orlando, Ricardo C Michel, José Carlos Pinto, Tainá Cosme, and Geiza E Oliveira. Effect of pressure on the structure and electrical

conductivity of cardanol–furfural–polyaniline blends. *Journal of Applied Polymer Science*, 119(5):2666–2673, 2011.

[37] Michael E. Brown, editor. *Introduction to Thermal Analysis*, volume 1 of *Hot Topics in Thermal Analysis and Calorimetry.* Kluwer Academic Publishers, Dordrecht, 2004.

[38] Edward M. Barrall. Precise determination of melting and boiling points by differential thermal analysis and differential scanning calorimetry. *Thermochim. Acta*, 5(4):377–389, feb 1973.

[39] D Dollimore, T A Evans, Y F Lee, G P Pee, and F W Wilburn. The significance of the onset and final temperatures in the kinetic analysis of TG curves. *Thermochimica Acta*, 196(2):255–265, 1992.

[40] Morten Gunnar Grønli, Gábor Várhegyi, and Colomba Di Blasi. Thermogravimetric Analysis and Devolatilization Kinetics of Wood. *Industrial & Engineering Chemistry Research*, 41(17):4201–4208, 2002.

[41] Marcin Wojdyr. Fityk : a general-purpose peak fitting program. *Journal of Applied Crystallography*, 43(5):1126–1128, oct 2010.

[42] J. D. Hanawalt, H. W. Rinn, and L. K. Frevel. Chemical analysis by x-ray diffraction. *Industrial & Engineering Chemistry Analytical Edition*, 10(9):457–512, 1938.

[43] J. D. Hanawalt. Phase Identification by X-Ray Powder Diffraction Evaluation of Various Techniques. *Advances in X-ray Analysis*, 20:63–73, mar 1976.

[44] JD Hanawalt. History of the powder diffraction file. *Crystallography in North America-Apparatus and Methods*, pages 215–219, 1983.

[45] Saulius Gražulis, Adriana Daškevič, Andrius Merkys, Daniel Chateigner, Luca Lutterotti, Miguel Quirós, Nadezhda R. Serebryanaya, Peter Moeck, Robert T. Downs, and Armel Le Bail. Crystallography Open Database (COD): an open-access collection of crystal structures and platform for world-wide collaboration. *Nucleic Acids Research*, 40(D1):D420–D427, jan 2012.

[46] Soorya Kabekkodu. Pdf-2 2007. *ICDD Database*, 2007.

[47] Juan Rodríguez-Carvajal. Recent advances in magnetic structure determination by neutron powder diffraction. *Physica B: Condensed Matter*, 192(1-2):55–69, oct 1993.

[48] J.M. Criado. Kinetic analysis of DTG data from master curves. *Thermochimica Acta*, 24(1):186–189, may 1978.

[49] Pedro E. Sánchez-Jiménez, Luis A. Pérez-Maqueda, Antonio Perejón, and José M. Criado. Generalized master plots as a straightforward approach for determining the kinetic model: The case of cellulose pyrolysis. *Thermochimica Acta*, 552:54–59, jan 2013.

[50] John P. Elder. Reconciliation of Arrhenius and iso-conversional analysis kinetics parameters of non-isothermal data. *Thermochimica Acta*, 272:41–48, jan 1996.

[51] V.I. Selikhova, Yu.A. Zubov, N.F. Bakeyev, and G.P. Belov. Melting temperature, heat of melting and crystallinity determinations on polyethylene by differential scanning calorimetry. *Polymer Science U.S.S.R.*, 19(4):879 – 886, 1977.

[52] Anke Brems, Jan Baeyens, Carlo Vandecasteele, and Raf Dewil. Polymeric Cracking of Waste Polyethylene Terephthalate to Chemicals and Energy. *J. Air Waste Manage. Assoc.*, 61(7):721–731, jul 2011.

[53] Sergey Vyazovkin. *Isoconversional Kinetics of Thermally Stimulated Processes.* Springer International Publishing, Cham, 2015.

[54] Sanket A Deshmukh, Ganesh Kamath, Vilas G Pol, and Subramanian K R S Sankaranarayanan. Kinetic Pathways To Control Hydrogen Evolution and Nanocarbon Allotrope Formation via Thermal Decomposition of Polyethylene. *J. Phys. Chem. C*, 118(18):9706–9714, 2014.

[55] Seth E. Levine and Linda J. Broadbelt. Detailed mechanistic modeling of high-density polyethylene pyrolysis: Low molecular weight product evolution. *Polymer Degradation and Stability*, 94(5):810 – 822, 2009.

[56] William R. Turner, Donald S. Brown, and Donald V. Harrison. Properties of Paraffin Waxes. *Ind. Eng. Chem.*, 47(6):1219–1226, jun 1955.

[57] Syukri Himran, Aryadi Suwono, and G. Ali Mansoori. Characterization of Alkanes and Paraffin Waxes for Application as Phase Change Energy Storage Medium. *Energ. Source*, 16(1):117–128, jan 1994.

[58] Josef Chmelař, Richard Pokorný, Patrik Schneider, Klára Smolná, Petr Bělský, and Juraj Kosek. Free and constrained amorphous phases in polyethylene: Interpretation of 1h nmr and saxs data over a broad range of crystallinity. *Polymer*, 58:189 – 198, 2015.

[59] J.A. Conesa, A. Marcilla, J.A. Caballero, and R. Font. Comments on the validity and utility of the different methods for kinetic analysis of thermogravimetric data. *J. Anal. Appl. Pyrolysis*, 58-59:617–633, apr 2001.

[60] Marco Aurélio Bazelatto Zanoni, Henrique Massard, and Márcio Ferreira Martins. Formulating and optimizing a combustion pathways for oil shale and its semi-coke . *Combust. Flame*, 159(10):3224–3234, 2012.

[61] Guillermo Rein, Chris Lautenberger, A Carlos Fernandez-Pello, Jose L Torero, and David L Urban. Application of genetic algorithms and thermogravimetry to determine the kinetics of polyurethane foam in smoldering combustion. *Combust. Flame*, 146(1):95–108, 2006.

Chapter 5

Combustion-driven pyrolysis reactor: converting LDPE waste into hydrocarbons

Contents

Summary

In this work, a new concept of energetically self-sustaining pyrolysis reactor was presented as an alternative to transform waste of recycled polyethylene, WRPE, into hydrocarbons. The method consists of propagating a combustion front using low-grade fuels and drive the heat of combustion to plastic waste thermal cracking.

Twenty-nine (29) experiments were carried out in the combustion-driven pyrolysis reactor, C-DPyR, under several operating conditions of bed composition and inlet airflow, resulting in different temperature profiles, i.e., energy availability to perform pyrolysis. The final pyrolysis products were categorized into a liquid, wax, gas, and solid residue. However, to produce a high-grade raw material with great energy density and calorific value, the experiments focused on recovering wax while using low thermal energy for conversion.

The wax was then characterized by TGA and DSC to verify different thermal behavior among the materials recovered. The TGA data were also used to perform kinetics computations. ATR-FTIR identified the functional groups constituting the waxes.

The experiments that reached great thermal energies resulted in a high amount of gas produced, on average of 74 wt.%, confirming that the heat available for pyrolysis was more than sufficient to crack the samples. Decreasing the thermal energy beyond the 497 kJ limit, a perceptible change in the product yield distribution was observed: the gas decreased to around 60 wt.%, increasing the amount of wax from 14 wt.% to about 34 wt.%. For intermediate to low thermal energy experiments, the wax amount significantly increased to an average of 55 wt.%. A maximum of about 87 wt.% of wax was recovered from an experiment made available for pyrolysis 80 kJ of energy.

The wax characterization showed that waxes were almost wholly converted between 25-500 °C during pyrolysis marked by competing reactions. It was assumed that these reactions with some overlapping degrees might be associated with the main functional groups forming the wax and identified by FTIR. DSC curves evidenced two zones, one endothermic, an average enthalpy of 80 J/g, and another exothermic associated with an average enthalpy of 2115 J/g. The FTIR established the functional wax groups composed mainly of C-H, CH_2, and CH_3, the same groups present in the FTIR spectra of LDPE.

Using isoconversional methods, both single-step and multi-step kinetic analysis of the wax pyrolysis was performed to determine the kinetic triplets (activation energy, E, pre-exponential factor, A, and reaction model, $f(\alpha)$). For both approaches, the TGA curves were accurately reconstructed, confirming reliable kinetic predictions.

Candidate contribution: Conceptualization, methodology, software, validation, formal analysis, resources, data curation, writing - original draft, Writing - review & editing, visualization.

5.1 Introduction

The number of plastics produced and then disposed of in the environment has dramatically impacted humans and the ecosystem [1, 2, 3]. Plastic bags and foamed plastic products are classified as single-use plastics, often also referred to as disposable plastics, and the general perception of their presence in the environment raises essential concerns about a solution to the problem they pose [4, 5]. However, the production of single-use plastics for packaging and personal protective equipment (like face masks, gloves, and gowns) suddenly skyrocketed around the world, putting the plastic reduction policies in check [6]. Still, the goal of recycling plastic to reduce high rates of plastic pollution while putting less pressure on virgin materials to produce brand new plastic products persist noble. This approach is known to help conserve resources and divert plastics from landfills and not planned destinations, such as the marine environment [2, 7, 8].

Lots of processes emerged [9, 10, 11], ones disappeared [12, 13], and others kept under investigation, such as pyrolysis [10, 14, 15] for waste plastics to raw materials. The pyrolysis products' value mainly depends on the waste composition and the reactor technologies in maximizing the desired product [16]. From the many technologies adapted to as pyrolysis reactors [13, 14, 17, 18], the insufficient heat transfer to carry out the process is reported to be the Achilles heel [16].

Although the heat transfer plays an important role, the pyrolysis product spectra in the bench-scale experiments mainly depend on the waste composition - polyethylene at low pyrolysis temperature results in waxes, α-olefins and paraffin oils, at high, in gases and light oils [16, 19]. At low temperature or high, polystyrene results in styrene and its oligomers [20]. Some works focused on obtaining liquid products [21, 22, 23], others on gases [24]. Nevertheless, polyolefins' pyrolysis, especially polyethylene and polypropylene, yield wax as one of the head products. In order to conveniently recover the waxes, the recovery systems must be designed to handle waxes [25]. Waxes can be seen as a high-grade raw material, stable, relatively homogeneous, with far greater energy density and calorific value than the waste polyethylene, providing significant benefits in logistics, handling, and storage, opening up a wide range of potential uses [26]. For these reasons, polyethylene waxes are attractive for many fields of application, and developing new uses for it, especially in energy-saving applications, should make significant contributions to meet the recycling plastic challenges [23, 27, 28].

In terms of wax characterization relative to its original matrix, waste of recycled polyethylene in the present work context, the terminology for a polyethylene solid or wax may be of little value for distinguishing actual crystal structures [29]. Conversely, their thermal behaviors are quite different concerning the type of transformations, a series of discrete [30, 31, 32] or continuous transformations [33]. Furthermore, it is necessary to characterize wax analytically. FTIR spectrometry is widely used for polymer identification [29, 34, 35], and, more specifically, ATR-FTIR has been shown to give excellent results [36]. The analysis setup is completed by evaluating the wax by thermogravimetry (TGA) [32, 33, 37] and differential scanning calorimetry (DSC) [33, 38] analysis.

The aim of the present work is to present a novel process to convert plastics waste toward an energy-dense material, easily recoverable, and using low-grade fuels as a heat-drive. A new concept of energetically self-sustaining pyrolysis reactor was specially developed and use for this purpose and polyethylene waxes are recovered and characterized. The thermochemical behavior of the polyethylene waxes is investigated and the identification of the functional groups of the samples is presented.

5.2 Materials and methods

5.2.1 Combustion-driven pyrolysis reactor (C-DPyR) experiments

A new concept of energetically self-sustaining pyrolysis reactor was specially developed and launched as an alternative to convert polyethylene waste into hydrocarbons. The methodology consists of propagating a smoldering combustion front in a charcoal-based bed and use the energy released by this process to promote the plastic waste thermal cracking. The C-DPyR, Fig. 5.1 a, has two independent chambers coaxially arranged, one to furnish heat another to convert the material. The full description of the C-DPyR reactor was done in Chapter 3. The pyrolysis chamber has an entrance through which plastic is fed and one outlet circuit through which the pyrolysis products flow. This outlet consists of a channel in stainless steel, 12 mm in diameter, and a length of a few millimeters less than the pyrolysis chamber's height. It is purposely arranged in a coaxial manner to allow the two-pass flow arrangement of the pyrolysis products through the region with the highest temperature inside the reactor. The zoomed region, Fig. 5.1 b, allows a better understanding of this configuration.

Twenty-nine (29) experiments were carried out in the C-DPyR under several operating conditions of bed composition and inlet airflow. The experimental results' reliability was verified through repeatability, empirical dimensionless correlations, and analysis of variance. A complete description of this study can be found in Chapter 3. In the combustion chamber, the experiments were carried out in a homogeneous and heterogeneous reactive porous medium. The first type of medium consists only of charcoal grains and the other in a mixture of charcoal and $NaHCO_3$ powder. Details on experimental setup and response variables are available in Chapter 4. Table 5.1 summarizes the primary input and outputs parameters of each run and provides an overview of these experimental investigations.

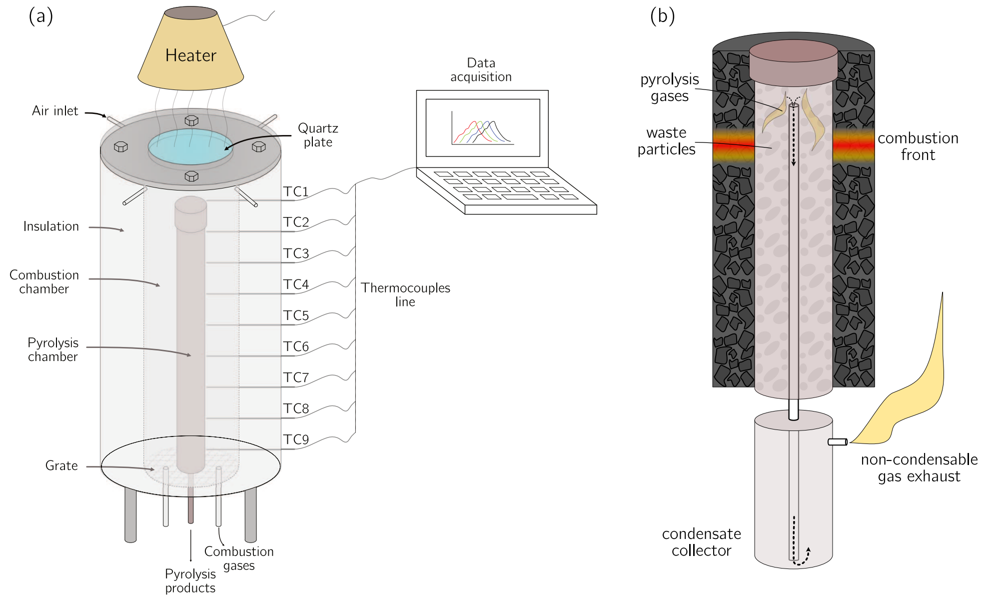

Figure 5.1: (a) Combustion-driven pyrolysis reactor. (b) The zoomed region shows the interior of the pyrolysis chamber.

Table 5.1: Input parameters and summarized results for different runs.

		Heat input			Pyrolysis yields			
Exp.	n*	T_z [°C]	Runtime [s]	Thermal energy [kJ]	Liq. [wt.%]	Wax [wt.%]	Gas [wt.%]	Residue [wt.%]
1	1	464	13816	1205	17.3	16.0	60.0	6.7
2	1	479	12636	867	12.7	12.1	69.1	6.1
3	1	494	6990	533	10.3	15.4	67.9	6.4
4	4	542	6824	723	6.9	0	81.0	12.1
5	1	518	5537	523	4.3	12.9	68.6	14.3
6	1	550	3668	420	3.8	12.9	63.6	19.7
7	1	588	3196	404	2.9	13.0	66.7	17.4
8	1	510	5420	592	9.1	15.2	69.7	6.1
9	1	477	4693	378	15.8	13.2	63.2	7.9
10	1	473	4216	497	0	34.3	59.7	6.0
11	1	540	3616	413	0	19.4	68.7	11.9
12	1	382	6631	447	0	45.2	37.1	17.7
13	4	386	3841	213	0	43.1	51.7	5.2
14	1	458	2116	253	0	40.3	56.7	3.0
15	4	356	5231	373	0	49.5	45.0	5.5
16	1	345	1390	77	0	34.8	62.3	2.9
17	2	402	994	80	0	87.0	10.1	2.9
18	2	389	2537	232	0	83.6	13.4	3.0

*Number of repetitions.

The plastic pyrolyzed in this study was a waste of recycled polyethylene (WRPE), Fig. 5.2, from the municipal solid waste stream. The material has non-uniform geometry (2 mm average grain size) and was used as received; approximately 63 g was pyrolyzed by experiment. The WRPE was previously characterized, and its composition and thermochemical behavior are available in Chapter 2, Duque et al. [33].

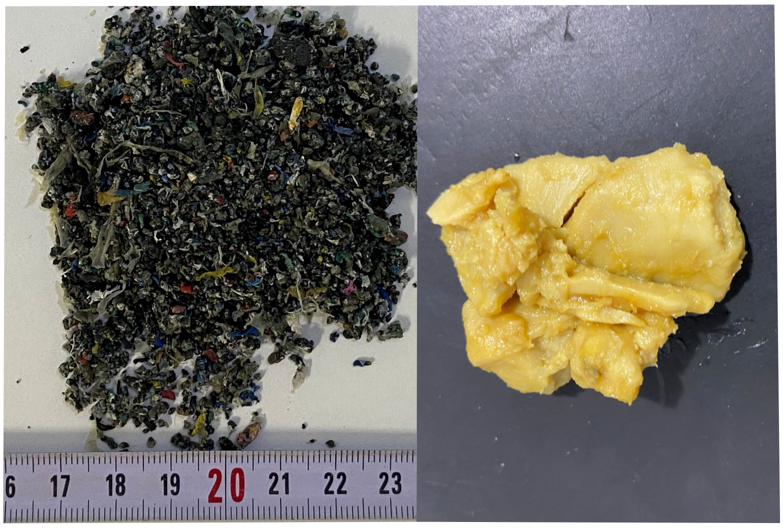

Figure 5.2: Waste of recycled polyethylene, WRPE, before pyrolysis (left), and polyethylene wax recovered (right).

5.2.2 Hydrocarbons products characterization

Pyrolysis products were categorized into intermediate and final products: the intermediate resulted into condensable and non-condensable gases; the final into liquid, wax, gas, and solid residue. Condensable gases (wax and liquid fractions) were collected and quantified, while the non-condensable ones were exhausted into the atmosphere and its yields determined by mass balance, Eq. 5.1. The solid residue remaining in the pyrolysis chamber was ash and residual char [15]. In Eq. 5.1, X_{gas} represents the percentage of WRPE converted into gas in wt.%, m_{WRPE} is the initial mass of WRPE, m_{liq} is the mass of pyrolysis products in the liquid phase, m_{wax} is the mass of wax, and m_{res} is the mass of the solid remaining inside the pyrolysis chamber after the process, all masses in gramme.

$$X_{gas} = \frac{m_{WRPE} - m_{liq} - m_{wax} - m_{res}}{m_{WRPE}} \times 100 \tag{5.1}$$

Representative samples of the condensable pyrolysis products were collected and characterized. The characterization aimed to study the thermochemical behavior through thermogravimetric analysis (TGA) coupled with differential scanning calorimetry (DSC) and also the identification of the functional groups of the samples through Fourier-Transform Infrared Spectroscopy (FTIR).

TGA and DSC characteristics were obtained on an STA 449F3 from NETZSCH Instruments based on the recommendations of the International Confederation for Thermal Analysis Calorimetry (ICTAC) [39] to ensure the quality of the experimental data collected. A total mass sample in the range of 15-17 mg was placed in an Al_2O_3 crucible, and then the whole system was degassed and filled with N_2 (carrier gas: 60 ml/min, 99.999% purity). The sample was progressively heated from 20-700 °C at three heating rates, β, 5, 10, and 15 °C/min. The integrated areas from DSC curves versus time intervals were used to represent melting and pyrolysis enthalpies. Fityk software, version 0.9.8.57 [40], was used to perform the integrations.

FTIR spectra were obtained with a Tensor 27 spectrophotometer from Bruker. The samples were scanned in the range of 4000 to 600 cm^{-1}, and the functional groups were identified by the ATR method. The identifications were made by comparing the spectrum from an 'unknown' with previously recorded reference spectra available from libraries [41] and scientific articles, i.e., computer-based spectral searching.

5.2.3 Kinetics

TGA data were processed to obtain the wax yield's degradation characteristics and perform kinetic computations. The same methodology presented in Chapter 2 [33] was used to identify the reaction zones (the onset and offset temperatures of each reaction) in the TGA and their respective mass losses.

To extract the kinetic triplet (activation energy, E, pre-exponential factor, A, and reaction model, $f(\alpha)$) from TGA data a differential and an integral isocoversional method were applied considering both a single-step [42] and a multi-step [43] approaches. The single-step rate of non-isothermal solid decomposition, $d\alpha/dt$, was expressed in terms of the Arrhenius rate constant, $k(T)$, and the reaction model, Eq. 5.2:

$$\frac{d\alpha}{dt} = k(T)f(\alpha) = Aexp\left(-\frac{E}{\Re T}\right)f(\alpha) \tag{5.2}$$

$$\alpha = \frac{m_0 - m_i}{m_0 - m_f} \tag{5.3}$$

where α is the fraction reacted representing the conversion of the reactant to products, Eq. 5.3, $\Re$ is the universal gas constant, T is the absolute temperature, and m_i, m_0, and m_f the instantaneous, initial, and final masses of the sample, respectively.

The differential isoconversional method used to solve Eq. 5.2 and determine the kinetic parameters was the one proposed by Friedman [44], Eq. 5.4. For each given value of α in the range of 0.05-0.95, with steps of 0.05, three different heating rates, $\beta = dT/dt$, were used to construct plots of $\ln(\beta d\alpha/dT)$ against $1/T$. The values of E and $ln(A)$ were determined from the linear regression coefficients of each plot.

$$\ln\left(\frac{d\alpha}{dt}\right) = \ln\left(\beta\frac{d\alpha}{dT}\right) = \ln\left[Af(\alpha)\right] - \frac{E}{\Re T} \tag{5.4}$$

When integrated, Eq. 5.2 leads to Eq. 5.5, where $g(\alpha)$ is the integral form of the reaction model. This integral does not have an analytical solution, and the approach proposed by Starink [45], Eq. 5.6, can be used for the solution with great accuracy. By plotting the left-hand side against $1/T$, the kinetic parameters were calculated from the slope of the straight lines fitted at each given value of α.

$$g(\alpha) \equiv \int_0^{\alpha} \frac{d\alpha}{f(\alpha)} = \frac{A}{\beta}\int_0^{T} exp\left(-\frac{E}{\Re T}\right) dT \tag{5.5}$$

$$\ln\left(\frac{\beta}{T^{1.92}}\right) = const - 1.0008\left(\frac{E}{\Re T}\right) \tag{5.6}$$

Although the essence of isoconversional methods allows determining the activation energy without assuming a reaction model, the conversion dependence of the process rate obeys some model [46]. This dependence can be represented by a wide variety of theoretical functions, Table 5.2 [42, 46, 47], and the Criado method [48, 49], Eq. 5.7, is a quite straightforward way to determine the most appropriate model.

$$\left(\frac{T}{T_{0.5}}\right)^2 \frac{(d\alpha/dt)}{(d\alpha/dt)_{0.5}} = \frac{f(\alpha)\, g(\alpha)}{f(0.5)\, g(0.5)} \tag{5.7}$$

The terms $T_{0.5}$, $(d\alpha/dt)_{0.5}$, $f(0.5)$, and $g(0.5)$ in Eq. 5.7 represent the temperature, the reaction rate and the conversion functions evaluated at $\alpha = 0.5$. The most suitable reaction model was defined by the best match between the experimental and theoretical plots of the reaction rate vs. the fraction reacted. This assessment was performed with the Root Mean Square Error (RMSE) assistance, Eq. 5.8.

Table 5.2: Algebraic expressions of the most widely used theoretical solid-state reaction models.

Model	Code	$f(\alpha)$	$g(\alpha)$
Power-law	P_n^a	$n\alpha^{(n-1/n)}$	$\alpha^{(1/n)}$
Zero-order	$F0$	1	α
First-order	$F1$	$1-\alpha$	$-ln(1-\alpha)$
Second-order	$F2$	$(1-\alpha)^2$	$[1/(1-\alpha)]-1$
Third-order	$F3$	$(1-\alpha)^3$	$[1/(1-\alpha)^2]-1$
Avrami-Erofeev	A_n^b	$n(1-\alpha)[-ln(1-\alpha)]^{1-1/n}$	$[-ln(1-\alpha)]^{1/n}$
Contracting geometry	R_n^c	$n(1-\alpha)^{1-1/n}$	$1-(1-\alpha)^{1/n}$
One-dimensional diffusion	$D1$	$(1/2)\alpha^{-1}$	α^2
Two-dimensional diffusion	$D2$	$[-ln(1-\alpha)]^{-1}$	$(1-\alpha)ln(1-\alpha)+\alpha$
Three-dimensional diffusion	$D3$	$(3/2)(1-\alpha)^{2/3}[1-(1-\alpha)^{1/3}]^{-1}$	$[1-(1-\alpha)^{1/3}]^2$
Ginstling-Brounshtein	$D4$	$(3/2)[(1-\alpha)^{-1/3}-1]^{-1}$	$1-(2\alpha/3)-(1-\alpha)^{2/3}$
Prout-Tompkins	$B1$	$\alpha(1-\alpha)$	$ln[\alpha/(1-\alpha)]$
Exponential-law	$E1$	α	$ln(\alpha)$

$^a n = 2/3, 2, 3, 4$ / $^b n = 2, 3, 4$ / $^c n = 2, 3$

$$RMSE = \sqrt{\frac{\sum_{i=1}^{n} \left[(d\alpha/dt)_{exp} - (d\alpha/dt)_{model}\right]^2}{n}} \tag{5.8}$$

A multi-step kinetics analysis was performed in accordance with the ICTAC Kinetics Committee recommendations [43] considering that the WRPE pyrolysis products decomposition consists of a reaction with competing steps. The model-fitting approach was also chosen here for this investigation considering each reaction step i with its own conversion α_i, reaction rate $d\alpha_i/dt$, activation energy E_i, pre-exponential factor A_i, and reaction model $f_i(\alpha_i)$ [50]. The overall conversion and reaction rate in the multi-step model was represented by Eq. 5.9 and Eq. 5.10:

$$\alpha = \sum_{i=1}^{n} w_i \alpha_i \tag{5.9}$$

$$\frac{d\alpha}{dt} = \sum_{i=1}^{n} w_i \frac{d\alpha_i}{dt} = \sum_{i=1}^{n} w_i A_i exp\left(-\frac{E_i}{\Re T}\right) f_i(\alpha_i) \tag{5.10}$$

where w_i represents the contribution of each partial mass loss to the overall conversion ($\sum w_i = 1$ and $\sum \alpha_i = \alpha$) and n the number of steps. Taking the logarithmic derivative of the global reaction rate (Eq. 5.10) and noting that, according to the isoconversional principle, the reaction rate at a constant value of α is only a function of temperature, the isoconversional activation energy can be calculated as follows [51]:

$$E_\alpha = \frac{\sum_{i=1}^{n} w_i E_i k_i f_i(\alpha_i)}{\sum_{i=1}^{n} w_i k_i f_i(\alpha_i)} \tag{5.11}$$

5.3 Results and discussion

5.3.1 Hydrocarbons products yield

Once proposed a new pyrolysis reactor model, the C-DPyR, several experiments were carried out to understand and control the process in question. Although occurring in different chambers, two phenomena coexist with heat interaction within the reactor: the carbonaceous medium's combustion and the plastic waste's pyrolysis. Each one with a specific purpose, the first serving as a source of thermal energy and the second aiming to reduce volume while recovering a energy-dense product.

Table 5.1 summarizes the experimental results detailing the heat inputs - according to the discussion around the longitudinal temperature profiles (LTP) presented in Chapter 3 and the energy availability analysis presented in Chapter 4 -, and the pyrolysis products yields, and Fig. 5.3 shows the WRPE's pyrolysis product yields organized by experiment and categorized into two classes of thermal energy (kJ) for establishing relative comparisons. The pyrolysis products yields of all experiments are available in Appendix H.

The amount of gas was high for the experiments that reached great thermal energies (Exp. 3, 4, 5, and 8), on average of 74 wt.% regardless of the reduction in thermal energy from 723 - 523 kJ in these experiments. This confirmed that the heat available to pyrolysis (even considering the thermal losses) was more than sufficient, making the gas yield insensitive to thermal energy changes; see Chapter 4 for further details. However, decreasing the thermal energy beyond the limit of 497 kJ (Exp. 10), a perceptible change of the product yield distribution was observed. The gas decreased to around 60 wt.%, increasing the amount of wax, from 14 wt.% to about 34 wt.%. The experiment that reached 497 kJ of thermal energy marked the transition from, that we considered, high to intermediate-low thermal energy experiments, from 447 - 77 kJ. At these energies, the wax amount significantly increased to an average of 55 wt.%, and a maximum of about 87 wt.% of wax was recovered from an experiment that made available 80 kJ of energy (Exp. 17). Also, the experimental conditions leading to an attractive amount of wax recovered were reached if one keeps in mind converting plastics toward an energy-dense material, easily recoverable, and using low-grade fuels as a heat-drive.

Note that, the gas yields, as it was obtained by difference, it is in somehow overestimated. Although the C-DPyR makes the plastic conversion sustainably into gas, the actual fraction of non-condensable gases depending on developing or installing a relatively sophisticated wash system [21, 24, 52], that was out of the scope of this work.

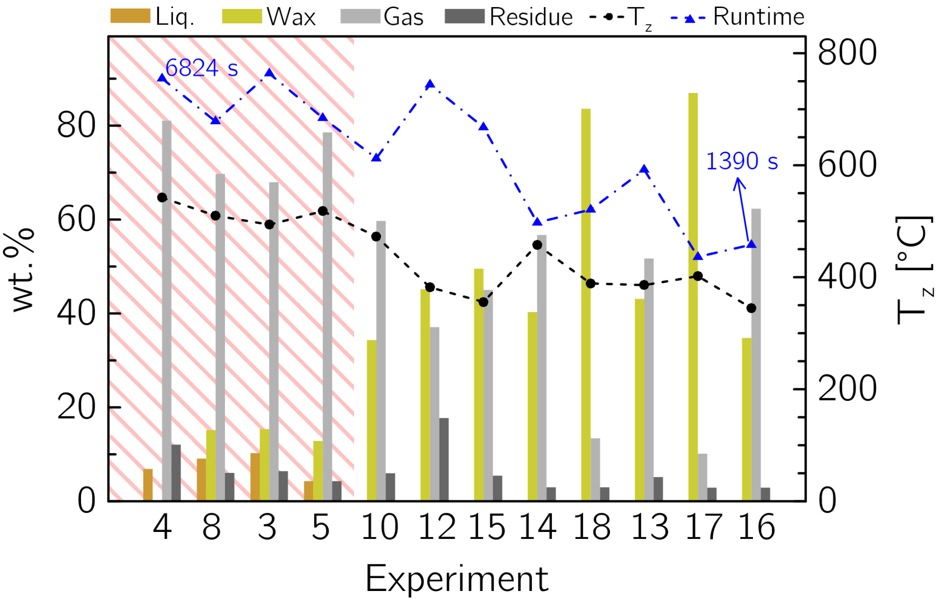

Figure 5.3: Pyrolysis product yields organized according to thermal energy grouped experiments. The hatched zone refers to the experiments that reached high thermal energy to pyrolyze the WRPE.

5.3.2 Polyethylene wax characterization

Once the experimental parameters that govern the C-DPyR were controlled to maximize wax products' recovery, some samples were selected to be characterized. For the sake of simplification, the adopted nomenclature for the characterized samples was as following, W_i refers to wax from experiment i related to the experiment number adopted through the text. Therefore, W_{13}, W_{15}, and W_{17} were chosen for characterization via TG/DSC and FTIR.

5.3.2.1 General aspects

The visual aspect of the wax recovered is shown in Figure 5.2. Although the samples before pyrolysis carry all kinds of pigmentation, the wax recovered had a yellowish aspect. At room temperature, the wax had a strong petrochemicals-like smell and a soft consistency to the touch. When in direct contact with fire, it behaved like paraffin wax.

5.3.2.2 Thermal analysis

TGA and DSC results under inert atmosphere are summarized in Fig. 5.4. In this figure, each column presents the decomposition profile of the waxes recovered from the experiments W_{13}, W_{15}, and W_{17}. The heating rate of 15 °C/min was used for these samples; however, for sample W_{17}, two additional heating rates were applied for kinetics purposes, 5 and 10 °C/min, meeting ICTAC's [42] recommendation of using at least three different temperature programs.

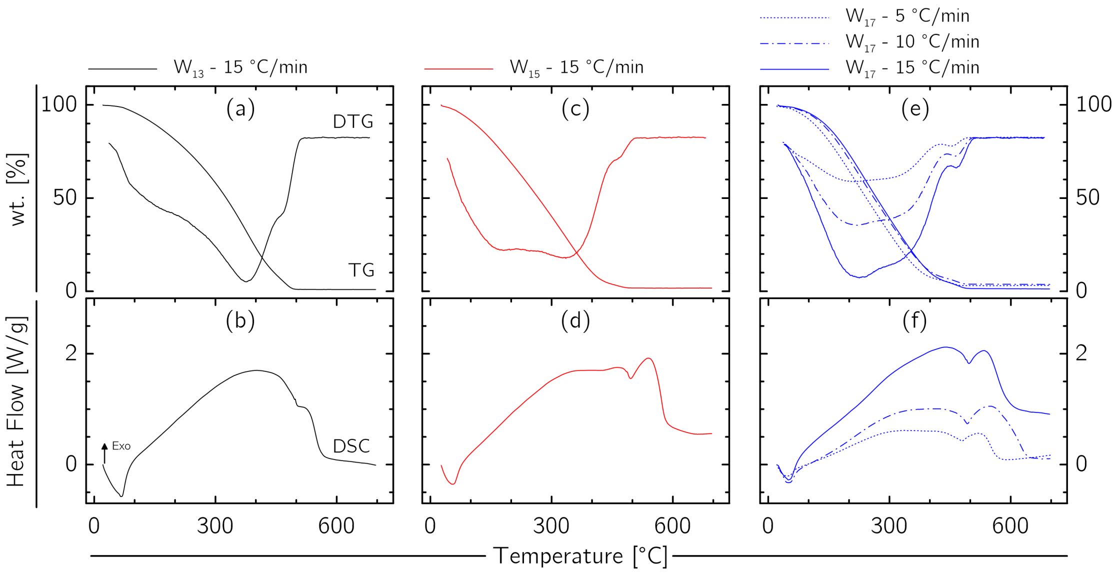

Figure 5.4: Waxes thermal analysis under an inert atmosphere. At the top the thermogravimetric analysis and its derivatives, and at the bottom the differential scanning calorimetry.

When subjected to pyrolysis, all wax samples were almost wholly converted between 25-500 °C, on average 98 wt.% of the mass was lost. Once the heating starts, the conversion begins and occurs without notable plateaus, indicating a single-step degradation. Nevertheless, when plotted the DTG curves, at least three reactions can be observed, suggesting a principal reaction competing with two others. These reactions with some overlapping degrees might be associated with the main functional groups forming the wax. Note that, as the condition of heat at the origin of the recovering process changed for W_{13}, W_{15}, and W_{17}, the reaction rate, expressed by DTG curves, changed accordingly. Also, observing the variation of the heating rate from 5 to 15 °C/min, the rate of the reaction is amplified sensibly as well.

Different zones on the TGA curves were defined assisted by its first and second derivatives [33]. The initial and final reaction temperature, T_{range}, and their respective percentage of mass converted, Δ_m, are indicated in Table 5.3. By confronting the TG/DTG curves for W_{13}, W_{15}, and W_{17} samples, a first reaction started at 25 °C and extended to 250 °C, converting approximately 42 wt.% of the sample. Then, the second reaction begins, and until approximately 400 °C, the mass converted is an additional of 42 wt.%. The last reaction converted the rest of the sample mass up to 500 °C. Since all samples followed this thermal behavior, it suggests that the material recovered kept consistent regardless of the thermal process originating it.

The heat flow [W/g], as a function of the temperature, is shown in Figures Fig. 5.4 b, d, and f. The enthalpies obtained from the integration of the DSC curves are shown in Table 5.3. All curves were normalized to the instantaneous sample mass.

In the DSC curves, approximately two temperature regions can be distinguished. The heat effect is endothermic in the low-temperature range (25-90 °C). This endothermic enthalpy is associated with the heat absorbed by the wax for phase change (melting and evaporation) and the beginning of the decomposition, i.e., a competition between Intra- and intermolecular bond breaking. In the second region, from 90 to 600 °C or more, the heat effects are exothermic, quite big, and well defined. It cannot be attributed without wild speculations. Although we are dealing with polyethylene samples, the ultimate composition is C and H [33]. However, the fact of the samples be recycled from municipal solid waste, C and H account for around 98 wt.% of the total mass, remaining 2 wt.% of other elements among which oxygen. Further discussions are still necessary, such as confronting these results with another technique as of FTIR.

Therefore, a significant part of the heat effects involved in polyethylene wax pyrolysis is exothermic. On the one hand, the average endothermic peak contributed to the overall heat flow; $\Delta H_{endo} = 80$ J/g; on the other, average exothermic heat was quite significant, $\Delta H_{exo} = 2115$ J/g. Since the literature is most of the time concerned by investigating just the behavior of wax melting [32, 53], to establish a comparison between the wax characteristics obtained from the C-DPyR process and others is not a trivial task. It is somehow understandable since the wax recovered here becomes, to the recycling stream point of view, a raw material that can be employed diversely [54, 55, 56], and consequently, the characterization technique explored is particular of the end-use, thus, scarce data.

5.3.2.3 FTIR spectra

FTIR was performed to investigate the functional groups present in the condensed pyrolysis products. The spectra related to samples W_{13}, W_{15}, and W_{17} were plotted in Fig. 5.5. The band indicated in the wavenumber of 2915 cm^{-1} was related to the asymmetric stretching of the C-H bonds; around the wavenumber of 2845 cm^{-1}, there was a

Table 5.3: Combustion conditions and TGA parameters.

Sample	β [°C/min]	m_i [mg]	ΔH_{endo} J/g	ΔH_{exo} J/g	T_{range} [°C]	Δ_m [wt.%]
W_{13}	15	16.5	106.5	1846.6	25 - 200	18.8
					200 - 450	72.3
					450 - 500	8.0
					25 - 500	99.0
W_{15}	15	15.1	61.3	2069.5	25 - 235	40.8
					235 - 430	53.9
					430 - 500	3.6
					25 - 500	98.3
W_{17}	5	15.5	68.3	2415.3	25 - 260	54.8
					260 - 430	38.2
					430 - 500	2.8
					25 - 500	95.8
W_{17}	10	16.3	62.0	2268.9	25 - 270	52.7
					270 - 445	40.4
					445 - 500	3.0
					25 - 500	96.0
W_{17}	15	15.0	66.0	1973.1	25 - 300	60.9
					300 - 450	34.5
					450 - 500	3.2
					25 - 500	98.5

band correlated to the symmetric stretching of C-H bonds out-of-plane [35]. A band of weak intensity was detected in the range of 2370 - 2300 cm^{-1}; this band was associated with symmetric stretching of CO_2 gas in-plane. Its presence in the spectrum was due to the equipment calibration process and the atmosphere saturation for carrying out the analyses [57].

In the range, 1467 - 1462 cm^{-1}, a band formation intrinsic to CH_2 group angular deformation was verified. Around 1377 cm^{-1} was detected that a CH_3 band underwent symmetric angular deformation [58]. At 903 cm^{-1}, an ambiguous band was detected, which could mean both a monosubstituted aromatic ring stretching or a C-H bond torsional angular deformation [59]. However, the nature of the material allows us to conclude that such a band effectively refers to the C-H bond's angular deformation since LDPE does not present aromatic compounds in its polymeric structure [58]. Finally, the bands between 730 and 717 cm^{-1} refer to CH_2 group rotational angular deformation [60].

The developed analyses showed that the samples presented C-H groups (symmetrical and asymmetric), CH_2 with angular deformation, CH_3 with symmetric angular deformation, and CH_2 with angular rotational deformation, in their respective wavenumbers. These groups were precisely those present in the FTIR spectra of LDPE, as described

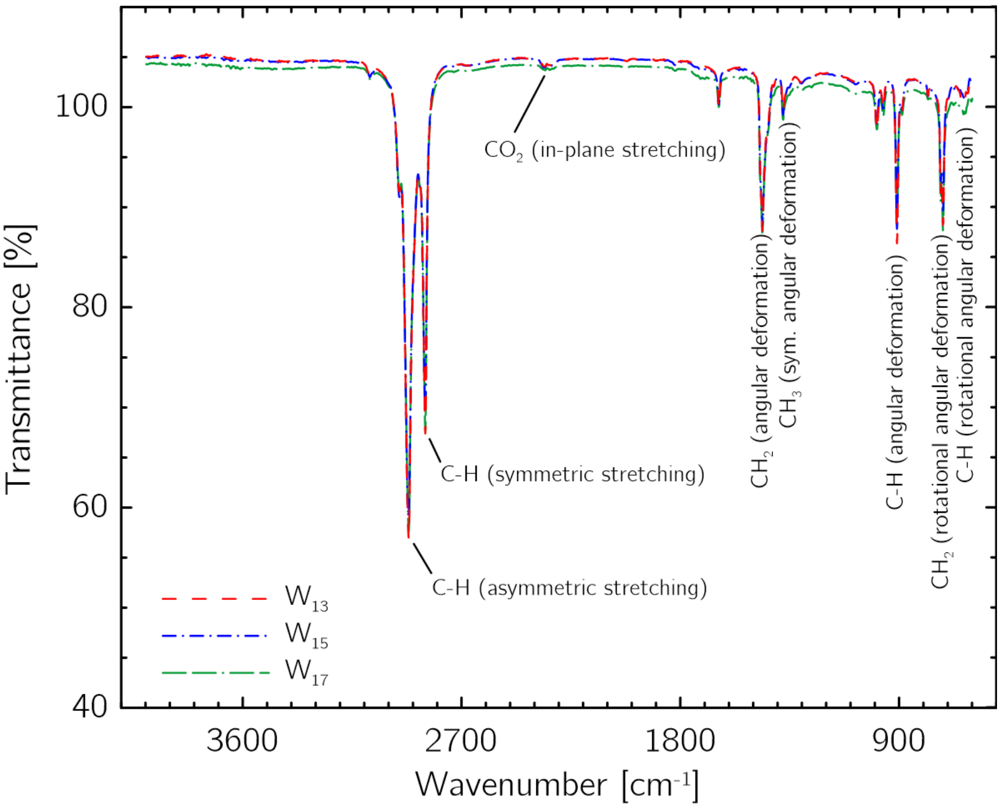

Figure 5.5: FTIR spectra.

previously in [35, 58, 60]. Therefore, the samples can be categorized as a low-density polyethylene type since the spectra found in the literature and samples were quite identical. Therefore, the samples W_{13}, W_{15}, and W_{17} are indeed polyethylene wax type [29].

5.3.3 Kinetic analysis

The visual inspection of TGA curves suggested that the degradation of the waxes occurring in a single step. Conversely, the DTG evidenced the existence of at least three competing reactions in the temperature range investigated. In these concerns, the literature highlights that a process that includes more than one step does not immediately invalidate applying a single-step approach [43, 51]. Considering these arguments, it was performed both single-step and multi-step kinetics of the wax pyrolysis.

The TGA data of wax W_{17} was used for kinetics investigation, and two isoconversional methods were applied to evaluate the experimental data within the range $\alpha =$ 0.05 - 0.95. Once the integral methods can give rise to a systematic error when E varies significantly with α [42], the differential approach was also employed to avoid this type of error in the kinetic triplet evaluation. The calculated kinetic parameters were used to reconstruct the conversion profiles in comparison with the experimental ones.

5.3.3.1 Single-step kinetics

Considering the thermal degradation of W_{17} occurring as a single-step reaction, the plots of the left-hand side of Eq. 5.4 and Eq. 5.6 against 1/T, Fig. 5.6a and 5.6b, respectively, resulted in straight lines with R^2 presenting small fluctuations around 0.997 for $0.1 \leq \alpha \leq 0.9$, indicating an acceptable linear confidentiality of the plots [39]. Each straight line corresponds to a given value of fraction reacted and is obtained by the fit of three points, each corresponding to a heating rate. From the coefficients of these lines, the activation energy was determined and then reported in a plot E vs. α, Fig. 5.7a and Fig. 5.7d. For both methods used, an important dependence of E on α was observed. The average activation energy varies in a range of 96 ± 18 kJ/mol for the Friedman method, and 87 ± 19 kJ/mol for the Starink method, and the difference between the maximum and minimum value of E was 88% and 79% of the average value, for each method respectively.

The most suitable reaction models, $f(\alpha)$, able to describe the conversion process of the wax recovered from the WRPE pyrolysis are shown in Fig. 5.8, all the theoretical functions in Table 5.2 were tested, and only the best fits are plotted. The RMSE calculation between the experimental data and the theoretical reaction models, Eq. 5.8,

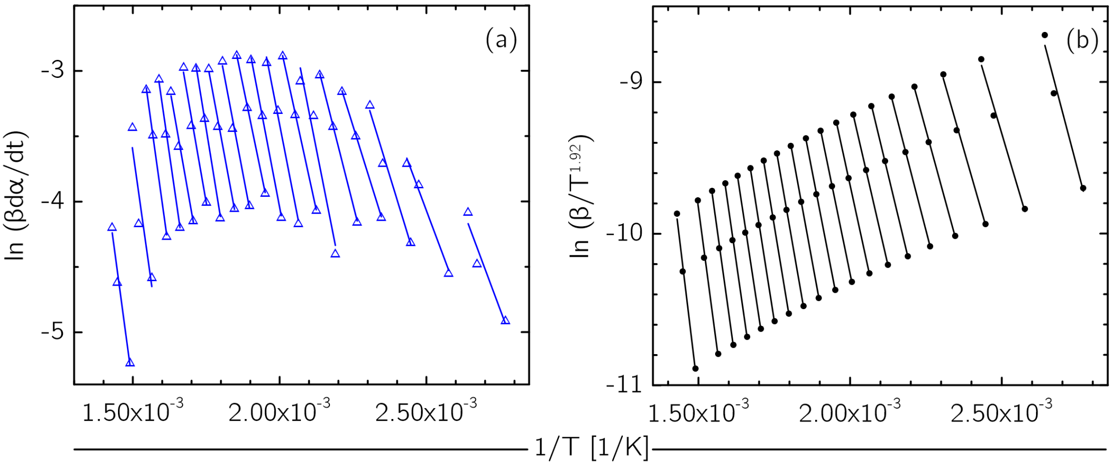

Figure 5.6: Single-step kinetics. (a) Isoconversional plot of Friedman and (b) Starink methods.

resulted in the same scenario described in Chapter 2 [33], the process could be described by Avrami-Erofeev models (A2, A3, and A4), first-order model (F1), as well as, by the contracting geometry (R3) and three-dimensional diffusion (D3) models. It must be stressed that a single dependence on α can be observed practically independent of the heating rate [42, 48].

Once the activation energy was calculated, and the reaction model identified, to complete the kinetic triplet, the pre-exponential factor was calculated according to Eq. 5.2. The dependence of $ln(A)$ on α for Friedman and Starink are shown in Fig. 5.7b and Fig. 5.7e, respectively. Table 5.4 displays the values of E and $ln(A)$ for the entire conversion range and Fig. 5.7c,f shows the relationship between them. For the Friedman method, the correlation coefficient was $R^2 = 0.901$, and for the Starink method, it was $R^2 = 0.991$, indicating that for all heating rates, the values of A accord with the E within all the conversion range, despite the amplification of the experimental noises inherent of the differential method used.

The kinetic triplets calculated were used to reconstruct numerically the fraction reacted profiles in comparison with the experimental TGA data that were used to evaluate these parameters. Fig. 5.9a-c shows this comparison for when single-step kinetics was considered, the average correlation coefficients was $R^2 = 0.990$ and $R^2 = 0.998$ for Friedman and Starink methods, respectively, pointing a good consistency of the kinetic parameters estimates. Therefore, since the thermal degradation process of the wax seems to include more than one step according to DTG and, the application of the single-step approach seems to be enough to approximate the TGA curves, the overall rate of the process probably is dominated or limited by the rate of one step [43].

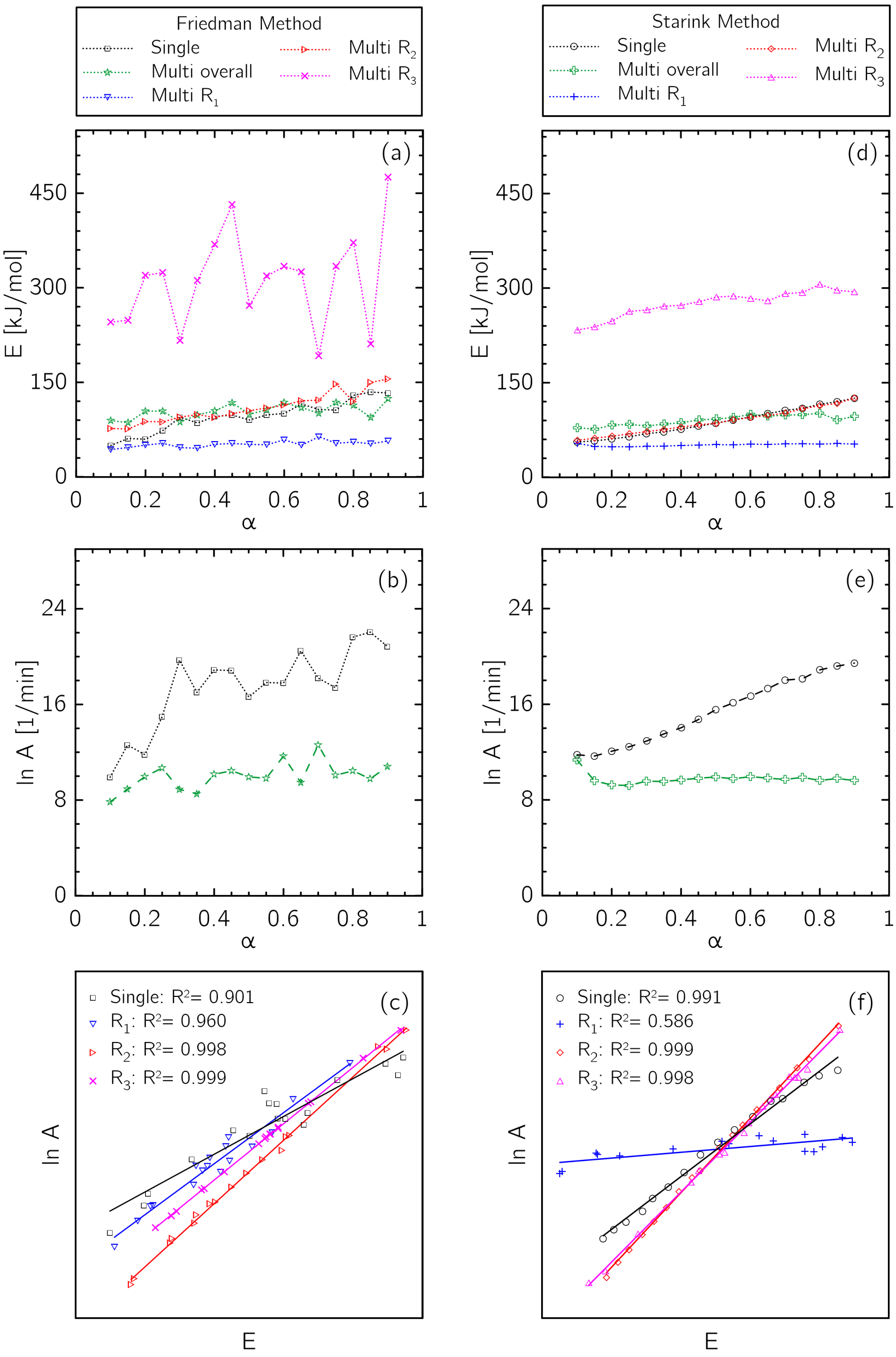

Figure 5.7: Single-step and multi-step kinetics: Dependence of activation energy on α, the dependence of pre-exponential factor on α, and estimated $ln(A)$ vs. E. (a)-(c) for Friedman method, and (d)-(f) for Starink method.

Table 5.4: Activation energy, E [kJ/mol], and pre-exponential factor, A [1/min], for the pyrolysis of the wax recovered from WRPE, obtained from isoconversional methods in a range of $\alpha = 0.05$ - 0.95, using single-step and multi-step approaches.

	Single step				Multi step			
α	Friedman method		Starink method		Friedman method		Starink method	
	E [kJ/mol]	$ln(A)$ [1/min]	E [kJ/mol]	$ln(A)$ [1/min]	E [kJ/mol]	$ln(A)$ [1/min]	E [kJ/mol]	$ln(A)$ [1/min]
0.05	50.1	10.7	63.0	15.0	91.4	24.3	82.2	21.3
0.10	49.9	9.9	55.9	11.8	89.5	21.9	78.5	18.6
0.15	60.9	12.6	57.6	11.8	85.8	19.8	76.2	17.1
0.20	59.8	11.8	60.7	12.1	104.4	24.1	82.6	18.1
0.25	73.6	15.0	64.2	12.6	104.2	23.1	83.9	17.7
0.30	94.6	19.7	69.0	13.2	87.0	17.8	81.2	16.3
0.35	85.6	17.0	71.9	13.6	98.4	20.2	84.3	16.7
0.40	95.8	18.9	76.4	14.2	104.7	21.0	86.4	16.6
0.45	98.0	18.8	81.0	14.8	117.5	23.4	91.0	17.2
0.50	90.3	16.6	85.7	15.6	99.5	18.7	92.5	17.1
0.55	98.4	17.8	90.7	16.1	106.5	19.6	94.8	17.0
0.60	100.6	17.8	95.5	16.7	117.7	21.5	99.9	17.6
0.65	115.6	20.5	100.8	17.4	110.0	19.3	96.8	16.5
0.70	106.9	18.2	106.0	18.0	100.8	16.9	98.6	16.5
0.75	105.9	17.4	109.4	18.1	118.2	19.9	99.0	16.0
0.80	129.4	21.6	115.6	18.9	113.4	18.5	101.7	16.2
0.85	134.5	22.0	119.9	19.3	94.1	14.4	90.9	13.8
0.90	133.1	20.8	125.3	19.4	124.2	19.2	96.6	14.1
0.95	139.3	20.6	137.6	20.3	110.1	15.5	88.3	11.7

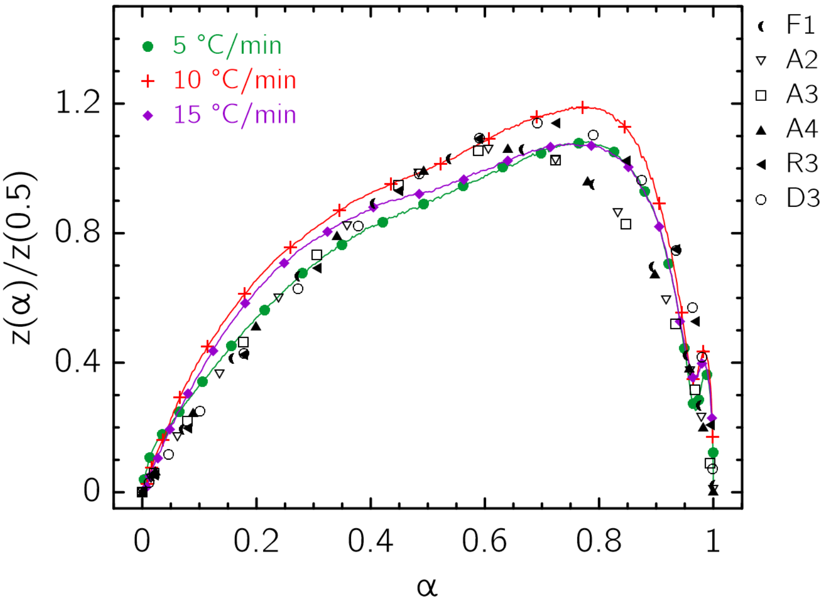

Figure 5.8: Masterplots of theoretical reaction models vs. experimental data.

5.3.3.2 Multi-step kinetics

As discussed above in section 5.3.2.2, the DTG curves indicated the presence of at least three competing reactions. It was assumed that each reaction step, R_1, R_2, and R_3, refers to a functional group indicated in the FTIR and has its own kinetic parameters. The kinetic analysis took place considering the approach of each step individually but connected through a multi-step kinetic model. From the isoconversional plots shown in Fig. 5.10, the activation energy for each reaction was calculated as previously presented, while for the overall reaction, linking the individual steps, Eq. 5.11 was used.

Fig. 5.7a,d shows the dependence of E on α for each individual reaction step, as well as, for the overall reaction. The activation energy for R_1 that starts at 25 °C and extends approximately to 250 °C, was around 52 kJ/mol, for R_2 that goes up to 400 °C was around 89 kJ/mol, and for R_3 that goes up to 500 °C around 275 kJ/mol. The overall activation energy hovered around 104 ± 8 kJ/mol when Friedman method was used and around 90 ± 6 kJ/mol for Starink method.

It should be stressed that the meaningful kinetics parameters predicted by the single-step kinetics can be explained at this point. When compared with the activation energy of the individual reactions, the single-step activation energy is almost equal to the values obtained for reaction R_2, responsible for a large mass loss, on the other hand, the values obtained for R_3 have little influence in the overall reaction due to its insignificant

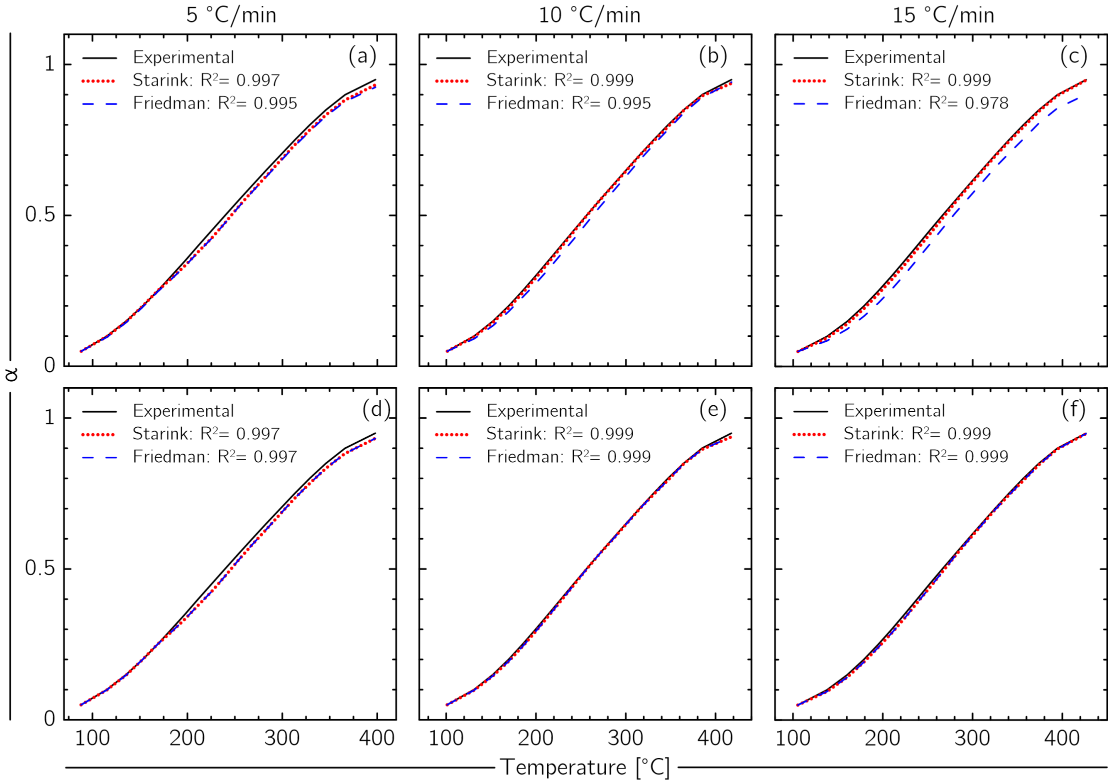

Figure 5.9: (a)-(c) Reconstruction of thermogravimetric analysis considering the pyrolysis of the recovered products as a single-step reaction, and (d)-(f) considering a multi-step reaction.

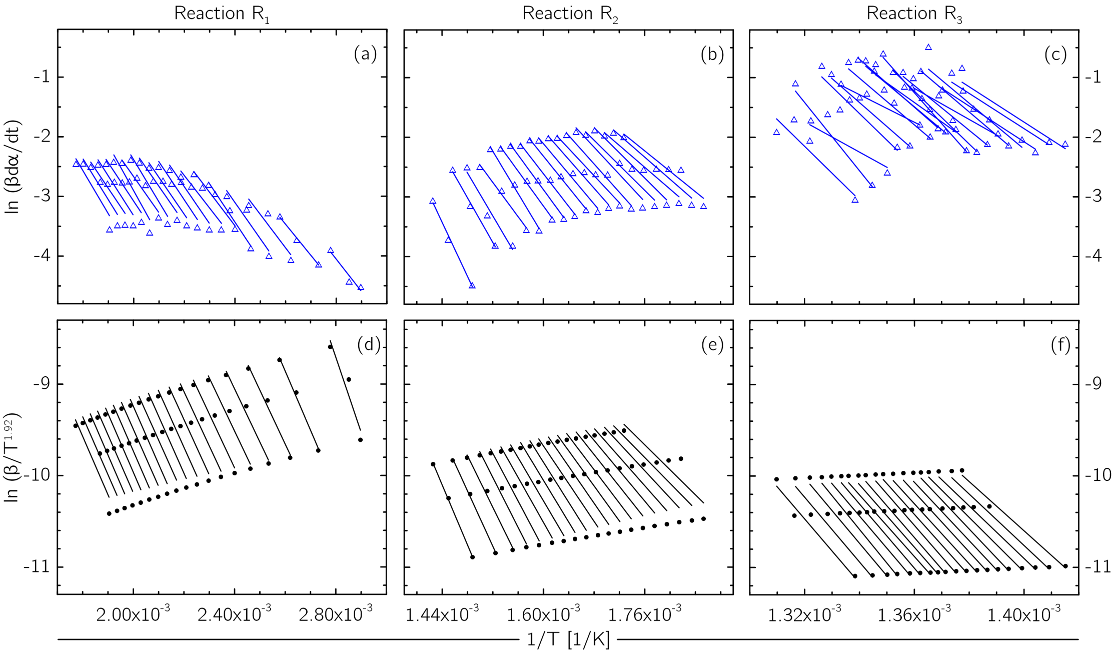

Figure 5.10: Multi-step kinetics. (a)-(c) Isoconversional plot of Friedman, and (d)-(e) Starink methods.

participation in the mass loss, supporting the idea of a dominant reaction.

The pre exponential factor was also calculated and its dependence on α is represented in the Fig. 5.7b,e. Table 5.4 summarizes the values of E and $ln(A)$ within the entire conversion range for the multi-step kinetics.

Fig. 5.9d-f shows a comparison between measurements and predictions of TGA curves, indicating that the kinetic triplets predictions from the multi-step approach can be used to reconstruct accurately TGA curves, $\mathrm{R}^2 = 0.999$. Confirming that, by dividing the overall reaction into three steps with its individual extent of conversion, i.e, by performing the analysis in small temperature intervals, the accuracy of the isoconversional approach is improved, making reliable kinetic predictions [51].

5.4 Conclusion

In this article, waste of recycled polyethylene was pyrolyzed and hydrocarbons products recovered and characterized. A new concept of energetically self-sustaining pyrolysis reactor was launched for this purpose. Inside C-DPyR low-grade fuels were oxidized and used as a heat-drive to promote the plastic waste's pyrolysis. The interplay between heat input and pyrolysis yields was investigated by managing the experimental configurations aiming to reduce the PE waste volume while recovering an energy-dense product. Pyrolysis performed under the condition of high thermal energy available to convert the WRPE, between 723-523 kJ, results mainly in gases, an average of 74 wt.%. While intermediate-low thermal energy experiments have maximized wax production. The wax yield significantly increased when the energy available decreased to the level of 80 kJ, leading to the optimal recovery condition producing 87 wt.% of wax.

TGA under an inert atmosphere indicated that the recovered wax is almost completely converted between 25-500 °C and suggests a decomposition reaction with at least three competing steps. DSC evidenced an endothermic zone of phase change associated with decomposition, with an average enthalpy of 80 J/g, and a more significant exothermic zone of decomposition with an average enthalpy of 2115 J/g. From FTIR it was established the functional groups of the wax yield, it is composed mainly of C-H, CH_2, and CH_3, the same groups present in the FTIR spectra of LDPE.

Single-step kinetics identified an important dependence of E on α, but at the same time, proved to be an accurate and economical description of the wax degradation that, can be represented by the models of Avrami-Erofeev (A2, A3, and A4), first-order (F1), contracting geometry (R3), and three-dimensional diffusion (D3). By performing multi-step kinetics, overall activation energy around 90-104 kJ/mol was found, and TGA curves were accurately reconstructed, confirming a reliable kinetic prediction.

Bibliography

[1] Stephanie L. Wright and Frank J. Kelly. Plastic and Human Health: A Micro Issue? *Environmental Science & Technology*, 51(12):6634–6647, jun 2017.

[2] Luís Gabriel Antão Barboza, A. Dick Vethaak, Beatriz R.B.O. Lavorante, Anne-Katrine Lundebye, and Lúcia Guilhermino. Marine microplastic debris: An emerging issue for food security, food safety and human health. *Marine Pollution Bulletin*, 133:336 – 348, 2018.

[3] Cayla R. Cook and Rolf U. Halden. Chapter 20 - ecological and health issues of plastic waste. In Trevor M. Letcher, editor, *Plastic Waste and Recycling*, pages 513 – 527. Academic Press, 2020.

[4] Riley E.J. Schnurr, Vanessa Alboiu, Meenakshi Chaudhary, Roan A. Corbett, Meaghan E. Quanz, Karthikeshwar Sankar, Harveer S. Srain, Venukasan Thavarajah, Dirk Xanthos, and Tony R. Walker. Reducing marine pollution from single-use plastics (sups): A review. *Marine Pollution Bulletin*, 137:157 – 171, 2018.

[5] Ana L. Patrício Silva, Joana C. Prata, Tony R. Walker, Diana Campos, Armando C. Duarte, Amadeu M.V.M. Soares, Damià Barcelò, and Teresa Rocha-Santos. Rethinking and optimising plastic waste management under covid-19 pandemic: Policy solutions based on redesign and reduction of single-use plastics and personal protective equipment. *Science of The Total Environment*, 742:140565, 2020.

[6] Tanveer M. Adyel. Accumulation of plastic waste during covid-19. *Science*, 369(6509):1314–1315, 2020.

[7] José G.B Derraik. The pollution of the marine environment by plastic debris: a review. *Marine Pollution Bulletin*, 44(9):842 – 852, 2002.

[8] Dirk Xanthos and Tony R. Walker. International policies to reduce plastic marine pollution from single-use plastics (plastic bags and microbeads): A review. *Marine Pollution Bulletin*, 118(1):17 – 26, 2017.

[9] Su Shiung Lam and Howard A Chase. A review on waste to energy processes using microwave pyrolysis. *Energies*, 5(10):4209–4232, 2012.

[10] Veena Sahajwalla and Vaibhav Gaikwad. The present and future of e-waste plastics recycling. *Current Opinion in Green and Sustainable Chemistry*, 13:102–107, 2018.

[11] Alicia Lee and Mei Shan Liew. Tertiary recycling of plastics waste: an analysis of feedstock, chemical and biological degradation methods. *Journal of Material Cycles and Waste Management*, sep 2020.

[12] Stephen J Miller, Naresh Shah, and Gerald P Huffman. Conversion of waste plastic to lubricating base oil. *Energy & fuels*, 19(4):1580–1586, 2005.

[13] Eoin Butler, Ger Devlin, and Kevin McDonnell. Waste polyolefins to liquid fuels via pyrolysis: review of commercial state-of-the-art and recent laboratory research. *Waste and biomass valorization*, 2(3):227–255, 2011.

[14] W Kaminsky, M Predel, and A Sadiki. Feedstock recycling of polymers by pyrolysis in a fluidised bed. *Polymer Degradation and Stability*, 85(3):1045 – 1050, 2004. The 42nd IUPAC Microsymposium on Degradation, Stabilisation and Recycling of Polymers, and The 2nd International Conference on Modification, Degradation and Stabilisation of polymers (MoDeSt).

[15] S.M. Al-Salem, A. Antelava, A. Constantinou, G. Manos, and A. Dutta. A review on thermal and catalytic pyrolysis of plastic solid waste (psw). *Journal of Environmental Management*, 197:177 – 198, 2017.

[16] Muhammad Saad Qureshi, Anja Oasmaa, Hanna Pihkola, Ivan Deviatkin, Anna Tenhunen, Juha Mannila, Hannu Minkkinen, Maija Pohjakallio, and Jutta Laine-Ylijoki. Pyrolysis of plastic waste: Opportunities and challenges. *Journal of Analytical and Applied Pyrolysis*, page 104804, 2020.

[17] C Roy, A Chaala, and H Darmstadt. The vacuum pyrolysis of used tires: End-uses for oil and carbon black products. *Journal of analytical and applied pyrolysis*, 51(1-2):201–221, 1999.

[18] DP Serrano, J Aguado, JM Escola, and E Garagorri. Conversion of low density polyethylene into petrochemical feedstocks using a continuous screw kiln reactor. *Journal of Analytical and Applied Pyrolysis*, 58:789–801, 2001.

[19] Paola Lettieri and Sultan M. Al-Salem. Chapter 17 - thermochemical treatment of plastic solid waste. In Trevor M. Letcher and Daniel A. Vallero, editors, *Waste*, pages 233 – 242. Academic Press, Boston, 2011.

[20] R Miandad, MA Barakat, Asad S Aburiazaiza, M Rehan, IMI Ismail, and AS Nizami. Effect of plastic waste types on pyrolysis liquid oil. *International biodeterioration & biodegradation*, 119:239–252, 2017.

[21] Devy K. Ratnasari, Mohamad A. Nahil, and Paul T. Williams. Catalytic pyrolysis of waste plastics using staged catalysis for production of gasoline range hydrocarbon oils. *Journal of Analytical and Applied Pyrolysis*, 124:631 – 637, 2017.

[22] Ioannis Kalargaris, Guohong Tian, and Sai Gu. Experimental evaluation of a diesel engine fuelled by pyrolysis oils produced from low-density polyethylene and ethylene–vinyl acetate plastics. *Fuel Processing Technology*, 161:125 – 131, 2017.

[23] Yayun Zhang, Dengle Duan, Hanwu Lei, Elmar Villota, and Roger Ruan. Jet fuel production from waste plastics via catalytic pyrolysis with activated carbons. *Applied Energy*, 251:113337, 2019.

[24] Stanislav Honus, Shogo Kumagai, Gabriel Fedorko, Vieroslav Molnár, and Toshiaki Yoshioka. Pyrolysis gases produced from individual and mixed pe, pp, ps, pvc, and pet—part i: Production and physical properties. *Fuel*, 221:346 – 360, 2018.

[25] John Scheirs and Walter Kaminsky, editors. *Feedstock Recycling and Pyrolysis of Waste Plastics.* John Wiley & Sons, Ltd, Chichester, UK, mar 2006.

[26] Hartmut Luker. Polyethylene wax, and a process for the preparation thereof, June 11 1991. US Patent 5,023,388.

[27] MA AlMaadeed, Sami Labidi, Igor Krupa, and Mabrouk Ouederni. Effect of waste wax and chain structure on the mechanical and physical properties of polyethylene. *Arabian Journal of Chemistry*, 8(3):388–399, 2015.

[28] Michael J D'amato, Santiago Faucher, Timothy L Lincoln, Ali Darabi, and Rosa Duque. Method for obtaining wax from recycled polyethylene, December 1 2015. US Patent 9,200,130.

[29] Douglas L Dorset. *Crystallography of the polymethylene chain: an inquiry into the structure of waxes*, volume 17. Oxford University Press on Demand, 2005.

[30] Sergei N. Magonov, Natalya A. Yerina, Goran Ungar, Darrell H. Reneker, and Dimitri A. Ivanov. Chain Unfolding in Single Crystals of Ultralong Alkane C 390 H 782 and Polyethylene: An Atomic Force Microscopy Study. *Macromolecules*, 36(15):5637–5649, jul 2003.

[31] J.A. Molefi, A.S. Luyt, and I. Krupa. Comparison of ldpe, lldpe and hdpe as matrices for phase change materials based on a soft fischer–tropsch paraffin wax. *Thermochimica Acta*, 500(1):88 – 92, 2010.

[32] I. Krupa, G. Miková, and A.S. Luyt. Phase change materials based on low-density polyethylene/paraffin wax blends. *European Polymer Journal*, 43(11):4695 – 4705, 2007.

[33] João Vitor F Duque, Márcio F Martins, Gérald Debenest, and Marcos Tadeu D'Azeredo Orlando. The influence of the recycling stress history on ldpe waste pyrolysis. *Polymer Testing*, page 106460, 2020.

[34] PASR Wickramarachchi. *Vibrational spectroscopy of linear and branched long alkanes.* PhD thesis, Sheffield Hallam University,, 2006.

[35] J.V Gulmine, P.R Janissek, H.M Heise, and L Akcelrud. Polyethylene characterization by ftir. *Polymer Testing*, 21(5):557 – 563, 2002.

[36] Ruth Chércoles Asensio, Margarita San Andrés Moya, José Manuel de la Roja, and Marisa Gómez. Analytical characterization of polymers used in conservation and restoration by ATR-FTIR spectroscopy. *Analytical and Bioanalytical Chemistry*, 395(7):2081–2096, dec 2009.

[37] HS Mpanza and AS Luyt. Comparison of different waxes as processing agents for low-density polyethylene. *Polymer Testing*, 25(4):436–442, 2006.

[38] J.K. Akishino, D.P. Cerqueira, G.C. Silva, V. Swinka-Filho, and M. Munaro. Morphological and thermal evaluation of blends of polyethylene wax and paraffin. *Thermochimica Acta*, 626:9 – 12, 2016.

[39] Sergey Vyazovkin, Konstantinos Chrissafis, Maria Laura Di Lorenzo, Nobuyoshi Koga, Michèle Pijolat, Bertrand Roduit, Nicolas Sbirrazzuoli, and Joan Josep Suñol. Ictac kinetics committee recommendations for collecting experimental thermal analysis data for kinetic computations. *Thermochimica Acta*, 590:1 – 23, 2014.

[40] Marcin Wojdyr. Fityk : a general-purpose peak fitting program. *Journal of Applied Crystallography*, 43(5):1126–1128, oct 2010.

[41] P J Linstrom and W G Mallard, editors. *NIST Chemistry WebBook, NIST Standard Reference Database Number 69.* National Institute of Standards and Technology, Gaithersburg MD, 20899, 2005.

[42] Sergey Vyazovkin, Alan K. Burnham, José M. Criado, Luis A. Pérez-Maqueda, Crisan Popescu, and Nicolas Sbirrazzuoli. ICTAC Kinetics Committee recommendations for performing kinetic computations on thermal analysis data. *Thermochimica Acta*, 520(1-2):1–19, 2011.

[43] Sergey Vyazovkin, Alan K. Burnham, Loic Favergeon, Nobuyoshi Koga, Elena Moukhina, Luis A. Pérez-Maqueda, and Nicolas Sbirrazzuoli. Ictac kinetics committee recommendations for analysis of multi-step kinetics. *Thermochimica Acta*, 689:178597, 2020.

[44] Henry L. Friedman. Kinetics of thermal degradation of char-forming plastics from thermogravimetry. Application to a phenolic plastic. *Journal of Polymer Science Part C: Polymer Symposia*, 6(1):183–195, mar 1964.

[45] M.J Starink. The determination of activation energy from linear heating rate experiments: a comparison of the accuracy of isoconversion methods. *Thermochimica Acta*, 404(1-2):163–176, sep 2003.

[46] Michael E. Brown, editor. *Introduction to Thermal Analysis*, volume 1 of *Hot Topics in Thermal Analysis and Calorimetry.* Kluwer Academic Publishers, Dordrecht, 2004.

[47] John P. Elder. Reconciliation of Arrhenius and iso-conversional analysis kinetics parameters of non-isothermal data. *Thermochimica Acta*, 272:41–48, jan 1996.

[48] J.M. Criado. Kinetic analysis of DTG data from master curves. *Thermochimica Acta*, 24(1):186–189, may 1978.

[49] Pedro E. Sánchez-Jiménez, Luis A. Pérez-Maqueda, Antonio Perejón, and José M. Criado. Generalized master plots as a straightforward approach for determining the kinetic model: The case of cellulose pyrolysis. *Thermochimica Acta*, 552:54–59, jan 2013.

[50] Elena Moukhina. Determination of kinetic mechanisms for reactions measured with thermoanalytical instruments. *Journal of Thermal Analysis and Calorimetry*, 109(3):1203–1214, sep 2012.

[51] Sergey Vyazovkin. Chapter 4 - modern isoconversional kinetics: From misconceptions to advances. In Sergey Vyazovkin, Nobuyoshi Koga, and Christoph Schick, editors, *Recent Advances, Techniques and Applications*, volume 6 of *Handbook of Thermal Analysis and Calorimetry*, pages 131 – 172. Elsevier Science B.V., 2018.

[52] Jan Nisar, Ghulam Ali, Afzal Shah, Munawar Iqbal, Rafaqat Ali Khan, Sirajuddin, Farooq Anwar, Raqeeb Ullah, and Mohammad Salim Akhter. Fuel production from waste polystyrene via pyrolysis: Kinetics and products distribution. *Waste Management*, 88:236 – 247, 2019.

[53] Wiesława Ciesińska, Barbara Liszyńska, and Janusz Zieliński. Selected thermal properties of polyethylene waxes. *Journal of Thermal Analysis and Calorimetry*, 125(3):1439–1443, 2016.

[54] M Predel and W Kaminsky. Pyrolysis of mixed polyolefins in a fluidised-bed reactor and on a pyro-gc/ms to yield aliphatic waxes. *Polymer Degradation and Stability*, 70(3):373 – 385, 2000.

[55] M. Arabiourrutia, G. Elordi, G. Lopez, E. Borsella, J. Bilbao, and M. Olazar. Characterization of the waxes obtained by the pyrolysis of polyolefin plastics in a conical spouted bed reactor. *Journal of Analytical and Applied Pyrolysis*, 94:230 – 237, 2012.

[56] Rohit Kumar Singh, Biswajit Ruj, A.K. Sadhukhan, and P. Gupta. Impact of fast and slow pyrolysis on the degradation of mixed plastic waste: Product yield analysis and their characterization. *Journal of the Energy Institute*, 92(6):1647 – 1657, 2019.

[57] Ray L. Frost and Kristy L. Erickson. Vibrational spectroscopy of stichtite. *Spectrochimica Acta Part A: Molecular and Biomolecular Spectroscopy*, 60(13):3001 – 3005, 2004.

[58] Melissa R. Jung, F. David Horgen, Sara V. Orski, Viviana Rodriguez C., Kathryn L. Beers, George H. Balazs, T. Todd Jones, Thierry M. Work, Kayla C. Brignac, Sarah-Jeanne Royer, K. David Hyrenbach, Brenda A. Jensen, and Jennifer M. Lynch. Validation of atr ft-ir to identify polymers of plastic marine debris, including those ingested by marine organisms. *Marine Pollution Bulletin*, 127:704 – 716, 2018.

[59] Merve Sogancioglu, Esra Yel, and Gulnare Ahmetli. Pyrolysis of waste high density polyethylene (hdpe) and low density polyethylene (ldpe) plastics and production of epoxy composites with their pyrolysis chars. *Journal of Cleaner Production*, 165:369 – 381, 2017.

[60] Daniel José da Silva and Hélio Wiebeck. Using pls, ipls and sipls linear regressions to determine the composition of ldpe/hdpe blends: A comparison between confocal raman and atr-ftir spectroscopies. *Vibrational Spectroscopy*, 92:259 – 266, 2017.

Chapter 6

Conclusion

This work aimed to develop a self-sustainable energy device that uses low-grade fuels as heat-drive to pyrolysis, perform the polyethylene waste thermal cracking, and recover an energy-dense material. This included characterizing the polyethylene waste; launching and commissioning a new concept of energetically self-sustaining pyrolysis reactor in which the input energy is driven by combustion; description and investigation of the propagation of a smoldering front in annular section pathway; and finally, conducting experiments toward the production and recovering of an energy-dense pyrolysis product in the form of wax.

- Regarding the characterization of the PE wastes, the main conclusion is that the thermal and mechanical stress history experienced by the waste during the recycling process promotes changes in the structure of the material, favoring long carbon chains and weakening the boundaries among the compounds. The ultimate and proximate analysis established that PE waste was mainly composed of carbon and hydrogen, forming a volatile matter matrix. Consequently, the TGA under an inert atmosphere resulted in an almost total mass loss in a single step between 350-500 °C. However, before degradation, the DSC evidenced that the PE is heated to the melting point; then, the bonds linking the compounds forming the PE are thermally broken. From this stage onward, a series-parallel pyrolysis reaction occurs.
- Concerning the composition of the waste of recycled PE, the XRD pointed out that the crystalline phase was formed by n-Tricosane ($C_{23}H_{48}$), n-nonacosane ($C_{29}H_{60}$), and n-tetracontane ($C_{40}H_{82}$), and also, from the analysis of the diffraction patterns, it was concluded that these long carbon chains are formed during the recycling. It must be considered to propose a pyrolysis pathway. These composition changes were evidenced by kinetics that identified that recycled waste needs less activation energy than other samples to degrade thermally.
- A series-parallel pyrolysis pathway represented the PE thermal cracking, including the stages of preheating, melting, bond breaking, evaporation, and pyrolysis reaction.

- Once the material to be pyrolyzed was characterized, an original combustion-driven reactor was designed, built, and tested as a novel experimental device capable of performing pyrolysis of condensed phase matters. A positive energy balance was reached, ratifying that a self-sustaining combustion process carried enough energy to supply a pyrolysis process. Particular attention was paid to propose a representative longitudinal temperature profile based on the time-averaged method at each thermocouple position, demonstrating that the use of the peak temperature to establish a representative LTP overestimates the results.

- The experiments' reliability was tested under twenty-nine runs, which presented a few average deviations, and through dimensionless analysis that led to empirical correlations that govern the C-DPyR. A sensitivity analysis of the experimental parameters, inlet air velocity, and bed composition was carried out based on the variance ANOVA F-test which revealed the independence of these input parameters on defining the longitudinal temperature profile.

- The main aspects of smoldering front propagation in an annular section were presented and new contributions in the calculation of the front velocity, as well as, in the determination of the basic structure of the combustion front base on the use of the concept of equivalence ratio (ER) to determine the smoldering front propagation regime were made.

- It was demonstrated that all experiments were self-sustaining, and the temperature evolution curves showed a similar behavior compared with the classical smoldering experiments in non-annular volumes. A mass balance was performed, and it was evidenced by the ER results and the high levels of CO and H_2 in the flue gas that the combustion front propagated under a gasification regime. The thermal and chemical fronts velocities verified that the oxidation reaction's heat was mostly convected downstream of the reaction front in the homogeneous and heterogeneous beds. That helped increase the average longitudinal temperature in both scenarios analyzed, increasing the airflow rate and increasing the bed heterogeneities by stimulating endothermic reactions.

- Finally, waste of recycled polyethylene was pyrolyzed, using low-grade fuels as a heat-driven, and hydrocarbons products were recovered and characterized. From the investigation of the interplay between heat input and pyrolysis yields, it was concluded that conversion performed under the condition of high thermal energy available, between 723-523 kJ, results mainly in gases, an average of 74 wt.%. While intermediate-low thermal energy experiments have maximized wax production. The wax yield significantly increased when the energy available decreased to 80 kJ, leading to the optimal recovery condition producing 87 wt.% of wax. The average enthalpy of the recovered products hovered around 2115 J/g, and according to FTIR results, the wax's functional groups were C-H, CH_2, and CH_3, the same groups present in the FTIR spectra of LDPE. The wax pyrolysis kinetic parameters were determined for a single and multi-step chemical reaction.

Therefore, the operational conditions attained by C-DPyR were proof to recover a polyethylene wax in an energetically self-sustaining way using low-grade fuels as heat-drive with the potential of performing feedstock recycling of plastic waste.

Conclusion (Fr)

Ce travail visait à développer un dispositif énergétique de pyrolyse autonome qui utilise des combustibles de faible qualité comme moteur thermique. Ainsi il est possible de craquer thermiquement des déchets de polyéthylène et de récupèrer un matériau dense en énergie. Cela comprenait aussi la caractérisation des déchets de polyéthylène et la mise en service d'un nouveau concept de réacteur de pyrolyse autonome sur le plan énergétique dans lequel l'énergie d'entrée est entraînée par un processus de combustion. Ensuite, nous avons décrit et étudié la propagation d'un front de combustion dans le réacteur annulaire. Enfin nous avons mené des expériences en vue de la production et de la récupération d'un produit de pyrolyse dense en énergie sous forme de cire.

- En ce qui concerne la caractérisation des déchets de PE, la principale conclusion est que l'historique des contraintes thermiques et mécaniques subies par les déchets pendant le processus de recyclage favorise des changements dans la structure du matériau, privilégiant les longues chaînes de carbone en affaiblissant les liens entre les composés. L'analyse ultime et immédiate a établi que les déchets de PE étaient principalement composés de carbone et d'hydrogène, formant une matrice de matière volatile. Par conséquent, le TGA sous atmosphère inerte a entraîné une perte de masse presque totale en une seule étape entre 350 et 500 °C. Cependant, avant dégradation, l'analyse DSC a mis en évidence que le PE est chauffé jusqu'à son point de fusion; puis, les liaisons liant les composés formant le PE sont rompues thermiquement. A partir de cet état, une suite de réactions de pyrolyse série et parallèle se produit;

- Concernant la composition des déchets de PE recyclé, la XRD a souligné que la phase cristalline était formée par le n-Tricosane ($C_{23}H_{48}$), le n-nonacosane ($C_{29}H_{60}$), et le n-tétracontane ($C_{40}H_{82}$). A partir de l'analyse des diagrammes de diffraction, il a été conclu que ces longues chaînes de carbone se formaient lors du recyclage. Ces changements de composition ont été mis en évidence par la découverte d'une cinétique propre qui a été identifiée. Il en résultet aussi que les déchets recyclés ont besoin de moins d'énergie d'activation que d'autres échantillons pour se dégrader thermiquement;

- Une voie de pyrolyse en série parallèle représentait le craquage thermique du PE, y compris les étapes de préchauffage, de fusion, de rupture de liaison, d'évaporation et de réaction de pyrolyse;

- Une fois le matériau à pyrolyser caractérisé, un réacteur de combustion entièrement nouveau a été conçu, construit et testé. Il apparaît comme un nouveau dispositif expérimental capable d'effectuer la pyrolyse des matières en phase condensée. Un bilan énergétique positif a été atteint, confirmant qu'un processus de combustion autoentretenu transportait suffisamment d'énergie pour alimenter le processus de pyrolyse de nos déchets plastiques. Une attention particulière a été portée afin de proposer un profil de température longitudinal représentatif basé sur la méthode de la moyenne temporelle à chaque position des thermocouples, démontrant ainsi que l'utilisation de la température de pointe pour établir une PLT représentative surestime les résultats;

- La fiabilité des expériences a été testée sous vingt-neuf essais, qui ont présenté quelques écarts moyens, et par une analyse sans dimension qui a conduit à des corrélations empiriques qui régissent le C-DPyR. Une analyse de sensibilité des paramètres expérimentaux, de la vitesse de l'air d'admission et de la composition du lit a été réalisée sur la base du test de variance ANOVA F-test qui a révélé l'indépendance de ces paramètres d'entrée quant à la définition du profil de température longitudinal;

- Les principaux aspects de la propagation du front de combustion dans une section annulaire ont été présentés et de nouvelles contributions dans le calcul de la vitesse du front, ainsi que, dans la détermination de la structure de base de la base du front de combustion sur l'utilisation du concept de rapport d'équivalence (ER) pour déterminer le régime de propagation du front de combustion couvant ont été faites;

- Il a été démontré que toutes les expériences étaient autoentretenues, et les courbes d'évolution de température ont montré un comportement similaire par rapport aux expériences classiques de combustion lente dans des volumes non annulaires. Un bilan de masse a été réalisé, et il a été mis en évidence par les résultats du RE et les niveaux élevés de CO et H_2 dans les gaz de combustion que le front de combustion se propageait dans un régime de gazéification. Les vitesses des fronts thermique et chimique ont démontré que la chaleur de la réaction d'oxydation était principalement transportée en aval du front de réaction dans des lits homogènes et/ou hétérogènes. Cela nous permetd'augmenter la température longitudinale moyenne dans les deux scénarios analysés, en augmentant le débit d'air et augmentant les hétérogénéités du lit en stimulant les réactions endothermiques;

- Enfin, les déchets de polyéthylène recyclé ont été pyrolysés, en utilisant des combustibles de faible qualité comme moteur thermique. Lees produits d'hydrocarbures ont été récupérés et caractérisés. De l'étude de l'interaction entre l'apport de chaleur et les rendements de pyrolyse, il a été conclu que la conversion effectuée dans des conditions d'énergie thermique élevée disponible, entre 723-523 kJ, se traduit principalement par une production importante de gaz, $\approx 74\%$ du poids total produit. Par contre, les expériences à énergie thermique intermédiaire-basse ont maximisé la production de cire. Le rendement en cire augmentait considérablement lorsque l'énergie disponible diminuait à 80 kJ, conduisant à une condition de récupération optimale produisant 87% en poids total en cire. L'enthalpie moyenne des produits récupérés oscille autour de 2115 J/g, et selon les résultats FTIR, les groupes fonctionnels de la cire sont C-H, CH_2 et CH_3, les mêmes groupes présents dans les spectres FTIR du LDPE. Les paramètres cinétiques de la pyrolyse de la cire ont été déterminés pour une réaction chimique en une et plusieurs étapes.

Par conséquent, les conditions opérationnelles atteintes par le C-DPyR sont la preuve de la récupération d'une cire de polyéthylène d'une manière énergétiquement autonome en utilisant des combustibles de faible qualité comme moteur thermique avec le potentiel de recycler les matières premières issus des déchets plastiques.

Appendix A

License terms

The license term for Figures 1.3 and 1.4 can be checked at the links below:

`https://marketplace.copyright.com/rs-ui-web/mp/license/b5dcb9c5-e299-49d4-afea-5dfa1c0dff54/6e54f391-4e64-4693-8a4c-d384fb54bcba`

`https://s100.copyright.com/MyAccount/web/jsp/viewprintablelicensefrommyorders.jsp?ref=21e8f6c6-2940-43ae-bf49-bde3364d4d5f&email=`

Appendix B

Biodegradable masterbatch blends: The implications on thermal conversion and recycling stream of polyethylene

B.1 Introduction

During the past two decades, significant advances have been made in the development of biodegradable polymeric materials for many applications such as in packaging and hygiene products [1, 2]. Still, they accumulate in the environment as these materials are not readily biodegradable and because of their resistance to microbial degradation [3]. Among the many classes of polymers, are the blend of conventional plastic with different commercial biodegradable masterbatches [4, 5] and the compostable plastics fully derived from renewable agricultural resources [6]. The blends intend to confer suitable performance during service life and short degradation times during subsequent disposal, and the compostables are supposed to break down to basic elemental components with the aid of microorganisms.

If on the one hand, the biodegradable masterbatch can be blended with a wide range of polyolefin materials to tailor a product with properties perfectly matched to the application, on the other, they break the material recycling cycle since they actually only fragment the plastics. The fragmented plastics arises the migration, via rivers to the ocean, of the often called “micro-plastics” [7]. Also, some conventional masterbatch enters the market as a mixture (iron, stearate, oxides, etc.) to design a polymer labeled biodegradable as well and their fragments are spread on the environment. In this case report, we are dealing with the implications of blending fossil LDPE with biodegradable masterbatches on pyrolysis. Two types of commercial masterbatch are evaluated against a pure fossil LDPE.

B.2 Material and methods

The materials used were samples of Low-Density Polyethylene (LDPE), button type geometry with an average diameter of 4 mm, and two types of approximately equal length and radius cylindrical geometry masterbatches. All these samples are commercial and commonly used for the local manufacturers for making packaging. The first masterbatch is a blend of thermoplastic starch (66 wt.%) with LDPE (MB1). The second one is, so-called by the manufacturer, an environmentally friendly iron-based/oxo-biodegradable additive (MB2) in which the mixture proportions are not revealed. The LDPE has no pigmentation and the masterbatches are pigmented (see Fig. B.1).

The mutual physical properties provided in the materials data sheet are Melt Flow Rate (ASTM D1238) and Density (ASTM D792), 1.4 g /10 min and 0.921 g/cm^3 for LDPE, 1.2 g/10 min and 1.18 g/cm^3 for MB1, and 20-25 g/10min and 1.02 g/cm^3 for MB2, respectively.

The thermal degradation study was carried out by using thermogravimetric analysis (TGA). X-ray diffraction (XRD), ultimate and proximate analyses were applied to investigate if the samples could have a certain degree of differentiation either on composition and chemical structure arrangement. The full configuration of the experiments is detailed in Table B.1 [3].

Figure B.1: Geometric and color characteristics of samples. Made using a SteREO V12 Zeiss 0.63x FWD 107 mm.

B.3 Results

The LDPE sample is a high-quality polymer, its proximate and ultimate analysis indicated only the presence of carbon and hydrogen, 85.7 wt.% and 14.3 wt.% respectively. The blended sample (MB1) contains 57.2 wt.% of C, 9.8 wt.% of H, and 33.0 wt.% of other elements, in which 98.35 wt.% are volatile material. The environmental friendly masterbatch, MB2, has 83.24 wt.% of volatile material distributes in 63.6 wt.% of C, 9.6 wt.% of H, and 26.8 wt.% of other elements.

Table B.1: Setup of experiments for characterization of blending LDPE with masterbatches.

Name of experiment	Make	Operating conditions	Reference
TGA	STA 449F3 - NETZSCH	Sample mass: 10-15 mg Crucible: Al_2O_3 Carrier gas: N_2, Air, 60 ml/min Temperature range: 20-670 °C Heating rate, β: 20 °C/min	ISO 11358 DIN 51006
XRD	ULTIMA IV - RIGAKU	CuK alpha radiation: average length $\lambda = 0.15419$ Theta/2-theta Bragg-Brentano geometry 2-theta data range: 5.00° to 125.00° Step size: 0.02° CuK alpha doublet: wavelengths of 0.154056 (65%) and 0.154439 (35%) nm. Radiation detector: LiF monochromator	Duque et al. [3]
Ultimate analysis	EA 1110 - CE	Default settings	*ASTM D5373-16
Proximate analysis	Muffle furnace	Moisture and ash: Weight loss Volatile matter: **by difference	ASTM D3173 / D3173M-17a / D3174-12 -

* there is no specific standard for PE / ** based on the assumption that all the carbon and hydrogen, except for the moisture and ash contents, form the volatile matter matrix.

TGA and DTG results under inert and oxidative atmospheres are summarized in Fig. B.2. Under both atmospheres, the LDPE presents similar thermochemical behavior, one conversion step between 325 °C and 525 °C where the mass is totally converted. The supposed biodegradable sample, MB2, presented one conversion step between 375 °C and 525 ° leaving about 30 wt.% of an unconverted matter. Another reaction (inorganic one) has the potential to occur greater than 650 °C. The blended sample, MB1, has a more complex conversion chemical pathway. Under N_2 two main mass losses converting almost 97 wt.% of the total mass, and a third slow rate reaction starting about 500 °C are observed. Still for MB1, when undergoing oxidation, the two main blocks of compounds released in pyrolysis are oxidized. The first block can be approximated to one oxidation reaction step, and for the second block first occurs less strong oxidation that is partially covered by the main one. The last mass loss is observed starting as well as about 500 °C.

Fig. B.3 shows the X-ray powder diffraction patterns for all samples. The diffractograms of MB1 and MB2 showing the diffraction peaks characteristic of the orthorhombic cell of polyethylene are very similar to that of LDPE. This confirms the presence of the main compound forming the LDPE in the masterbatch samples. The essential difference of the observations is the amorphous wide peak, centered at around 19.5 degrees, which is not observed in the MB2 sample. Also, the MB2, according to the manufacture,

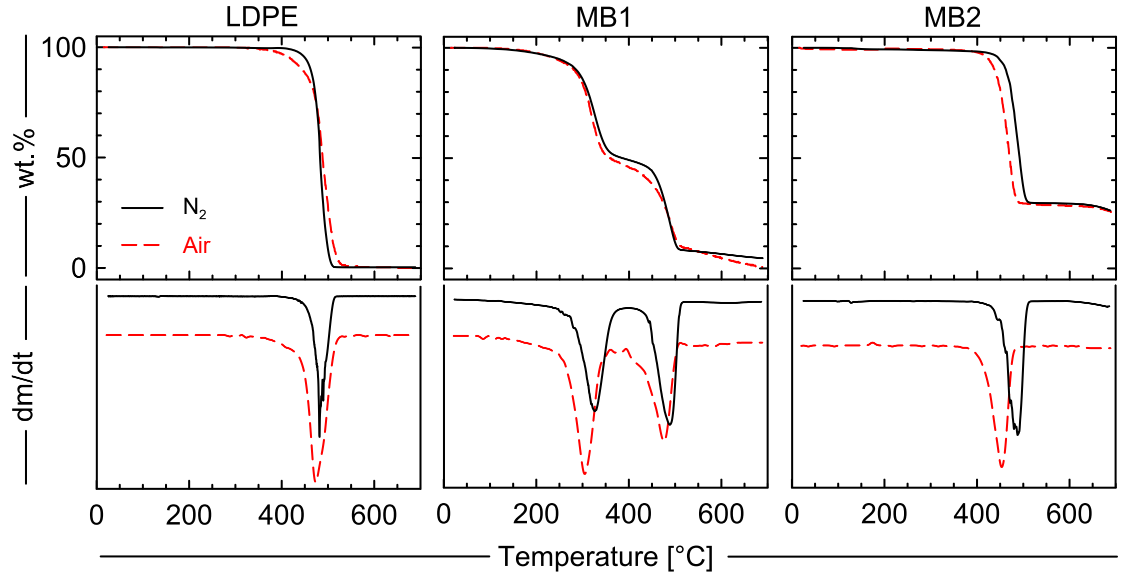

Figure B.2: TG and DTG analysis under N$_2$ and air.

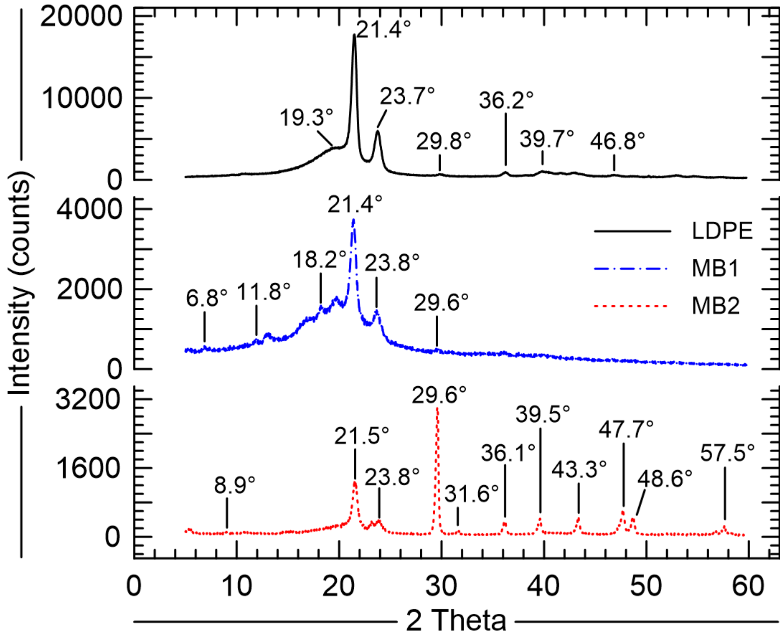

Figure B.3: X-ray powder diffraction pattern.

is an iron-based/oxo-biodegradable additive a strong peak centered at around 29 degrees and successive small ones are observed. The average crystallinity was 48% for LDPE. For the masterbatches, as they are blends, another methodology different from the used for pure LDPE should be applied to allow evaluating their degree of crystallinity.

The apparent relative reduction in the crystallinity for MB1 and MB2 may be explained on the basis of the proportion of LDPE in the blends, just 34 wt.% of LDPE in MB1, and for MB2, as shown in TG analysis, the proportion of the inorganic matter was important suggesting less than 1/3 in wt. basis of LDPE in MB2.

B.4 Final remarks

The former results reveal some implications. The ash content observed on proximate and TGA analysis is significant if we think the catalytic effect on the thermal conversion that such not converted components can promote at temperatures high as 700 °C. This is an important consideration since the samples, MB1 and MB2, are supposed to be used as a mixture with pure or recycled polyethylenes, and even if the MB2 should be mixed no more than 2 wt.% in the mixture. Note that, small quantities of some oxides in ash, or even ingredients widely used in masterbatch mixtures such as glycerol, sorbitol might have a catalytic effect on thermochemical conversion.

When compared with the LDPE pyrolysis, the conversion of the blend of thermoplastic starch and Polyethylene (MB1) happens in a wider temperature range, involving multi-step reactions, which suggest an increase in the overall pyrolysis enthalpy. In contrast, the pyrolysis of iron-based-oxo-biodegradable masterbatch (MB2) leaves behind a large amount of mass not converted material suggesting the presence of an important amount of inorganic material in its composition. Even though the blend of organic additives with fossil polyethylene might aid the biodegradability of plastics disposed of in the environment, some drawbacks should be accounted for the plastic life cycle: -the impact of this blends in the plastic recycling stream; - and the intensive use of agriculture for bioplastics manufacturing.

Looking ahead, if the main goal of this blends brings only plastic fragments, the process of collecting the debris becomes unviable breaking down the recycling cycle. Concerning, the intensive use of agriculture, even if this industry is toward the use of agriculture residues, it might induce competition with the biomass to energy industry.

Bibliography

[1] Nair, L. S. and Laurencin, C. T. *Biodegradable polymers as biomaterials.* Progress in polymer science, 32(8-9), 762-798, (2007).

[2] Laycock *et al.*. *Lifetime prediction of biodegradable polymers* Progress in Polymer Science, 71, 144-189, (2017).

[3] Duque *et al.*. *The influence of the recycling stress history on LDPE waste pyrolysis.* Polymer Testing (2020): 106460.

[4] Chen *et al.*. *Optimization of the preparation process of biodegradable masterbatches and characterization of their rheological and application properties.* Polymer Testing, 70, 526-532, (2018).

[5] Peres, A. M., Pires, R. R., Orefice, R. L. *Evaluation of the effect of reprocessing on the structure and properties of low density polyethylene/thermoplastic starch blends.* Carbohydrate polymers, 136, 210-215, (2016).

[6] Lorcks, J.. *Properties and applications of compostable starch-based plastic material.* Polymer degradation and stability 59.1-3 : 245-249, (1998).

[7] Haider *et al.*. *Plastics of the future? The impact of biodegradable polymers on the environment and on society.* Angewandte Chemie International Edition, 58(1), 50-62, (2019).

Appendix C

Relationship between dimensionless numbers

Buckingham Pi theorem was used to perform a simplified dimensional analysis of the combustion - driven pyrolysis reactor. The parameters annular distance, r, and the reactor's characteristic length, L, both in m, were used to represent the geometry of the reactor. To represent the physical properties of the bed were chosen the medium higher heating value, Q, in kJ/kg, the medium thermal conductivity, λ_m, in W/mK, the specific heat capacity at constant pressure, c_{p_m}, in J/kgK, and the bulking density, ρ_m, in kg/m^3. Finally, the inlet air velocity and temperature, v_a in m/s, and T_{in} in K, were considered as the input variable, respectively, while the longitudinal temperature, T_z in K, was arbitrated as the only output parameter. The dimensionless numbers obtained were

$$\Pi_1 = \frac{r}{L} \tag{C.1}$$

$$\Pi_2 = \frac{v_a}{Q^{0.5}} \tag{C.2}$$

$$\Pi_3 = \frac{T_z c_{p_m}}{Q} \tag{C.3}$$

$$\Pi_4 = \frac{\rho_m Q^{1.5} L}{T_z \lambda_m} \tag{C.4}$$

Combining equations C.1, C.2 and C.3, leads to

$$\Pi_1{}' = \frac{r v_a c_{p_m} T_z}{Q^{1.5} L} \tag{C.5}$$

By plotting $log(\Pi_1'^{\,-1})$ against $log(\Pi_2{}^{-1})$, Fig. C.1, straight lines for constant values of Π_3 and airflows are obtained. Solving the straight line equation for T_z, we have

$$log\left[\frac{Q^{1.5}L}{rv_a c_p T_z}\right] = m\left[log\left(\frac{Q^{0.5}}{v_a}\right)\right] + b$$

$$log\left(Q^{1.5}\right) - log\left(v_a\right) - log\left(T_z\right) = m\left[log\left(Q^{0.5}\right)\right] - m\left[log\left(v_a\right)\right] + b - log\left(\frac{L}{rc_p}\right)$$

$$log\left(T_z\right) = \sigma\left[log\left(Q\right)\right] + \omega\left[log\left(v_a\right)\right] - b + log\left(\frac{L}{rc_p}\right) \quad (\text{for } \sigma = 1.5 - 0.5m,\ \omega = m - 1)$$

$$log\left(T_z\right) = log\left(Q^{\sigma}v_a^{\omega}\right) + log\left(\frac{L}{rc_p}\right) - b$$

$$log\left(\frac{T_z}{Q^{\sigma}v_a^{\omega}}\right) = log\left(\frac{L}{rc_p}\right) - b$$

$$\frac{T_z}{Q^{\sigma}v_a^{\omega}} = C \quad (\text{for } C = 10^{log\left(\frac{L}{rc_p}\right) - b})$$

$$T_z = CQ^{\sigma}v_a^{\omega}$$

where m and b are the straight line coefficients, and C, σ, ω are the constants limited to the range of experimental inputs.

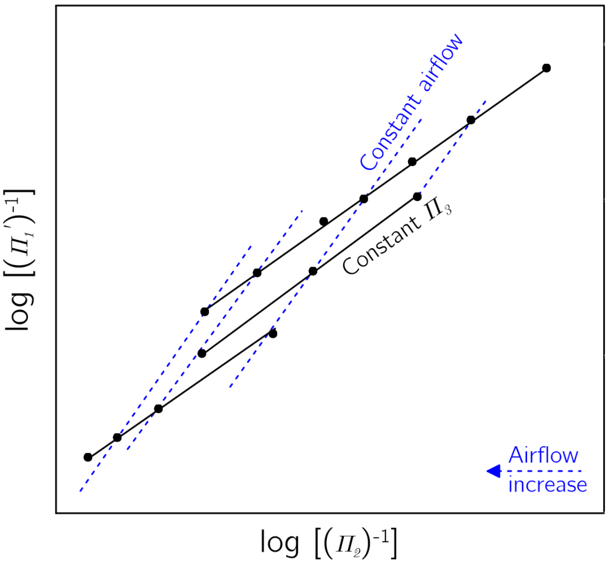

Figure C.1: Sketch Pi.

Appendix D

Supplementary experimental data

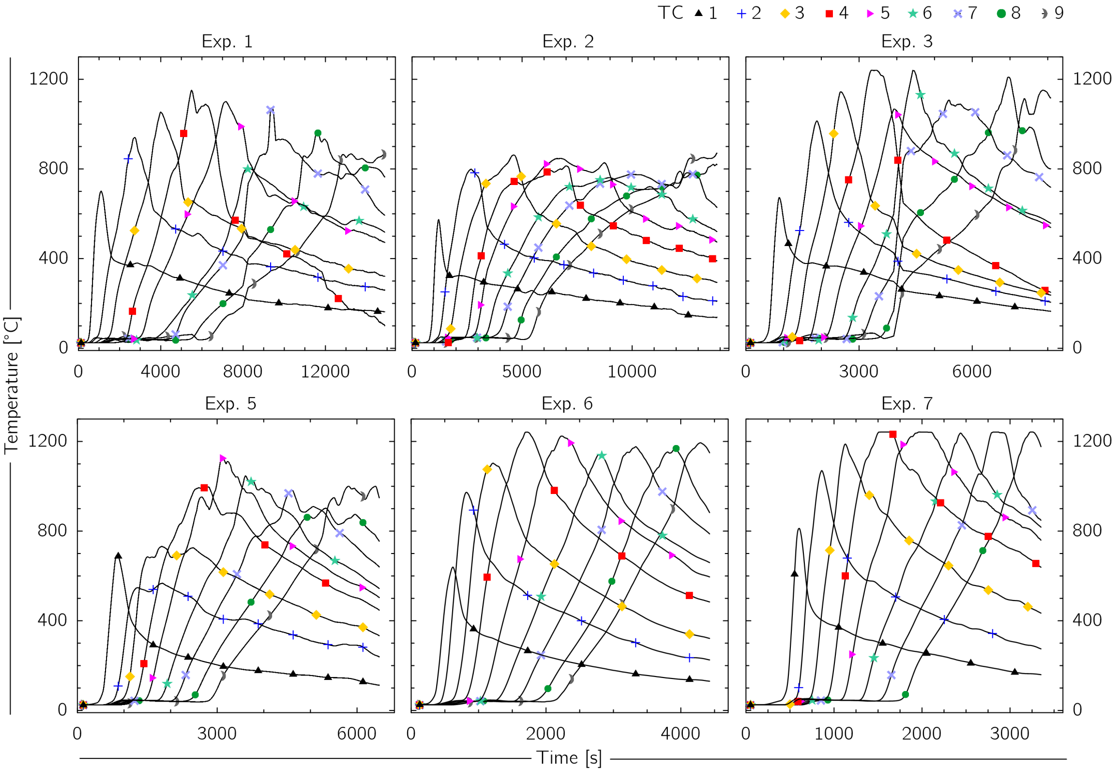

Figure D.1: Plot of temperature evolution for a annular section. Bed proximate analysis: 58.8 wt.% of FC, 28.4 wt.% of VM, 3.4 wt.% of MC, 9.4 wt.% of Ash, and 0 wt.% of IM.

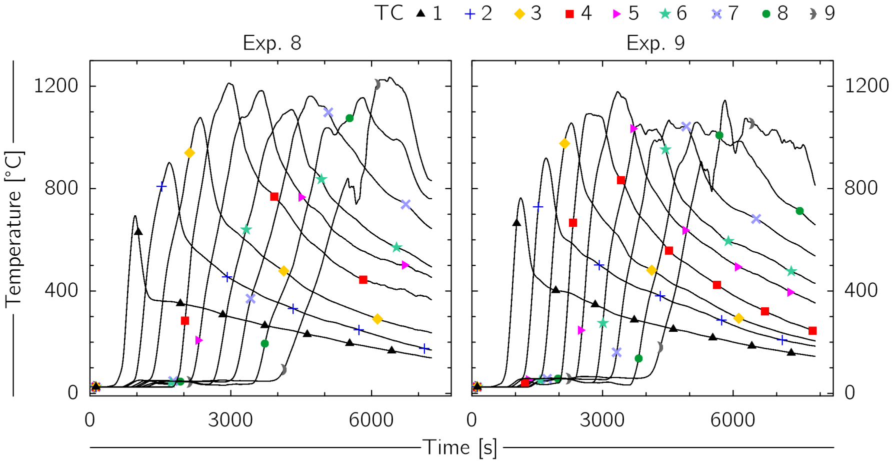

Figure D.2: Plot of temperature evolution for a annular section. Exp. 8 - Bed proximate analysis: 49.0 wt.% of FC, 23.7 wt.% of VM, 19.5 wt.% of MC, 7.8 wt.% of Ash, and 0 wt.% of IM. Exp. 9 - Bed proximate analysis: 42.0 wt.% of FC, 20.3 wt.% of VM, 31.0 wt.% of MC, 6.7 wt.% of Ash, and 0 wt.% of IM.

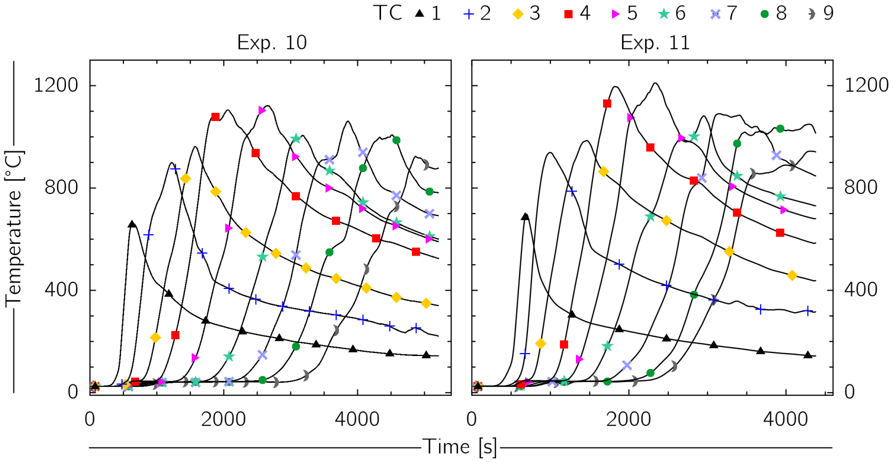

Figure D.3: Plot of temperature evolution for a annular section. Bed proximate analysis: 47.9 wt.% of FC, 22.7 wt.% of VM, 2.7 wt.% of MC, 7.5 wt.% of Ash, and 20.1 wt.% of IM.

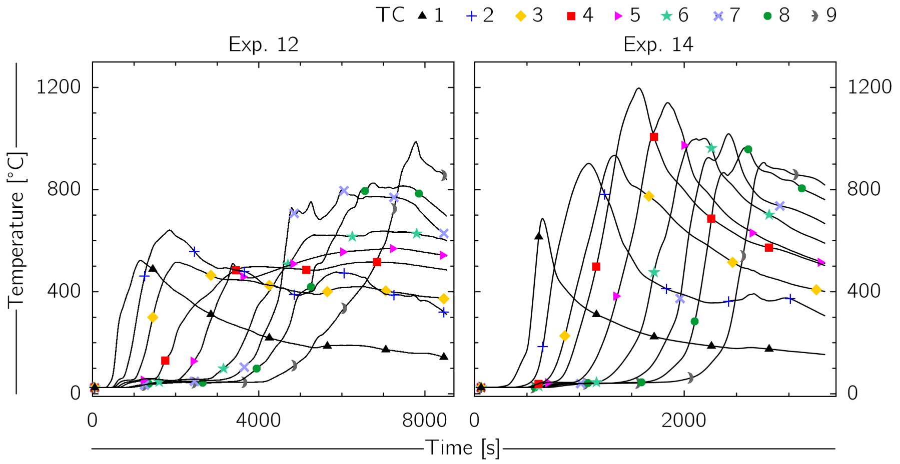

Figure D.4: Plot of temperature evolution for a annular section. Bed proximate analysis: 39.2 wt.% of FC, 19.9 wt.% of VM, 2.2 wt.% of MC, 6.3 wt.% of Ash, and 33.3 wt.% of IM.

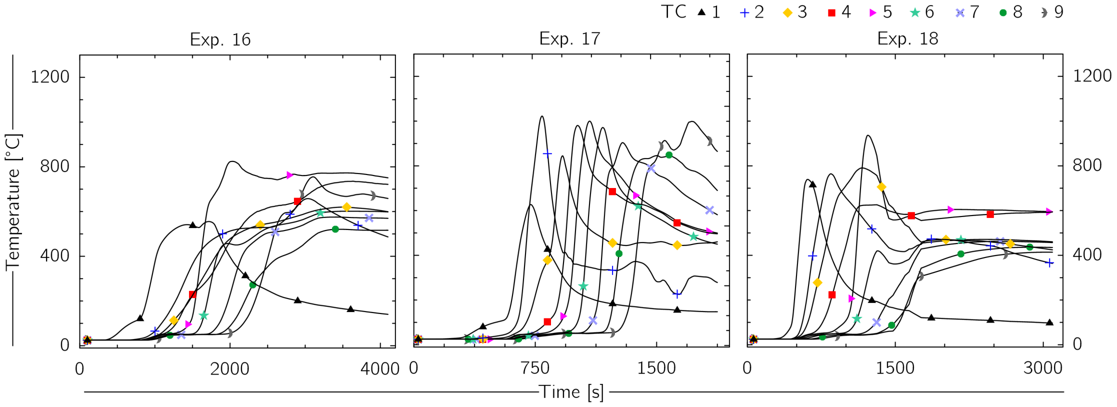

Figure D.5: Plot of temperature evolution for a annular section. Bed proximate analysis: 29.4 wt.% of FC, 14.2 wt.% of VM, 1.7 wt.% of MC, 4.7 wt.% of Ash, and 50.0 wt.% of IM.

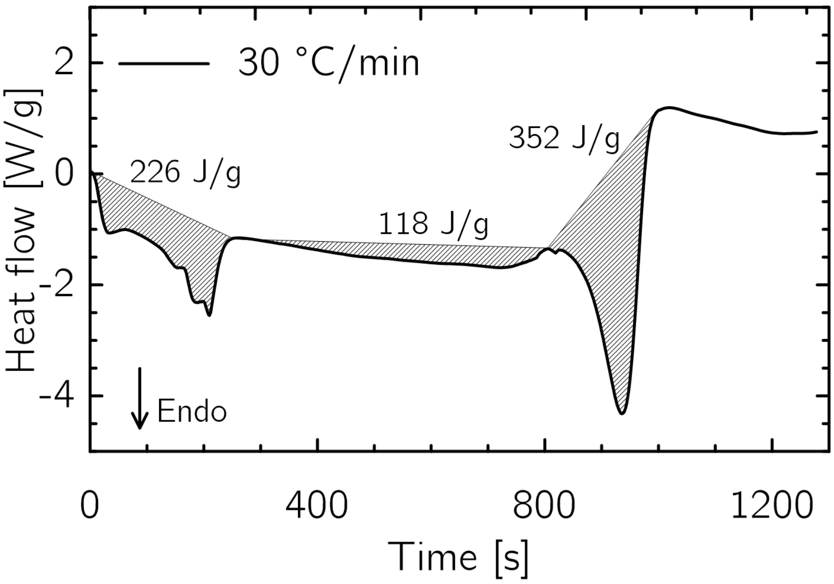

Figure D.6: Differential scanning calorimetry of waste of recycled polyethylene an under inert atmosphere.

Appendix E

Combustion mass balance

The following mass balance takes into account geometric aspects of the porous bed and experimental input and output parameters to calculate the flue gases composition, the combustion front velocity, v_f, and the fraction of carbon oxidized into CO, fr.

- Input parameters

	Equation	Unit
Reactor:		
Combustion chamber internal diameter, ϕ_e	-	m
Pyrolysis chamber external diameter, ϕ_i	-	m
Annular section, S	$\pi(\phi_e^2 - \phi_i^2)/4$	m^2
Bed:		
Bed height, H	-	m
Bed volume, V	SH	m^3
Initial mass, m_0	-	kg
Apparent density, ρ_b	m_0/V	kg/m^3
Charcoal mass fraction, X_{char}	-	%
FC mass fraction, X_{FC}	-	%
FC oxidized by the front, FC_{oxi}	-	%
Sodium bicarbonate mass fraction, $X_{\mathrm{NaHCO_3}}$	-	%
Flow rates:		
Inlet airflow rate, $q_{v_{air}}$	-	l/min
Inlet molar airflow rate, $q_{mol_{air}}$	$q_{v_{air}}/(22.4 \times 60)$	mol/s
Inlet molar flow rate of N_2, $q_{mol_{\mathrm{N_2}}}$	$q_{mol_{air}}(100 - 20.93)/100$	mol/s
Inlet molar flow rate of O_2, $q_{mol_{\mathrm{O_2}}}$	$q_{mol_{air}}(20.93)/100$	mol/s

- Charcoal oxidation

$$C + (1 - \frac{fr}{2})\mathrm{O}_2 \longrightarrow fr\mathrm{CO} + (1 - fr)\mathrm{CO}_2$$

	Equation	Unit
Flow rates:		
Mass flow rate of oxidized FC, $q_{m_{FC}}$	$\rho_b.v_f.S.X_{char}.X_{FC}.FC_{oxi}$	kg/s
Molar flow rate of oxidized FC, $q_{mol_{FC}}$	$q_{m_{FC}}/0.012$	mol/s
Molar flow rate of CO, $q_{mol_{\mathrm{CO}}}$	$q_{mol_{FC}}.fr$	mol/s
Molar flow rate of CO$_2$, $q_{mol_{\mathrm{CO}_2}}$	$q_{mol_{FC}.(1-fr)}$	mol/s
Molar flow rate of consumed O$_2$, $q^{cons}_{mol_{\mathrm{O}_2}}$	$q_{mol_{FC}(1-fr/2)}$	mol/s

- Sodium bicarbonate thermal decomposition

$$\mathrm{NaHCO}_3 \longrightarrow 0.5\mathrm{Na}_2\mathrm{CO}_3 + 0.5\mathrm{CO}_2 + 0.5\mathrm{H}_2\mathrm{O}$$

	Equation	Unit
Decomposition:		
NaHCO$_3$ converted into CO$_2$, $X^{sb}_{\mathrm{CO}_2}$	-	%
NaHCO$_3$ converted into H$_2$O, $X^{sb}_{\mathrm{H}_2\mathrm{O}}$	-	%
Flow rates:		
Molar flow rate of CO$_2$ from NaHCO$_3$, $q^{sb}_{mol_{\mathrm{CO}_2}}$	$\rho_b.v_f.S.X_{char}.X_{\mathrm{NaHCO}_3}.X^{sb}_{\mathrm{CO}_2}/0.044$	mol/s
Molar flow rate of H$_2$O from NaHCO$_3$, $q^{sb}_{mol_{\mathrm{H}_2\mathrm{O}}}$	$\rho_b.v_f.S.X_{char}.X_{\mathrm{NaHCO}_3}.X^{sb}_{\mathrm{H}_2\mathrm{O}}/0.018$	mol/s

- Overall species balance

$$q^{total}_{mol} = q_{mol_{\mathrm{N}_2}} + q_{mol_{\mathrm{CO}}} + q_{mol_{\mathrm{CO}_2}} + q^{sb}_{mol_{\mathrm{CO}_2}} + q_{mol_{\mathrm{O}_2}} - q^{cons}_{mol_{\mathrm{O}_2}} + q^{sb}_{mol_{\mathrm{H}_2\mathrm{O}}}$$

$$\mathrm{O}_2[\%] = \frac{q_{mol_{\mathrm{O}_2}} - q^{cons}_{mol_{\mathrm{O}_2}}}{q^{total}_{mol}} \times 100$$

$$\mathrm{CO}_2[\%] = \frac{q_{mol_{\mathrm{CO}_2}} + q^{sb}_{mol_{\mathrm{CO}_2}}}{q^{total}_{mol}} \times 100$$

$$\mathrm{CO}[\%] = \frac{q_{mol_{\mathrm{CO}}}}{q_{mol}^{total}} \times 100$$

Appendix F

XRD data collection details - PDF-2 database (ICCD, 2007)

F.1 Sample VPE

Table F.1: Matched Materials.

	A) n-Paraffin	B) n-Nonacosane	C) Paraffin wax	D) Pentatriacontane
Formula	$(CH_2)_x$	$C_{29}H_{60}$	C-H	$C_{35}H_{72}$
Pdf Number	40-1995	40-1992	14-763	33-1802
Figure of Merit	65%	26%	20%	19%
Total Peaks	9	5	16	15
Peaks Matched	9	4	12	14

Table F.2: List of Peaks.

2-Theta	D-Spacing	Intensity	Width	Confidence	Matches
9.553	9.2505	57	0.299	99.8%	
10.567	8.3654	66	0.301	99.6%	
19.387	4.5748	121	0.533	95.1%	C
21.481	4.1333	11498	0.317	100%	ABCD
23.770	3.7401	2889	0.350	100%	ACD
29.855	2.9903	118	0.303	100%	ACD
36.239	2.4768	312	0.327	100%	AD
39.718	2.2675	197	0.362	100%	C
41.692	2.1646	94	0.330	100%	CD
42.949	2.1041	135	0.329	100%	CD
43.801	2.0651	52	0.288	92.5%	AD
46.792	1.9398	114	0.424	100%	C
50.228	1.8149	54	0.242	100%	
53.051	1.7248	103	0.414	100%	
54.642	1.6783	46	0.296	99.9%	
64.466	1.4442	19	0.273	92.2%	
72.758	1.2987	24	0.304	97.0%	
79.372	1.2062	24	0.258	92.9%	
102.902	0.9849	18	0.216	98.0%	

F.2 Sample WVPE

Table F.3: Matched Materials.

	A) n-Tetracontane	B) n-Nonacosane	C) n-Heptadecane
Formula	$C_{40}H_{82}$	$C_{29}H_{60}$	$C_{17}H_{36}$
Pdf Number	40-1891	40-1992	36-1590
Figure of Merit	56%	25%	10%
Total Peaks	20	5	28
Peaks Matched	18	4	15

Table F.4: List of Peaks.

2-Theta	D-Spacing	Intensity	Width	Confidence	Matches
21.647	4.1019	7157	0.282	100%	ABCD
24.057	3.6963	1692	0.323	100%	ACD
29.397	3.0358	151	0.247	100%	A
30.162	2.9605	70	0.239	99.6%	ACD
30.919	2.8898	119	0.246	100%	
36.325	2.4711	234	0.325	100%	AC
39.725	2.2671	72	0.340	99.6%	A
40.839	2.2078	84	0.280	100%	AC
41.788	2.1598	74	0.262	100%	AD
43.028	2.1004	109	0.313	100%	AD
43.940	2.0589	54	0.288	97.8%	ACD
46.945	1.9339	45	0.280	98.8%	AD
48.531	1.8743	46	0.221	99.8%	D
50.963	1.7904	56	0.218	100%	
53.085	1.7237	69	0.324	100%	
54.903	1.6709	40	0.253	99.7%	D
57.436	1.6031	49	0.254	100%	
61.588	1.5046	20	0.233	92.2%	D
64.682	1.4399	24	0.251	96.8%	
67.200	1.3919	19	0.250	92.5%	D
70.490	1.3348	19	0.230	94.4%	
72.974	1.2954	22	0.269	96.6%	
74.419	1.2738	25	0.239	98.5%	
78.425	1.2184	20	0.243	91.8%	

F.3 Sample WRPE

Table F.5: Matched Materials.

	A) n-Tetracontane	B) n-Nonacosane	C) n-Tricosane
Formula	$C_{40}H_{82}$	$C_{29}H_{60}$	$C_{23}H_{48}$
Pdf Number	40-1891	40-1992	34-1644
Figure of Merit	65%	20%	10%
Total Peaks	20	5	25
Peaks Matched	16	4	14

Table F.6: List of Peaks.

2-Theta	D-Spacing	Intensity	Width	Confidence	Matches
21.583	4.1139	6718	0.295	100%	ABC
24.011	3.7031	1588	0.325	100%	AC
27.458	3.2457	236	0.254	100%	
29.443	3.0311	80	0.249	100%	A
30.132	2.9634	77	0.260	99.9%	AC
36.214	2.4785	272	0.298	100%	AC
39.717	2.2675	100	0.331	100%	A
40.726	2.2136	38	0.246	96.1%	AC
43.051	2.0993	106	0.350	100%	A
43.951	2.0584	54	0.290	99.1%	AC
46.954	1.9335	46	0.273	99.8%	A
48.621	1.8711	24	0.214	93.4%	
53.005	1.7262	74	0.330	100%	
54.372	1.6859	58	0.259	100%	
55.018	1.6677	37	0.255	97.7%	
69.103	1.3582	17	0.262	93.7%	
74.382	1.2743	20	0.232	96.7%	

APPENDIX G

TGA of PE samples under oxidative atmosphere

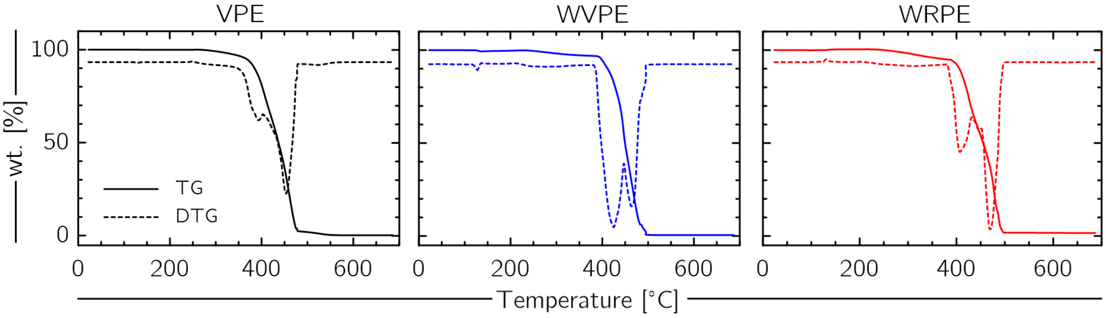

Figure G.1: TGA of PE samples at 20 °C/min, under the oxidative atmosphere and its derivatives.

APPENDIX H

Pyrolysis products yield

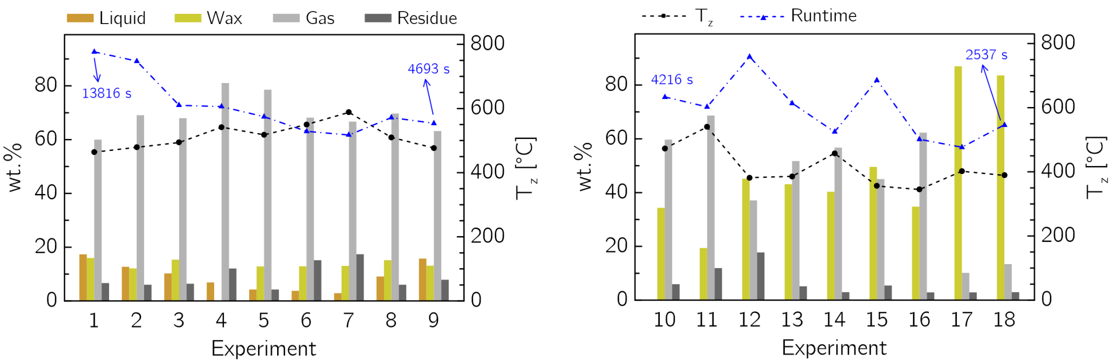

Figure H.1: The yield of pyrolysis products. On the left side for combustion on homogeneous bed (charcoal grains) and on the right for heterogeneous bed (mix of charcoal grains and $NaHCO_3$ powder).